MARIA CURIE-SKŁODOWSKA UNIVERSITY
LUBLIN

Faculty of Mathematics, Physics and Computer Science
Department of Theoretical Physics

Bartłomiej Baran
Supervisor: prof. dr hab. Tadeusz Domański

Dynamical properties of superconducting nanostructures

Lublin 2022

UNIWERSYTET MARII CURIE-SKŁODOWSKIEJ
W LUBLINIE

Wydział Matematyki, Fizyki i Informatyki

Katedra Fizyki Teoretycznej

Bartłomiej Baran
Promotor: prof. dr hab. Tadeusz Domański

Dynamiczne właściwości nadprzewodzących nanoukładów

Lublin 2022

Serdecznie dziękuję prof. Tadeuszowi Domańskiemu
za zaangażowanie, poświęcony czas i merytoryczne wsparcie
podczas studiów doktoranckich.

Dziękuję również prof. Ryszardowi Taranko
za nieocenioną pomoc i owocną współpracę.

Abstract

This thesis is devoted to the theoretical analysis of phenomena occurring in nanosystems under nonequilibrium conditions. The objects of the research are two-terminal nanojunctions consisting of quantum dots with metallic and superconducting electrodes. The main purpose of the research is to analyse time-dependent observables and correlation functions describing the system, e.g. differential conductivity, occupancy of quantum dots, and effective electron pairing on the dots. The nonequilibrium conditions which can be applied to the systems are a sudden change in the potential difference between the electrodes, a quench in the energy level of quantum dots, a sudden change in the hybridization of the quantum dot with the superconducting electrode, and the level of quantum dots oscillating in time. Under the influence of the mentioned perturbations, the evolution of the system takes place, which is noticed in observables and can be proved experimentally. The analysis of the above-mentioned quantities reveals the presence of beats in the charge current, a change in the direction of the flowing current, as well as a transition between the singlet and doublet states, a type of electron dot configuration. In periodically driven systems, we observe the appearance of harmonic states, an additional electron transport channels that contribute directly to the differential conductivity averaged over the period of the driving. These theoretical studies are based on Green's formalism extended by Floquet's theory and the Heisenberg equation.

Streszczenie

Niniejsza praca skupia się na teoretycznej analizie zjawisk zachodzących w nanoukładach w warunkach nierównowagowych. Obiektami badań są dwuterminalne nanozłącza skonstruowane na bazie kropek kwantowych, których elektrody mają charakter metaliczny i nadprzewodzący. Głównym celem badań jest analiza czasowo zależnych obserwabli oraz funkcji korelacyjnych opisujących układ, m.in. przewodnictwa różniczkowego, obsadzenia kropek kwantowych, efektywnego parowania elektronowego na kropkach. Warunki nierównowagowe, którym możemy poddać badany układ to m.in.: nagła zmiana różnicy potencjałów pomiędzy elektrodami, skok poziomu energii kropek kwantowych, zmiana hybrydyzacji kropki kwantowej z elektrodą nadprzewodzącą, a także oscylujący sinusoidalnie w czasie poziom kropek kwantowych. Pod wpływem wymienionych zaburzeń zachodzi ewolucja układu zauważana w obserwablach, których przebieg może zostać sprawdzony eksperymentalnie. Analiza wymienionych wielkości ujawnia występowanie dudnień w charakterystykach prądowych, zmianę kierunku płynącego prądu, a także przejścia pomiędzy stanem singletowym a dubletowym, typem konfiguracji elektronowej kropki. W periodycznie zaburzanych układach obserwujemy pojawienie się stanów harmonicznych, dodatkowych kanałów transportu elektronowego, które mają bezpośredni wkład do charakterystyk przewodnictwa różniczkowego uśrednionego po okresie zaburzenia. Badania teoretyczne opierają się na wykorzystaniu formalizmu funkcji Green'a rozszerzonego o teorię Floquet'a oraz rozwiązywaniu równania Heisenberg'a.

Contents

Chapter 1

Motivation

In recent decades, nanodevice engineering has become a very well-known and developed part of the industry. The method of manufacturing nanostructures offers the possibility of constructing variety nanodevices, information storages, transistors and other components needed in the high-tech branches. The breakthrough in the easy fabrication of semiconductors and semiconducting heterostructures enables the experimental verification of theoretical predictions for new physical phenomena in condensed matter physics. It is amazing how experiment goes hand in hand with theoretical predictions and the design of nanostructures. This remarkable development of condensed matter physics is evident in a growing number of publications in this field, as well as by its many new specialistic subdisciplines.

Following such trends in physics, this thesis addresses the ideas of the condensed matter physics and is focused on the processes occurring in the superconducting nanojunctions. Since the late 1950s, the nanojunctions consisting of the superconductors and quantum impurities have been extensively studied [1,2]. The preliminary research has been focused on the paramagnetic impurities and their influence on the superconducting order. It has been shown that the impurities have negligible impact on the isotropic superconducting state in the bulk materials [3]. However, it has been proved that the

magnetic impurities strongly influence the superconducting order [4–6]. In nanojunctions, it is known that in the boundary area between the normal metal and superconducting material there occurs a mixing of those phases [7].

Unfortunately, the experimental examination of bulk materials gives information about their macroscopic properties. To observe microscopic physical processes we need to focus on the study of the quantum impurities. In the 1980's, the quantum size effect has been observed by the absorption spectrum of excitons in *quantum boxes* [8] or in colloidal nanocrystals [9, 10]. Those *quantum boxes* are epitaxially-grown quasi-zero-dimensional objects made of semiconducting materials. In 1986, the evidence of energy quantization in those objects has been shown and they have been named "quantum dots" [11]. Not much later, it has been presented that quantum dots are characterised by discrete peaks in resonant tunnelling spectra, indicating an atomic density of states in zero dimension [12]. Since then, new fabrication methods of quantum dots had been developed, e.g.: the electron beam lithography of narrow quantum wells made of GaAs/AlGaAs [13] or InGaAs/InP [14], the Stranski-Krastanow method [15, 16], application of carbon nanotubes [17, 18]. The easy and well understood fabrication process has contributed to the discovery of a wide range of quantum dot properties. This knowledge contributed to the development of laser based on the quantum dots [19], photo-detectors [20] and also the incoherent light sources [21]. One of the milestone experiments, performed by Bonadeo et al., was the coherent control, by phase-locked picosecond pulses, of the excitation in a GaAs/AlGaAs single quantum dot on a time scale that is short compared to the time scale of quantum coherence loss [22]. This work has initiated the field of quantum computation based on the optical properties of quantum dots. It has been shown that quantum dot experiments can satisfy some of the criteria of DiVincenzo [23] conditions, necessary for constructing a quantum computer, e.g.: state preparation [24], state read out [25, 26] and coherent manipulation [27, 28].

Furthermore, the use of quantum dots in quantum information can be

based on the spin manipulation. It has been proposed that in the superconducting junction with a quantum point contact or the quantum dot, the Bogoliubov quasiparticles can be trapped in discrete Andreev levels [29, 30]. In contrast to the semiconductor quantum dots this type of device has been called Andreev quantum dot. This proposal of Andreev qubit shows that the experimental manipulation and measurement of a state defined by spin $1/2$ is possible, which provides the opportunity to quantum computing applications. Moreover, another theoretical concept of qubit proposed by Nazarov [31] is based on a superconducting circuit and quantum dot in the form of the Josephson junction. In systems with the spin-orbit interaction, the two-level system is realized by the spin state of the electron on the quantum dot and its polarization can be tuned by the superconducting phase difference across the junction. Based on those ideas, various families of qubit devices have been proposed and experimentally examinated [32]: the charge qubits in a transmission line resonator - *transmons* [33, 34], the gate tunable superconducting qubits - *gatemons* [35–37] or combination of transmon qubits with qubits based on Majorana zero modes [38–42]. This shows that quantum dot devices have a wide range of applications in the current and future quantum computing.

Besides the single quantum dot devices, the double quantum systems have been experimentally studied by the tunnelling spectroscopy using InAs [43–46], InSb [47], Ge/Si [48] and carbon nanotubes [49, 50] as well as by the scanning tunneling microscopy applied to molecules deposited on superconductors [51–55]. It has been shown that in such types of systems it is possible to manipulate and change the state of a single electron [56–58]. It had been proved that for the electrically isolated double quantum dot the eigenstates of the system are characterized by surprisingly long coherence time $\sim 220ns$. For quantum computation purpose the double quantum dot systems can be regarded as a kind of qubit [59].

Furthermore, superconducting circuits based on double quantum dot

systems are rich in the properties of in-gap bound states [47,60–62], originating from the ground state configuration with even or odd parity. Due to the system parameters, the parity change has been experimentally detected by discontinuities of the Josephson current in S-DQD-S junctions [45, 46, 63] or the subgap Andreev current in N-DQD-S junctions [47, 63, 64]. In double quantum dot systems coupled to superconducting lead the spin of quantum dots could create a triplet blockade [63]. This spin locking counteracts the superconducting proximity effect, what has been reported in S-DQD-S [44] and N-DQD-S [64] nanostructures. Quantum dot heterostructures can be studied in terms of time-dependent processes that occur under the influence of step-like pulses or photon exchange with the environment [65–67], leading to the post-quench evolution and photo-assisted tunnelling processes. The time-dependent experimental measurements for the Josephson junction placed in microwave cavity exhibits discretization of super-current and higher-order effects such as multiple Andreev reflections and Shapiro-like steps in conductance characteristics [68–70].

This thesis is devoted to theoretical studies of time-dependent processes, occurring in systems with single and double quantum dots placed between the normal metal and superconducting leads. The main objective is to study the evolution of systems induced by the temporary and long-term disturbance of its properties such as: rapid change of source-drain voltage or energy level position of quantum dot, sudden coupling to superconducting lead and periodic driving of the quantum dot energy levels. Depending on the type of perturbation, the systems exhibit different ways of reaching equilibrium. We investigate the relaxation times and associated phenomena manifested in post-quench evolution, evident in the time-dependent current characteristics. For this purpose we made use of: Green's function method, Floquet formalism and Heisenberg's equation of motion technique.

Chapter 2

Introduction to superconductivity

The superconductors, as their name suggests, are characterised by perfect conductivity, which can be observed in specific materials under some physical conditions. Superconductivity, as physical phenomenon has been discovered more than one century ago [71]. The presence of perfect conductivity is one of the essential characteristics of superconductors, playing an important role from an economic point of view. Superconductors are also characterised by ideal diamagnetism [72]. In the presence of a magnetic field, its lines are expelled from the bulk of superconductor - the Meissner effect. For correspondingly higher values of the external magnetic field the superconducting effect disappear, and the field penetrates the volume of the material. The value of the magnetic field at which the superconducting effect is suppressed is called the critical point B_c. It happens for the *pure* superconductors, like 27 metals (e.g. Al, Pa, Th, Pb) which are called Type I superconductors, having the critical temperature $T_C < 7.2K$, below which the superconducting effect appears. Type II superconductors are made from alloys (e.g. NbTi, PbMoS, NbN), they are colloquially known as *dirty* superconductors. They maintain the superconducting state to higher temperatures (tens of Kelvin) and magnetic fields, than I type superconductors. The second type superconductors can exist in a mixed state of normal and superconducting regions,

called a vortex state. This state predicted by Abrikosov is characterized by vortices of superconducting currents surrounding cores of materials in normal state.

In this chapter, we will provide a short theoretical description of the superconductors and the processes occurring at the interface of different materials. The following sections (Sec. 2.1, 2.2) are based on the popular books [73–75].

2.1 Electron bound states of bulk materials

The breakthrough step in the formulation of the microscopic theory of conductivity had been made by Cooper [76]. In 1956, Cooper showed that two electrons, interacting on the Fermi sphere, can create a bound state, called later a *quasiparticle* or Cooper pair. This state appears in the presence of the weak attractive interaction. One of Cooper's assumptions was that pairing between electrons occurs in the singlet state $\chi = \frac{1}{\sqrt{2}}(|\uparrow\downarrow\rangle - |\downarrow\uparrow\rangle)$, which guarantees the antisymmetry of wave-function. In theory, the pair of electrons can be described by the two particle wave-function in the real space coordinates r_i

$$\psi(r_1, r_2) = \phi_q(r_1 - r_2)e^{iqR}\chi, \tag{2.1}$$

where $R = (r_1 + r_2)/2$ is the center of mass, ϕ_q is wave-function in the center of mass and q is momentum of the center of the mass of the pair with respect to the Fermi sea. One of the Cooper's assumptions is that the center of mass of the pair lies in the center of the Fermi sphere $q = 0$. Making a Fourier expansion of ϕ_q, the two particle wave-function takes form

$$\psi(r_1, r_2) = \sum_k g(k)e^{ikr_1}e^{-ikr_2}\chi, \tag{2.2}$$

where $g(k)$ is a Fourier transform of the center-of-mass wave-function. The wave-function of the pair of electrons consists of the plane waves with equal and opposite momenta.

Solving the Schrödinger equation for the introduced wave-function $\psi(r_1, r_2)$ of the Hamiltonian

$$\hat{H} = -\frac{\hbar^2}{2m}(\nabla_1^2 + \nabla_2^2) + V(r_1, r_2), \tag{2.3}$$

where $V(r_1, r_2)$ is the interaction term, yields

$$\sum_{k'}\left[\frac{\hbar^2}{2m}2k'^2 + V(\rho)\right]g(k')e^{ik'\rho} = \left(\varepsilon + 2\frac{\hbar^2 k_F^2}{2m}\right)\sum_{k'} g(k')e^{ik'\rho}. \tag{2.4}$$

Here, the translational invariance has been assumed $V(r_1, r_2) = V(\rho)$ and ε is a total energy of two considered electrons. Multiplying both sides of (2.4) by $e^{ik\rho}$ and integrating over $d^3\rho$, we obtain

$$\frac{\hbar^2}{m}\int \sum_{k'} e^{i(k'-k)\rho}g(k')k'^2 d^3\rho + \int \sum_{k'} V(\rho)e^{i(k'-k)\rho}g(k')d^3\rho = \left(\varepsilon + \frac{\hbar^2 k_F^2}{m}\right)\int \sum_{k'} e^{i(k'-k)\rho}g(k')d^3\rho. \tag{2.5}$$

It is important to notice that the above equation has a non-zero solution only if $k = k'$:

$$\int d^3\rho e^{i(k-k')\rho} = L^3\delta_{k,k'}. \tag{2.6}$$

Then (2.5) takes form

$$\frac{\hbar^2}{m}k^2 g(k) + \sum_{k'} g(k')V_{kk'} = (\varepsilon + 2\varepsilon_F)g(k), \tag{2.7}$$

where $V_{kk'} = \frac{1}{L^3}\int V(\rho)e^{i(k-k')\rho}d^3\rho$.

The Cooper theory assumes that the attraction potential takes a constant value up to a cut-off imposed by the Debye frequency ω_D which is order of $k_B\theta_D$, where k_B is Boltzmann constant and θ_D Debye temperature. This means that the coefficient $V_{kk'}$ fulfills the following relations:

$$V_{kk'} = \begin{cases} -V/L^3 & \text{if} \quad |\xi_k|, |\xi_{k'}| \leqslant \hbar\omega_D, \\ 0 & \text{otherwise}, \end{cases} \tag{2.8}$$

where $\xi_k = \frac{\hbar^2 k^2}{2m} - \varepsilon_F$. Substituting this simple form of potential $V_{kk'}$ into (2.8) we obtain

$$(-2\xi_k + \varepsilon)\, g(k) = -\frac{V}{L^3} \sum_{k'} g(k'). \tag{2.9}$$

Dividing both sides of (2.9) by the factor $(-2\xi_k + \varepsilon)$ and performing summation over k, yields

$$\sum_k g(k) = \frac{V}{L^3} \sum_{kk'} \frac{1}{2\xi_k - \varepsilon} g(k'). \tag{2.10}$$

The right-hand side of (2.10) contains term $\sum_{k'} g(k')$, which is generally a constant value, equal to the left side of the equation. This term can be omitted, which results in the self-consistent condition

$$\frac{V}{L^3} \sum_k \frac{1}{2\xi_k - \varepsilon} = 1. \tag{2.11}$$

Converting summation to integration from zero up to the Debye frequency, yields

$$V \int_0^{\hbar\omega_D} \frac{\nu(\xi) d\xi}{2\xi - \varepsilon} = 1, \tag{2.12}$$

where $\nu(\xi)$ is the density of states for electrons (which practically takes constant value over the range of the integration). Then, performing the integration and assuming that $|\varepsilon| \ll \hbar\omega_D$, we finally obtain the energy electron pair

$$\varepsilon = -2\hbar\omega_D e^{-2/\nu(0)V}. \tag{2.13}$$

A negative sign indicates that a bound state is formed from attracting electrons. In other words, the energy of the bound electrons is lower than that of the free particles.

2.2 Bardeen-Cooper-Schrieffer theory

This scenario of the bound state formed of two electrons was fundamental to the macroscopic theory of superconductivity. Theoretical explanation of

the superconducting state was presented by a group of scientists consisting of J. Bardeen, L. Cooper and J. R. Schrieffer (BCS) and was awarded the Nobel Prize in 1972. The BCS theory is based on the Cooper model, the fact that the attractive interaction can bind two electrons with opposite spins and momentum vectors $(k\uparrow, -k\downarrow)$ into one pair on Fermi sphere [77]. The Cooper result (see Sec. 2.1) implies that many-body system can reveal the energy gap in their excitation spectrum. For the many-body case, the Cooper result suggests that the ground-state wave-function Ψ_N could be constructed of the paired electrons

$$\Psi_N = \psi(1,2)\psi(3,4)\psi(5,6)...\psi(N-1,N), \tag{2.14}$$

where N denotes the number of particle in the system. The pair wave-function $\psi(1,2) = \sum_k g(k)e^{ikr_1}e^{-ikr_2}\chi$ is multiplied by individual coefficient $g(k)$. For a realistic case this description is useless, because $\sim 10^{200}$ individual coefficients need to be calculated [74].

In the BCS theory and the second quantization representation, the ground state of the many-body system was proposed as collection of Cooper pairs

$$|\Psi_{BCS}\rangle = \Pi_{k=k_1,...,k_N}(u_k + v_k\hat{c}^\dagger_{k\uparrow}\hat{c}^\dagger_{-k\downarrow})|0\rangle, \tag{2.15}$$

where $|0\rangle$ denotes the vacuum and u_k, v_k are coefficients whose square are the probability of empty ($|u_k|^2$) and occupied ($|v_k|^2$) state with wave-vector k respectively. In order to satisfy the normalization condition $\langle\Psi_{BCS}|\Psi_{BCS}\rangle = 1$, the probabilities must obey the following relation

$$|u_k|^2 + |v_k|^2 = 1. \tag{2.16}$$

The wave-function Ψ_N defined in (2.14) describes the system consisting of $N/2$ electron pairs, while Ψ_{BCS} defined in (2.15) is a superposition of pairs containing the even number of electrons, without fixed number of particles. Between those two wave-functions a following relation can be written

$$\Psi_{BCS} = \sum_N \lambda_N \Psi_N, \tag{2.17}$$

with the normalization condition $\sum_N \lambda_N = 1$.

The many-body system with translational invariance can be described by Hamiltonian

$$H = \sum_{k\sigma} \xi_k \hat{c}^\dagger_{k\sigma} \hat{c}^\dagger_{k\sigma} + \sum_{kk',\sigma\sigma',q} V_{kk',\sigma\sigma',q} \hat{c}^\dagger_{k+q,\sigma} \hat{c}^\dagger_{k'-q,\sigma'} \hat{c}_{k'\sigma'} \hat{c}_{k\sigma}, \tag{2.18}$$

where $\xi_k = \frac{\hbar^2 k^2}{2m} - \varepsilon_F$ denotes the electron energies with respect to the Fermi level. The second term of Hamiltonian in (2.18) describes electron-electron interactions.

The binding energy of the Cooper pair depends on the sum of the total angular momentum of the electrons $K = k_1 + k_2$, where k_1 and k_2 are their wave-vectors. It reaches a maximum value for $K = 0$ and decreases dramatically for other values, implying that the electrons have opposite wave-vectors $k_1 = -k_2$. The origin of the attractive force originate from a phonon exchange, giving rise to an effective interaction. Considering the negatively charged electrons

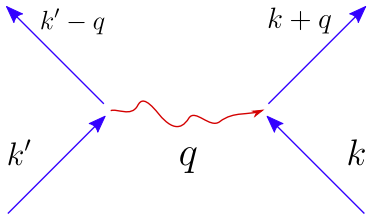

Figure 2.1: Diagrammatic representation of the exchange of a phonon q in the effective electron-electron interaction.

moving through the lattice of the positively charged lattice ions. The phonon can be exchanged as schematically presented in Fig. 2.1. In this process, the maximum possible phonon energy is truncated by the Debye frequency ω_D (the crystal lattice is not able to transfer higher energies) and furthermore the angular momentum should be conserved $k + k' = const$.

The Hamiltonian in (2.18) can be written in a simpler, *reduced* form. We can restrict the consideration to that part which contributes to the

superconducting effect, i.e., the interactive part taking into account only electrons with opposite spins and momenta. We can replace $k' \to -k$ and $k + q \to k'$, which yields

$$H = \sum_{k\sigma} \xi_k \hat{c}^\dagger_{k\sigma} \hat{c}^\dagger_{k\sigma} + \sum_{kk'} V_{kk'} \hat{c}^\dagger_{k\uparrow} \hat{c}^\dagger_{-k\downarrow} \hat{c}_{-k'\downarrow} \hat{c}_{k'\uparrow}. \tag{2.19}$$

To determine particular the coefficients u_k and v_k, we can use the variational principle of quantum mechanics to minimize the expectation value of the Hamiltonian (2.19)

$$\delta \langle \psi_{BCS} | \sum_{k\sigma} \xi_k \hat{c}^\dagger_{k\sigma} \hat{c}^\dagger_{k\sigma} + \sum_{kk'} V_{kk'} \hat{c}^\dagger_{k\uparrow} \hat{c}^\dagger_{-k\downarrow} \hat{c}_{-k'\downarrow} \hat{c}_{k'\uparrow} | \psi_{BCS} \rangle = 0. \tag{2.20}$$

The expectation value of the first and the second terms presented in (2.20) are given by

$$\langle \psi_{BCS} | \sum_{k\sigma} \xi_k \hat{c}^\dagger_{k\sigma} \hat{c}^\dagger_{k\sigma} | \psi_{BCS} \rangle = 2 \sum_k \xi_k |v_k|^2 \tag{2.21}$$

and

$$\langle \psi_{BCS} | \sum_{kk'} V_{kk'} \hat{c}^\dagger_{k\uparrow} \hat{c}^\dagger_{-k\downarrow} \hat{c}_{-k'\downarrow} \hat{c}_{k'\uparrow} | \psi_{BCS} \rangle = \sum_{kk'} V_{kk'} v^*_k u_k v_{k'} u^*_{k'}. \tag{2.22}$$

For convenience it can be assumed that the coefficient u_k and v_k are real numbers

$$u_k = \cos\theta_k \quad \text{and} \quad v_k = \sin\theta_k, \tag{2.23}$$

which gives us the variational minimization condition with respect to the parameter θ_k in form

$$\frac{\partial}{\partial \theta_k} \left(2 \sum_k \xi_k \sin^2\theta_k + \frac{1}{4} \sum_{kk'} \sin 2\theta_k \sin 2\theta_{k'} \right) = 0. \tag{2.24}$$

As a result of minimization we obtain

$$\xi_k \tan 2\theta_k = -\frac{1}{2} \sum_{k'} V_{kk'} \sin 2\theta_{k'}. \tag{2.25}$$

At this step, let us define an auxiliary parameter of the energy dimension

$$\Delta_k = -\sum_{k'} V_{kk'} u_k v_{k'} = -\frac{1}{2} \sum_{k'} \sin 2\theta_{k'}, \tag{2.26}$$

which can be called a gap function or order parameter. Substituting (2.26) into (2.25) we obtain

$$\sin 2\theta_k = 2u_k v_k = \frac{\Delta_k}{E_k}, \tag{2.27}$$

where $E_k = \sqrt{\xi_k^2 + \Delta_k^2}$. For completeness, we can also calculate

$$\cos 2\theta_k = u_k^2 - v_k^2 = \frac{\xi_k}{E_k}. \tag{2.28}$$

Having defined the relation between v_k and u_k in (2.16) and their combinations in (2.27), (2.28), we can obtain the coherence factors in formal forms

$$\begin{aligned} u_k^2 &= \frac{1}{2}\left(1 + \frac{\xi_k}{E_k}\right), \\ v_k^2 &= \frac{1}{2}\left(1 - \frac{\xi_k}{E_k}\right), \end{aligned} \tag{2.29}$$

where the excitation energy $E_k = \sqrt{\xi_k^2 + \Delta_k^2}$. Substituting (2.27) into (2.26) yields a non-linear gap equation

$$\Delta_k = \sum_{k'} V_{kk'} \frac{\Delta_{k'}}{2\sqrt{\xi_{k'}^2 + \Delta_{k'}^2}}. \tag{2.30}$$

The BCS theory assumes that the attraction potential takes a constant value up to a cut-off imposed by the Debye frequency ω_D. This means that the coefficient $V_{kk'}$ fulfils the following relation

$$V_{kk'} = \begin{cases} -V & \text{if} \quad |\xi_k|, |\xi_{k'}| \leqslant \hbar\omega_D, \\ 0 & \text{otherwise}, \end{cases} \tag{2.31}$$

which implies

$$\Delta_k = \begin{cases} \Delta & \text{for} \quad |\xi_k| \leqslant \hbar\omega_D, \\ 0 & \text{for} \quad |\xi_k| > \hbar\omega_D. \end{cases} \tag{2.32}$$

We can consider the following extreme situations:

- $|\xi| \gg \Delta$ the energy of the particles is greater than the energy of the superconducting gap and they behave like free electrons,

- $|\xi| \ll \Delta$ the electrons experience the pairing energy gap.

Assuming momentum-independent potential (justified in isotropic systems) parameter Δ_k can be cancelled on both side of the equation. Integrating (2.30) over energy ξ in the range $\pm\hbar\omega_D$ yields

$$1 = \nu(0)V \int_{-\hbar\omega_D}^{+\hbar\omega_D} \frac{d\xi}{2\sqrt{\xi^2 + \Delta^2}} = \nu(0)V \sinh^{-1}\left(\frac{\hbar\omega_D}{\Delta}\right), \tag{2.33}$$

or

$$\Delta = \hbar\omega_D \sinh^{-1}\left(\frac{1}{\nu(0)V}\right), \tag{2.34}$$

where $\nu(0)$ is the normal density of states at the Fermi level. In the weak-coupling limit $V\nu(0) \ll 1$ the gap function is given by the expression

$$\Delta \cong 2\hbar\omega_D e^{-1/V\nu(0)}. \tag{2.35}$$

In the Hartree-Fock-Bogoliubov approximation, the interaction term in (2.19) can be linearized

$$\begin{aligned} -V \sum_{kk'} \hat{c}^\dagger_{k\uparrow}\hat{c}^\dagger_{-k\downarrow}\hat{c}_{-k'\downarrow}\hat{c}_{k'\uparrow} \simeq -\sum_k \hat{c}^\dagger_{k\uparrow}\hat{c}^\dagger_{-k\downarrow} V \sum_{k'} \langle \hat{c}_{-k'\downarrow}\hat{c}_{k'\uparrow}\rangle \\ -V \sum_k \langle \hat{c}^\dagger_{k\uparrow}\hat{c}^\dagger_{-k\downarrow}\rangle \sum_{k'} \hat{c}_{-k'\downarrow}\hat{c}_{k'\uparrow} + V \sum_k \langle \hat{c}^\dagger_{k\uparrow}\hat{c}^\dagger_{-k\downarrow}\rangle \sum_{k'} \langle \hat{c}_{-k'\downarrow}\hat{c}_{k'\uparrow}\rangle, \end{aligned} \tag{2.36}$$

where $V\sum_k \langle \hat{c}_{-k\downarrow}\hat{c}_{k\uparrow}\rangle \equiv \Delta$. It yields the reduced BCS Hamiltonian

$$H \simeq \sum_{k\sigma} \xi_k \hat{c}^\dagger_{k\sigma}\hat{c}^\dagger_{k\sigma} - \left(\Delta \sum_k \hat{c}^\dagger_{k\uparrow}\hat{c}^\dagger_{-k\downarrow} + h.c.\right). \tag{2.37}$$

Near the critical temperature the energy gap can be approximated by following relation:

$$\Delta(T) \approx \Delta(0)\sqrt{1 - \frac{T}{T_c}}, \tag{2.38}$$

where $\Delta(0) \approx 1.74 k_B T_C$ is the energy gap for $T = 0$. In the bulk superconductor, the spatial range of the Cooper pairs is called the coherence length

ξ_S and is strictly connected with the energy gap Δ. The coherence length ranges from tens to hundreds of nanometres and is defined as follows

$$\xi_S = \frac{\hbar v_F}{\pi \Delta}, \tag{2.39}$$

where v_F denotes Fermi velocity. The temperature dependence of the coherence length depends of the mean free path for the electrons l_e. In the homogenous materials $\xi_S \ll l_e$ the coherence length has form

$$\xi(T) = 0.74 \xi_S \sqrt{\frac{T_c}{T_c - T}}. \tag{2.40}$$

For doped materials $\xi_S \gg l_e$ the coherence length obeys the following equation

$$\xi(T) = 0.85 \sqrt{\xi_S l_e} \sqrt{\frac{T_c}{T_c - T}}. \tag{2.41}$$

In contrast to the phonon superconductors, we can mention other types of superconducting phases. For example, the superconducting state has been found in the heavy fermion compound UGe_2 [78], which is qualitatively similar to the classic d–electron ferromagnets. In the ferromagnetic superconductor the quasiparticles responsible for the ferromagnetism form the Cooper pairs, for which the triplet pairing appears $(k \uparrow, -k \uparrow)$ [79]. Moreover, the superconducting effect can exist in form of FFLO phase (Fulde-Ferrell-Larkin-Ovchinnikov) [80–82]. In the presence of a magnetic field, we can find a pair of electrons $(k \uparrow, q - k \downarrow)$ in the bulk of the metal, which have nonzero total momentum $K \neq 0$. The external magnetic field induces a Zeeman energy splitting, the Fermi spheres differ for individual spins, resulting in the pairing of electrons into singlet pairs with total momentum q. Furthermore, it is important to mention about the high-temperature superconductors, the class of the materials which can not be simply described by the BCS theory. High-temperature superconductors exhibit precursor pairing effects at higher temperatures than T_c. Lately, it has been possible to obtain the first superconducting state at room temperature, discovered in the mixture of H_2S+CH_4 at high pressure 267 GPa [83]. Experimental results indicate that

the high-temperature superconductors involve singlet Cooper pairing with a d-wave symmetry [84], unlike in the BCS theory where the superconducting energy gap has a s-wave symmetry.

2.3 The proximity effect and Andreev reflection

At the metal-superconductor boundary the properties of both materials are mixed nearby the junction region [85–88]. The superconducting order enters the metal in the vicinity of the junction and the density of Cooper pair is exponentially descending together with the distance from the superconductor (see Fig. 2.2). The leakage of Cooper pairs into the metal can be understood as classical particle diffusion, where the pairing (coherence of Cooper pair) is gradually destroyed by scattering on other particles or lattice ions of metal. In the Ginzburg-Landau theory [89], the Cooper pair function is described by following macroscopic wave-function

$$\psi(r) = \sqrt{N(r)}e^{i\phi(r)}, \tag{2.42}$$

where $N(r)$ is density of Cooper pairs and $\phi(r)$ is their phase.

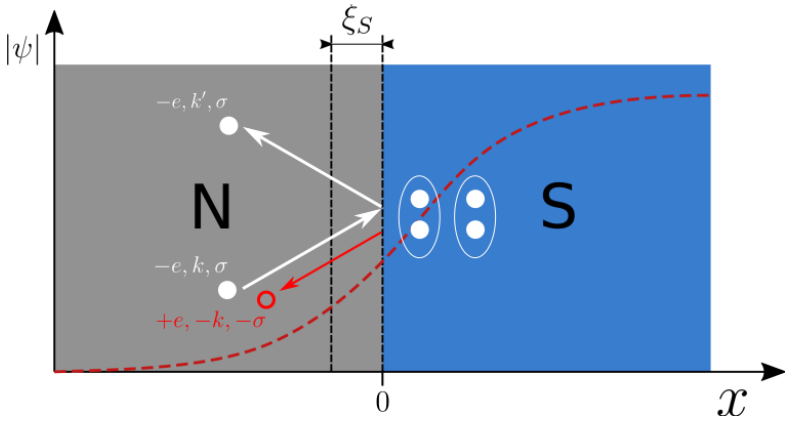

Figure 2.2: The visualization of the Andreev/normal reflection at the metal-superconductor interface and the superconducting proximity effect (marked by red dashed line) for $T < T_C$, where ξ_S denotes the coherence length.

The electron diffusion differs when particle transport is from metal to superconductor. In metal, a moving electron characterised by an energy $\varepsilon_{k\sigma}$ with a Bloch wave-vector k and spin σ can cross the metal-superconductor boundary. When the energy of electron is smaller than the superconducting gap $|\varepsilon_k - E_F| < \Delta$, where E_F denotes the Fermi energy of the metal, the electron cannot enter into a superconductor as a single particle (the normal reflection). In other possible process, an incoming electron can be bound to another electron with opposite momentum and spin, thus forming the Cooper pair which next propagates in the superconductor. This process, called the Andreev reflection, happens when the incoming electron with energy smaller than the energy gap is reflected as a hole with the opposite wave-vector $-k$ and spin $-\sigma$. The Andreev reflection involves the electron-hole transition process [90, 91], the reflected hole moves along the same path with reverse direction as the incoming electron. The incoming electron crosses the metal-superconductor interface and combines into the Cooper pair with the remaining electron having the spin and momentum opposite to its own. In case of $|\varepsilon_k - E_F| < \Delta$ the reflection is dominated by Andeev process with high probability $R_A \approx 1$ and the normal reflection may be ignored. Otherwise, for energies larger than the gap, the electrons be normally reflected (see Fig. 2.3a).

The Andreev scattering can be described by the microscopic approach with the Bogoliubov-de Gennes equations [92, 93]:

$$\begin{aligned} E\psi(x) &= \left(-\frac{\hbar^2}{2m}\frac{d^2}{dx^2} - \mu\right)u(x) + \Delta(x)v(x), \\ E\psi(x) &= \left(\frac{\hbar^2}{2m}\frac{d^2}{dx^2} + \mu\right)v(x) + \Delta(x)u(x), \end{aligned} \tag{2.43}$$

where μ denotes the chemical potential, $\Delta(x)$ is a spatial pairing potential and $\psi(x)$ is the 2-component wave-function

$$\psi_{\pm k^+} = \begin{pmatrix} u \\ v \end{pmatrix} e^{\pm i k^+ x}, \tag{2.44}$$

$$\psi_{\pm k^-} = \begin{pmatrix} u \\ v \end{pmatrix} e^{\pm i k^- x}, \tag{2.45}$$

defining the position in the space of the quasiparticles. By k^+ and k^- we denote the wave-vectors for electrons and holes, respectively. In such model, we can expect different Fermi momenta in the two materials, some elastic scattering in the electrodes and at the metal-superconductor interface. Assuming that there is no dissipation in the leads, the scattering at the phase boundary can be modelled by the delta function $V(x) = H\delta(x)$, with a potential barrier H. At the metal-superconductor interface the following boundary conditions can be assumed: the continuity of ψ at $x = 0$, i.e. $\psi_N(0) = \psi_S(0)$ and its spatial derivatives $\hbar/2m(\psi'_S(0) - \psi'_N(0)) = H\psi(0)$. Using these assumptions, the few types of plane waves can be distinguished: ψ_{inc} an incident wave, a reflected wave ψ_{refl} and a transmitted wave ψ_{transm}, having two possible solutions [93]:

$$\psi_{inc} = \begin{pmatrix} 1 \\ 0 \end{pmatrix} e^{iq^+ x}, \tag{2.46}$$

$$\psi_{refl} = a\begin{pmatrix} 0 \\ 1 \end{pmatrix} e^{iq^- x} + b\begin{pmatrix} 1 \\ 0 \end{pmatrix} e^{-iq^+ x}, \tag{2.47}$$

$$\psi_{transm} = c\begin{pmatrix} u \\ v \end{pmatrix} e^{ik^+ x} + d\begin{pmatrix} v \\ u \end{pmatrix} e^{-ik^- x}, \tag{2.48}$$

with

$$\hbar k^\pm = \sqrt{2m}[\mu \pm \sqrt{E^2 - \Delta^2}]^{1/2}, \tag{2.49}$$

$$\hbar q^\pm = \sqrt{2m}[\mu \pm E]^{1/2}, \tag{2.50}$$

and the appropriate coefficients: $a = uv/\gamma$, $b = -(u^2 - v^2)[(H/\hbar v_F)^2 + iH/\hbar v_F]/\gamma$, $c = u(1 - iH/\hbar v_F)/\gamma$, $d = ivH/\gamma\hbar v_F$, where $\gamma = u^2 + (u^2 - v^2)(H/\hbar v_F)^2$. Leaving aside the elastic scattering at the boundary of those two materials, the coefficients b and d are zero, which makes the Andreev reflection out of dissipation of quasiparticles. The amplitude coefficients u, v are energy dependent and they are defined in (2.29).

The Andreev scattering can appear in different heterostructures, e.g.: two N-S interfaces combined into a S-N-S heterostructure which form a Josephson junction [91], schematically presented in Fig. 2.3a. In a Josephson junction charge current flows without an applied voltage, this is known as a supercurrent. The intensity of the supercurrent is exponentially dependent on the correlation length of Cooper pairs, thickness of the normal metal layer and what is the most important the macroscopic phase difference between the superconductors $\phi = \phi_{S1} - \phi_{S2}$. For the tunnelling processes the transmitted wave-function is phase dependent

$$\psi_{transm} = c\begin{pmatrix} ue^{i\phi_{S1}} \\ v \end{pmatrix} e^{ik^+x} + d\begin{pmatrix} ve^{i\phi_{S2}} \\ u \end{pmatrix} e^{-ik^-x}. \tag{2.51}$$

Due to the finite length of metallic material, the discrete levels are formed in the energy spectrum [92–95]. Satisfying the continuity conditions for wave-functions and their derivates at the material boundaries (at $x = \pm L/2$, where L is width of the normal metal) the dispersion relation for particle with energies below the superconducting gap $|E| < \Delta$ takes form

$$e^{2i\alpha(E)} e^{i(k^+ - k^-)L} e^{\pm i\phi} = 1, \tag{2.52}$$

where the energy-dependent phase factor is defined by $\alpha(E) = \arccos(E/\Delta)$. In the systems composed of high-density superconductors (with negligible spin-orbit interaction and without magnetic field), neglecting the elastic scattering and considering the particle energies much lesser than the Fermi energy $|E| \ll E_F$ the eigenvalues can be calculated by using the relation $\hbar(k^+ - k^-) = 2E/v_F$. It yields

$$E_n^{\pm} = \frac{\hbar v_F}{2L}\left[2\pi\left(n + \frac{1}{2}\right) \pm \phi\right] \tag{2.53}$$

where $n = 0, 1, 2, ...$, unless the levels approach Δ. In the case of Andreev limit $|E| \ll E_F$ [96], the Andreev reflection probability reaches from $R_A \approx T_n^2/(2 - T_n)^2$ at $E = 0$ upto $R_A = 1$ at $E = \Delta$ [97], where T_n denotes the normal transmission coefficient. In point contact superconducting junctions,

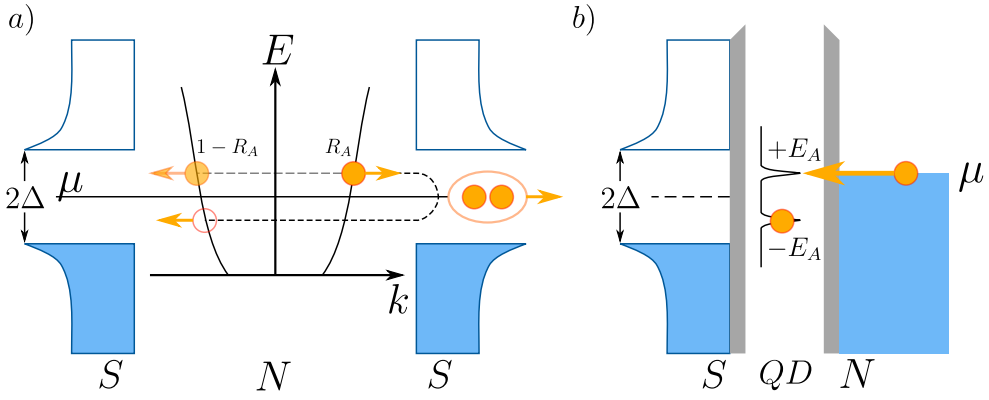

Figure 2.3: Scheme of: a) Bound states in a short S-N-S junction with phase-dependent energy $E(\phi)$ below the energy gap Δ, as result of Andreev reflection. b) Andreev bound states formed in S-QD-N junction, having essential role in transport spectroscopy [95].

where the superconductors are weakly connected, the contact region can be treated as the normal metal. Then, the metal region is much smaller than the coherence length of Cooper pairs $L_N \ll \xi_S$. For energies smaller that the energy gap $|E| < \Delta$ the relation in (2.52) has following solution

$$\alpha(E) = \arccos(E/\Delta) = \pm(\phi/2) \tag{2.54}$$

which implies a simple relation

$$E = \pm\Delta\cos(\phi/2). \tag{2.55}$$

Taking into account the elastic scattering, the discrete energy levels (bound states) are given by

$$E_n = \Delta\left[1 - T_n \sin^2(\phi/2)\right]^{1/2}, \tag{2.56}$$

with $n = 1, 2, ...m$ the number of allowed modes and T_n denoting the normal transmission coefficient for each independent scattering-matrix eigenmode in the normal phase [98, 99]. The scattering-matrix T_n takes values from range $\langle 0, 1\rangle$.

In the metal-superconductor heterostructure, where the quantum dot is a barrier between the materials, the Andreev states can also appear (see Fig. 2.3b). Emergence of the Andreev states in quantum dot strictly originates from the neighbouring superconductor. Their nature depends on the size of the pairing gap Δ and the Coulomb repulsion U between electrons [7]. For relatively large value of Δ, the multiple Andreev reflections give rise to Andreev bound states [100]. In the other limit, when the Coulomb repulsion U is dominant value in the system, the Andreev reflections are suppressed [101]. The influence of Δ and U on Andreev states will be discussed in details in Sec. 3.1. Emergence of the Andreev states will be systematically investigated in Sec. 3.4. Let us emphasize that such bound states are well detectable experimentally. Fig. 2.4a presents the recent results obtained for the Andreev in-gap states observed in differential conductance of current versus applied source-drain voltage and Fig. 2.4b shows their behaviour at the different temperatures.

Moreover, the proximity effect can be found in the different type of systems, e.g. in superconductor-ferromagnet heterostructures [102], what gives opportunity to study the dynamical properties of Josephson nanojunction with ferromagnet impurities [103, 104].

In multiterminal devices based on quantum dots, the other types of Andreev's scattering take place. For example, in a Cooper pair splitter device experimentally realised by Schönenberger's group [105] and theoretically investigated by [106–108] (schematically presented in Fig. 2.5), we can distinguish few types of scattering. The first possibility is ballistic transport (not presented in figure), which involves the flow of both electrons through the induced Andreev states on quantum dot, between the left and right electrodes. A second possibility for charge transport is the Direct Andreev Refflection (DAR), which occurs when an electron from the left electrode flows through the quantum dot on which it combines a pair with an electron from the second electrode (schematically presented in Fig. 2.5a). Then the paired electrons

flow into the superconductor. The third transport possibility is the Crossed Andreev Reflection (CAR), which involves the flow of an electron from one electrode to the quantum dot, on which the electron pairs up with an electron originating from the electron-hole transition process. In such case, the hole is reflected to the opposite electrode, what is schematically presented in Fig. 2.5b.

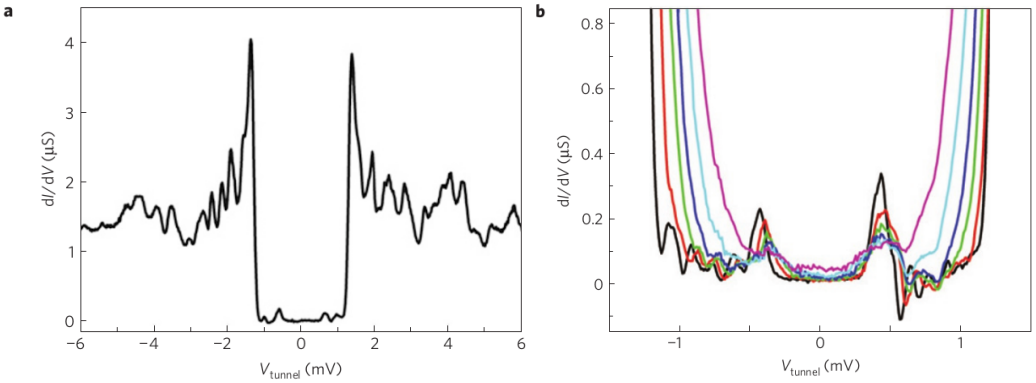

Figure 2.4: The experimental evidence for Andreev bound states (ABS) in graphene quantum dot: a) the differential tunnelling conductance versus bias voltage, b) in-gap states observed for different temperatures: 0.26, 0.45, 0.67, 0.86, 1.25 and 1.54 K [109].

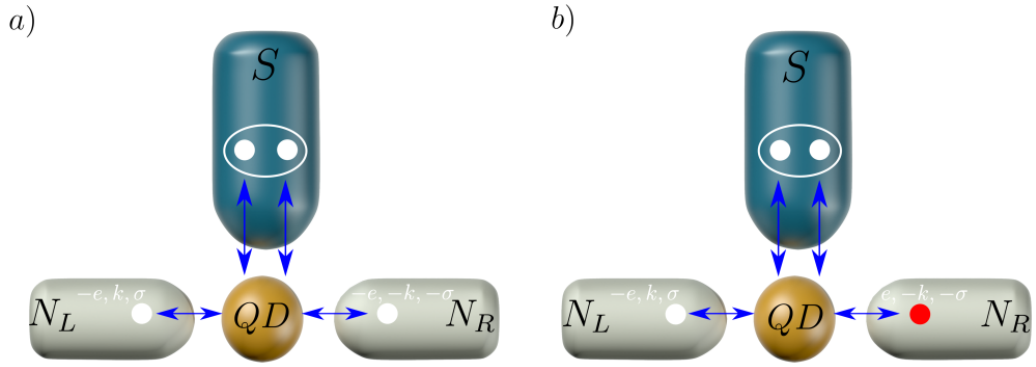

Figure 2.5: Schematic visualization of the multiterminal junction showing: a) Direct Andreev Refflection (DAR), b) Crossed Andreev Reflection (CAR) processes.

We presented a few examples of devices based on quantum dots and

possible scenarios of charge transport. In this thesis, we consider only two-terminal nanojunctions with the single and double quantum dot. Their theoretical investigation will be presented in the next chapters.

Chapter 3

Dynamics of Andreev states in single quantum dot system

This chapter describes dynamical properties of a single quantum dot placed between the metallic and the superconducting leads (N-QD-S), schematically presented in Fig. 3.1. We would like to investigate the time-dependent processes accompanying the formation of Andreev bound states in the system caused by the connection of circuit elements to each other. We identify their features and behavior depending on the system properties and initial conditions and determine the time necessary to reach equilibrium or steady-state by the system. Further, we investigate how changes in system settings affect the Andreev bound states. We analyse the evolution of the system after these changes, which reveals a number of new physical phenomena. In this chapter, we present results of time-dependent charge current and differential conductance, which could be experimentally examined. In what follows, we investigate the dynamics imposed by: transient effects (Sec. 3.4), rapid application of source-drain voltage (Sec. 3.5), quench in the orbital level (Sec. 3.6) and quench in coupling to superconducting lead (Sec. 3.7). Moreover, this chapter includes the theoretical description of the mathematical method based on the Heisenberg equations of motion technique (Sec. 3.3), used to

determine the time-evolution of the system.

3.1 Model Hamiltonian

The quantum dot (QD) coupled on one side to the metallic (N) and on the other side to the superconducting (S) reservoirs (Fig. 3.1) can be described by the second quantization Hamiltonian

$$\hat{H} = \hat{H}_{QD} + \hat{H}_N + \hat{H}_{N-QD} + \hat{H}_S + \hat{H}_{S-QD}. \tag{3.1}$$

The quantum dot part is given by

$$\hat{H}_{QD} = \sum_{\sigma} \varepsilon_d \hat{d}^{\dagger}_{\sigma} \hat{d}_{\sigma} + U\ \hat{n}_{\uparrow}\hat{n}_{\downarrow} \tag{3.2}$$

where ε_d is its discrete energy level, $\hat{d}^{\dagger}_{\sigma}$ ($\hat{d}_{\sigma}$) is creation (annihilation) operator of the quantum dot electron with spin $\sigma = \{\uparrow, \downarrow\}$. The second part of (3.2) is an interaction term describing the Coulomb repulsion U between the electrons with the opposite spin, where $\hat{n}_{\sigma} = \hat{d}^{\dagger}_{\sigma}\hat{d}_{\sigma}$ is a particle number operator.

The normal metallic lead is described as the free fermionic gas

$$\hat{H}_N = \sum_{k\sigma} \varepsilon_{k\sigma} \hat{c}^{\dagger}_{k\sigma} \hat{c}_{k\sigma}, \tag{3.3}$$

where summation is over the energy $\varepsilon_{k\sigma}$ of electrons with wave-vector k and spin σ. In the system, the hybridization between the quantum dot and external lead is expressed by

$$\hat{H}_{N-QD} = \sum_{k\sigma} V_k \left(\hat{c}^{\dagger}_{k\sigma} \hat{d}_{\sigma} + h.c. \right), \tag{3.4}$$

where V_k denotes the coupling of itinerant electrons with quantum dot.

The superconducting effects are considered by the BCS-type Hamiltonian

$$\hat{H}_S = \sum_{q\sigma} \varepsilon_{q\sigma} \hat{c}^{\dagger}_{q\sigma} \hat{c}_{q\sigma} - \sum_{q} \left(\Delta_{sc} \hat{c}^{\dagger}_{q\uparrow} \hat{c}^{\dagger}_{-q\downarrow} + \text{h.c.} \right), \tag{3.5}$$

where Δ_{sc} denotes the pairing energy gap. The hybridization between the quantum dot and superconducting lead is described by

$$\hat{H}_{S-QD} = \sum_{q\sigma} V_q \left(\hat{c}^{\dagger}_{q\sigma} \hat{d}_{\sigma} + h.c. \right) \tag{3.6}$$

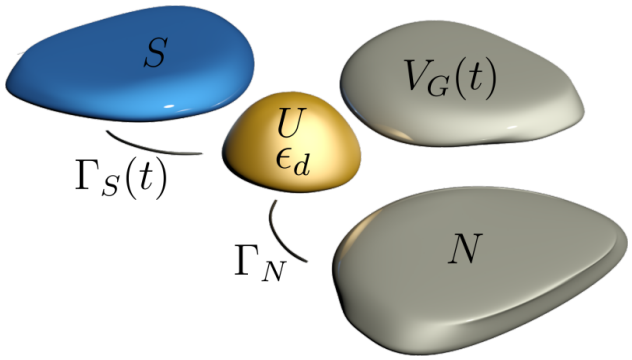

Figure 3.1: Illustration of single quantum dot placed between the normal (N) and the superconducting (S) reservoirs. The energy level of QD can be controlled by the additional gate V_G, U is the Coulomb repulsion potential and $\Gamma_{N/S}$ are couplings to the external reservoirs [110].

with an appropriate coupling constant V_q. Assuming this gap Δ_{sc} as the largest energy scale in the system, we will focus on the processes in the subgap regime. Under such conditions the fermionic degrees of freedom can be integrated out, resulting in the low-energy physics described by [111, 112]

$$\hat{H}_{QD} + \hat{H}_S + \hat{H}_{S\text{-}QD} \approx \sum_\sigma \varepsilon_d \hat{d}^\dagger_\sigma \hat{d}_\sigma + U\, \hat{n}_\uparrow \hat{n}_\downarrow + \frac{\Gamma_S}{2}\left(\hat{d}_\downarrow \hat{d}_\uparrow + \text{h.c.}\right), \tag{3.7}$$

where $\Gamma_S/2$ plays a role of the effective pairing potential induced in quantum dot [61]. For simplicity, we consider the energy-independent coupling $\Gamma_S = 2\pi \sum_q |V_q|^2 \delta\left(\varepsilon - \varepsilon_q\right)$ in the wide-band limit approximation.

3.2 Selected experimental realizations

Presently available techniques for fabrication of nanostructures allow to create various devices based on the quantum dots. As an example, we present a few of such systems. The popular way to construct a nanojunction based on a single quantum dot is STM (scanning tunneling microscope). Using STM tip one can deposit either a single atom or a cluster of atoms on a surface of arbitrary material. This approach allows to control the coupling strength between the quantum dot and the surface by defining the

distance between them. It gives the possibility to study the bound states inside the superconducting energy gap by conductance spectroscopy [113]. Another example, Fig. 3.2a (discussed in Ref. [114]) presents multiterminal heterostructure composed of the carbon nanotube (CNT) partially covered by superconducting layer (S) of Pb. The carbon nanotube is connected on both sides to electrodes made of Pd (N_1, N_2). In the system, SG_1 and SG_2 are palladium controlling gates. The manufactured system presented in Fig. 3.2a can work as the simple normal metal-quantum dot-superconductor heterostructure and as the Cooper pair splitter [105], depending on the controlling gate potentials. Another example of N-QD-S system is presented

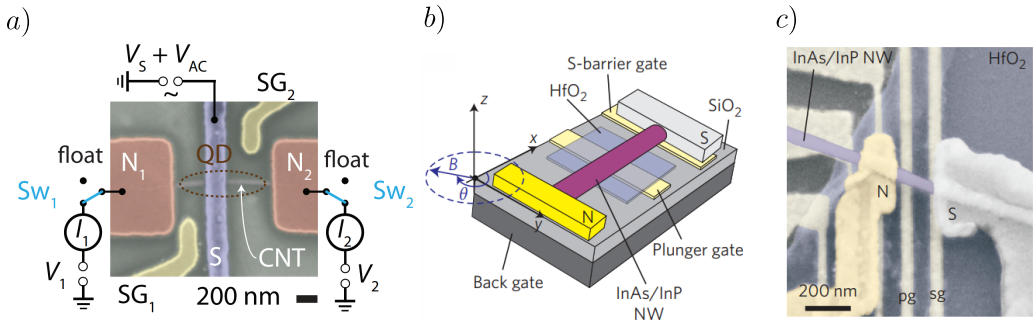

Figure 3.2: The experimental realisations of single quantum dot system. Panel *a*) presents the single quantum dot system based on the carbon nanotube [114]. Panel *b*) is schematic visualization of the single quantum dot system made of InAs/InP nanowire presented in panel *c*) [115].

in Fig. 3.2b,c [115]. The middle panel is a schematic visualization of the manufactured system presented in the right side panel. In this case, the system is made of the InAs/InP nanowire covered by the gold (N) and vanadium (S) leads. Under the nanowire the plunger-gate (pg) and superconductor-barrier gate (sg) are located.

3.3 Equations of motion approach

For investigating the evolution of any observable $\hat{O}(t)$ we use the following equation of motion

$$i\frac{d\hat{O}(t)}{dt} = \frac{1}{\hbar}[\hat{O}(t), \hat{H}] + i\frac{\delta}{\delta t}\hat{O}(t). \tag{3.8}$$

In particular, the time-dependent charge current flowing between QD and metallic lead $j_{N\sigma}(t)$ can be found from the Heisenberg equation of motion for the particle number operator $\hat{n}_{k\sigma}(t) = \hat{c}^{\dagger}_{k\sigma}(t)\hat{c}_{k\sigma}(t)$. The current flowing in the superconducting reservoir $j_{S\sigma}(t)$ and occupancy of the quantum dot $n_{\sigma}(t) = \langle \hat{n}_{\sigma}(t) \rangle$, can be indirectly calculated from the charge conservation law $\frac{d}{dt}n_{\sigma}(t) = j_{N\sigma}(t) + j_{S\sigma}(t)$.

We start from the momentum and spin dependent current $j_{Nk\sigma}(t)$ defined as the time derivative of the statistical average for the particle number operator $\langle \hat{n}_{k\sigma}(t) \rangle$

$$j_{Nk\sigma}(t) = -e\frac{d}{dt}\langle \hat{n}_{k\sigma}(t) \rangle = -\frac{ie}{\hbar}\left\langle [\hat{H}, \hat{n}_{k\sigma}(t)] \right\rangle. \tag{3.9}$$

Substituting the commutator

$$\left[\hat{H}, \hat{n}_{k\sigma}(t)\right] = -V_k\hat{c}^{\dagger}_{k\sigma}(t)\hat{d}_{\sigma}(t) + V_k\hat{d}^{\dagger}_{\sigma}(t)\hat{c}_{k\sigma}(t) \tag{3.10}$$

into (3.9) we obtain

$$j_{Nk\sigma}(t) = \frac{ie}{\hbar}\langle V_k\hat{c}^{\dagger}_{k\sigma}(t)\hat{d}_{\sigma}(t) - V_k\hat{d}^{\dagger}_{\sigma}(t)\hat{c}_{k\sigma}(t) \rangle. \tag{3.11}$$

Subtracting the conjugated numbers $z - z^{*} = 2i\,\mathrm{Im}(z)$ gives us the current formula for charge current

$$j_{Nk\sigma}(t) = \frac{2e}{\hbar}\,\mathrm{Im}\left(\langle V_k\hat{d}^{\dagger}_{\sigma}(t)\hat{c}_{k\sigma}(t) \rangle\right). \tag{3.12}$$

The total charge current contributed by all electrons is obtained by summation over momenta k

$$j_{N\sigma}(t) = \frac{2e}{\hbar}\,\mathrm{Im}\left(\sum_k V_k\langle \hat{d}^{\dagger}_{\sigma}(t)\hat{c}_{k\sigma}(t) \rangle\right). \tag{3.13}$$

At this step, the current formula depends on the quantum statistical averaging of operators $\langle \hat{d}_\sigma^\dagger(t)\hat{c}_{k\sigma}(t)\rangle$, which is not trivial problem to solve. One possible route to obtain this relies on expanding the operator $\hat{c}_{k\sigma}(t)$ into sum of the initial $\hat{c}_{k\sigma}(0)$ and additional terms, emerging during evolution of the system. The equation of motion for annihilation operator $\frac{d}{dt}\hat{c}_{k\sigma}(t) = i[\hat{H}, \hat{c}_{k\sigma}(t)]$ (for $\hbar = 1$) yields

$$\frac{d}{dt}\hat{c}_{k\sigma}(t) + i\varepsilon_{k\sigma}\hat{c}_{k\sigma}(t) = -iV_k\hat{d}_\sigma(t). \tag{3.14}$$

We can express (3.14) as a differential equation of the form

$$\frac{dy(x)}{dx} + f(x)x = y(x), \tag{3.15}$$

which has a general solution

$$y(t) = y(0)e^{-\int_0^x f(x')dx'} + \int_0^x g(x')e^{-\int_{x'}^x f(x'')dx''}. \tag{3.16}$$

Thus, the explicit formula for time-dependent operator $\hat{c}_{k\sigma}(t)$ takes the form

$$\hat{c}_{k\sigma}(t) = \hat{c}_{k\sigma}(0)e^{-i\int_0^t \varepsilon_{k\sigma}(t')dt'} - i\int_0^t dt' V_k e^{-i\int_{t'}^t \varepsilon_{k\sigma}(t'')dt''}\hat{d}_\sigma(t'). \tag{3.17}$$

Substituting (3.17) into (3.13), we obtain the total current expressed by following equation

$$j_{N\sigma}(t) = \frac{2e}{\hbar}\sum_k \mathrm{Im}\left(\tilde{V}_k(t)\langle \hat{d}_\sigma^\dagger(t)\hat{c}_{k\sigma}(0)\rangle - i\int_0^t dt'\tilde{V}_k^*(t')\tilde{V}_k(t)\langle \hat{d}_\sigma^\dagger(t)\hat{d}_\sigma(t')\rangle\right), \tag{3.18}$$

where $\tilde{V}_k(t) = V_k e^{-i\int_0^t \varepsilon_{k\sigma}(t')dt'}$ denotes the time-dependent coupling to the metallic lead and $\tilde{V}_{k\sigma}^*(t')\tilde{V}_{k\sigma}(t) = |V_k|^2 e^{-i\int_{t'}^t \varepsilon_{k\sigma}(t'')dt''}$ is a product of the time-dependent couplings at different times. In the wide-band limit approximation, assuming constant energy levels in time $\varepsilon_{k\sigma}(t) = \varepsilon_{k\sigma}$, the hybridization function $\tilde{V}_{k\sigma}^*(t')\tilde{V}_{k\sigma}(t)$ appearing in (3.18) simplifies to [116]

$$\sum_k |V_k|^2 e^{-i\int_{t'}^t \varepsilon_{k\sigma}(t'')dt''} = \sum_k |V_k|^2 e^{-i\int_{t'}^t \varepsilon_{k\sigma}dt''} = \frac{\Gamma_N}{2}\delta(t-t'), \tag{3.19}$$

where $\Gamma_N = 2\pi\sum_k |V_k|^2\delta(\varepsilon - \varepsilon_k)$ is the coupling to metallic lead.

Finally, one obtains the charge current expressed in the general form

$$j_{N\sigma}(t) = 2\,\mathrm{Im}\left[\sum_k V_k e^{-i\varepsilon_{k\sigma}t}\langle\hat{d}^\dagger_\sigma(t)\hat{c}_{k\sigma}(0)\rangle - \frac{i\Gamma_N}{2}\langle\hat{n}_\sigma(t)\rangle\right]. \tag{3.20}$$

To calculate the current $j_{N\sigma}(t)$ we have to solve numerically a set of coupled differential equations for the expectation values: $\langle\hat{n}_\sigma(t)\rangle$, $\langle\hat{d}_\downarrow(t)\hat{d}_\uparrow(t)\rangle$, $\langle\hat{d}^\dagger_\uparrow(t)\hat{c}_{k\uparrow}(0)\rangle$, $\langle\hat{d}^\dagger_\downarrow(t)\hat{c}_{k\downarrow}(0)\rangle$, $\langle\hat{d}_\uparrow(t)\hat{c}_{k\downarrow}(0)\rangle$ and $\langle\hat{d}_\downarrow(t)\hat{c}_{k\uparrow}(0)\rangle$. Explicit form of the individual functions is presented in Appendix A.1. Such method allows to investigate the time-dependent properties of the order parameter function $\chi(t) = \langle\hat{d}_\downarrow(t)\hat{d}_\uparrow(t)\rangle$, which characterizes evolution of the on-dot electron pairing.

For numerical purposes we use the Runge-Kutta of 4th order, assuming various initial conditions for occupancy of the quantum dot $n_\sigma(t = 0)$.

3.4 Transient effects and steady-state properties

To demonstrate dynamics of the Andreev bound states we first consider their buildup after suddenly connecting the quantum dot to external reservoirs. Processes accompanying the evolution from the initial conditions to the equilibrium state, when the steady properties are established, can be regarded as transient effects. For computational reasons it is convenient to assume that initially, at $t = 0$, the quantum dot is disconnected from both external reservoirs and it is connected to the system constituents at $t = 0^+$. Fig. 3.3 presents numerical results obtained for currents $j_{N\uparrow}(t)$, $j_{S\uparrow}(t)$, occupancy of quantum dot $n_\uparrow(t)$ and the real part of the order parameter $\chi(t)$. Imaginary par of $\chi(t)$ is negligibly small in comparison to $|\mathrm{Re}\chi(t)|$. We observe the evolution of the system (in absence of source-drain voltage) towards the steady state dependent on various initial quantum dot occupancy. The initial occupancy affects the transient currents and the charge accumulated in the quantum dot over time, as can be seen in their plots. If initially, the quantum dot is empty, we observe quantum oscillations due to the flow of Cooper

pairs back and forth between the quantum dot and the superconductor. In another case, when the quantum dot is initially occupied by a single electron, we observe gradual filling of quantum dot by electrons from the normal lead, because the Cooper pairs cannot flow onto the quantum dot. The relaxation processes originate from the coupling of the quantum dot to a continuum of electrons of the metallic lead. For the transient currents, the envelope functions is described by $e^{-\Gamma_N t}$ [117]. We also observe that the initial occupancy of the quantum dot does not affect creation of an on-dot pairing.

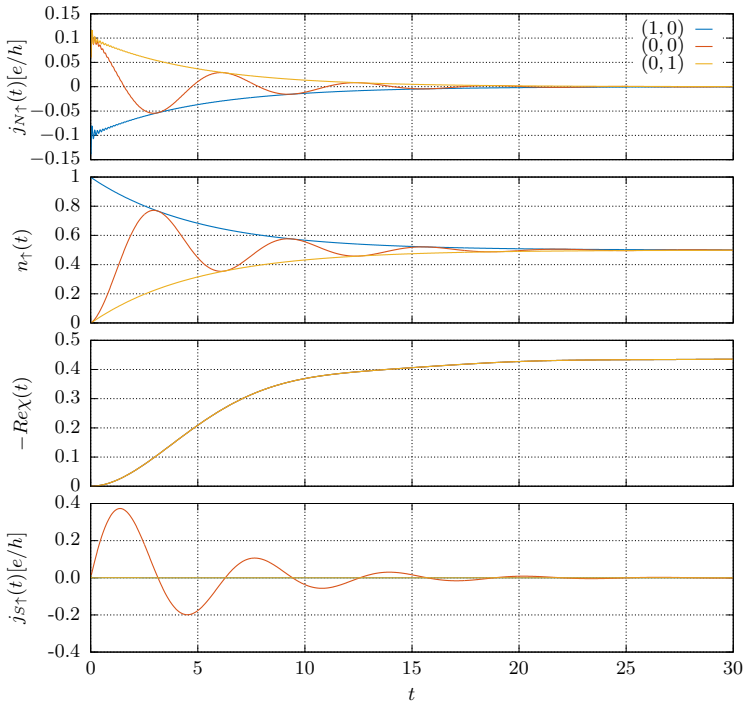

Figure 3.3: The transient evolution of currents $j_{N\uparrow}(t)$, $j_{S\uparrow}(t)$, occupancy $n_\uparrow(t)$ and the order parameter $\mathrm{Re}\,\chi(t)$, imposed by a sudden coupling of the quantum dot to both external leads at $t = 0^+$ for various initial occupancy $(n_\uparrow(0), n_\downarrow(0))$. The results are obtained for zero source-drain voltage and system parameters: $\varepsilon_d = 0$, $U = 0$, $\Gamma_N = 0.2$, $\Gamma_S = 1$.

The oscillating character of evolution is reminiscent of the Rabi oscillations of two-level quantum system. At time $t = 0$, the quantum dot is characterized

by the single energy peak at ε_d. Then for the time $t > 0$, the quantum dot energy level evolves into a pair of Andreev bound states at energies $E_A = \pm\sqrt{\varepsilon_d^2 + (\Gamma_S/2)^2}$. Those quantum oscillations are caused by fluctuations in the occupancy of these two-level system. In the transient evolution, the activation of quantum oscillations strictly depends on the initial conditions (for analytical reasoning see Ref. [117]). They are not observed if the initial configuration $[n_\uparrow(0), n_\downarrow(0)]$ is singly occupied $(1,0)$ or $(0,1)$, as shown in Fig. 3.3.

Empirical observation of the Andreev states formation can be done by the differential conductance $G_N(V,t) = \frac{d}{dV} j_{N\uparrow}(t)$ of the charge current flowing between the quantum dot and the metallic lead, when the chemical potential of the normal lead μ_N is detuned from μ_S by an applied source-drain voltage $eV = \mu_N - \mu_S$. We assume the superconductor to be grounded, $\mu_S = 0$. The voltage is imposed at $t = 0$. Fig. 3.4 shows the differential conductance G_N (in

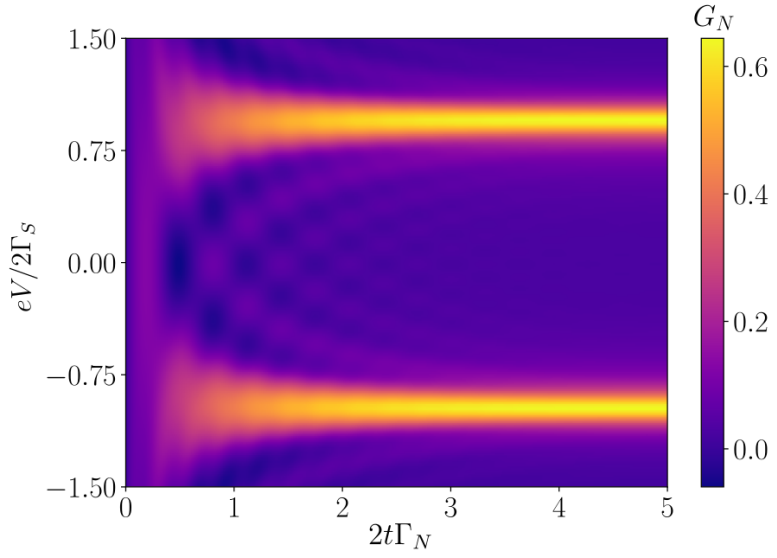

Figure 3.4: Evolution of the differential conductance G_N (in units of $2e^2/h$) with respect to source-drain voltage V and time t, after a sudden coupling of the quantum dot to both external leads at $t = 0^+$. For computation we used: $\varepsilon_d = 0$, $U = 0$, $\Gamma_N = 0.05$, $\Gamma_S = 1$.

units of $2e^2/h$) with respect to the source-drain voltage V and time t. In this particular uncorrelated case of quantum dot system, where $\varepsilon_d = 0$, we observe formation of the Andreev bound states localized symmetrically with respect to the chemical potential, at energies $E_A = \pm\Gamma_S/2$. Emergence of the Andreev peaks has an oscillating character with period $2\pi/E_A$, damped in time. Their damping is governed by the envelope function $e^{-\Gamma_N t}$ and originates form the coupling of the quantum dot to the continuum of free electrons of the metallic lead [117].

To calculate the conductance in the correlated quantum dot system by Heisenberg's equations of motion technique we adapt mean-field approximation, suitable for a weakly correlated system. Using the Hartree-Fock-Bogoliubov (HFB) approximation the Coulomb repulsion term in (3.2) can be written as

$$\begin{aligned} \hat{d}_\uparrow^\dagger \hat{d}_\uparrow \hat{d}_\downarrow^\dagger \hat{d}_\downarrow &\simeq n_\uparrow(t)\hat{d}_\downarrow^\dagger \hat{d}_\downarrow + n_\downarrow(t)\hat{d}_\uparrow^\dagger \hat{d}_\uparrow - n_\uparrow(t)n_\downarrow(t) \\ &+ \chi(t)\hat{d}_\uparrow^\dagger \hat{d}_\downarrow^\dagger + \chi^*(t)\hat{d}_\downarrow \hat{d}_\uparrow - |\chi(t)|^2 . \end{aligned} \tag{3.21}$$

The Hartree-Fock term can be included in the renormalized quantum dot energy level $\tilde{\varepsilon}_d \equiv \varepsilon_d + U n_{-\sigma}(t)$ and the anomalous contribution rescales the effective pairing potential $\tilde{\Gamma}_S \equiv \Gamma_S - 2U\chi(t)$ of the induced order parameter potential $\chi(t) = \langle \hat{d}_\downarrow(t)\hat{d}_\uparrow(t)\rangle$.

Fig. 3.5 presents the results obtained for weakly correlated heterostructure. Here, the top and bottom panels show the results for Coulomb repulsion $U = 0.25$ and $U = 1$, respectively. Both panels refer to particle-hole symmetry ($\varepsilon_d = -U/2$), when the quantum dot is half-filled in the steady state limit. Like in the uncorrelated case, the differential conductance G_N evolves towards its steady-state limit, exhibiting emergence of the bound states around $E_A = \pm\sqrt{(\varepsilon_d + U/2)^2 + (\Gamma_S/2)^2}$. Relaxation processes are governed by function $e^{-\Gamma_N t}$ and the quantum oscillations have the period $2\pi/E_A$.

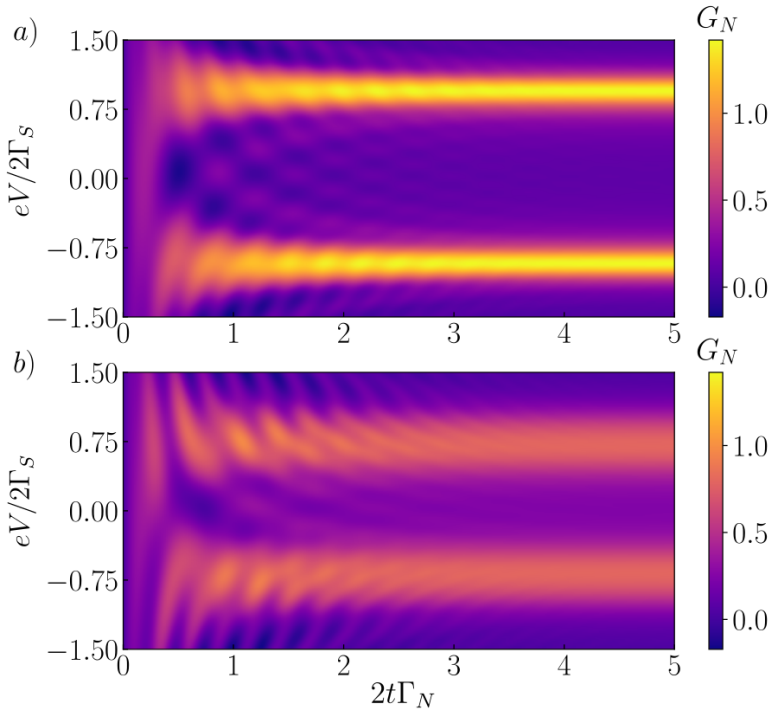

Figure 3.5: Evolution of the differential conductance G_N (in units of $2e^2/h$) with respect to voltage V and time t, after a sudden coupling of the quantum dot to both external leads at $t > 0$ treating the electron correlation effects by the mean-field approximation. In panel a) $U = 0.25$ and b) $U = 1$. The other model parameters are: $\Gamma_N = 0.05$, $\Gamma_S = 1$, $\varepsilon_d = -U/2$ [110].

3.5 Influence of suddenly varied source-drain voltage

Transient evolution of the uncorrelated system has been characterized by the time-dependent observables shown in Fig. 3.3 and conductance shown in Fig. 3.4. To have a deeper insight into the time-dependent observables after the perturbation, let us discuss separately the plots of $j_{N\sigma}(t)$, $j_{S\sigma}(t)$ presented in Fig. 3.6. Until $t = 30/\Gamma_S$, we display the transient evolution caused by abrupt coupling of the quantum dot to the external leads of unbiased junction. The damped quantum oscillations are controlled by the coupling Γ_N to the normal lead [117, 118], what is visible in the analytic formulas for

the observables:

$$j_{S\sigma}(t) = \frac{\Gamma_S}{2} \sin(\Gamma_S t)\, e^{-\Gamma_N t}, \tag{3.22}$$

$$j_{N\sigma}(t) = \frac{\Gamma_N}{2} \sin(\Gamma_S t + \varphi_0)\, e^{-\Gamma_N t}, \tag{3.23}$$

where φ_0 denotes the phase shift between the currents. When the system reaches its equilibrium we apply source-drain voltage to the system at $t = 30/\Gamma_S$. We assume step-like change of the chemical potential $\mu_N \to \mu_N + \Delta\mu_N$ at $t = 30/\Gamma_S$. In Fig. 3.6, the evolution exhibits quantum beats appearing in the current $j_{N\sigma}(t)$.

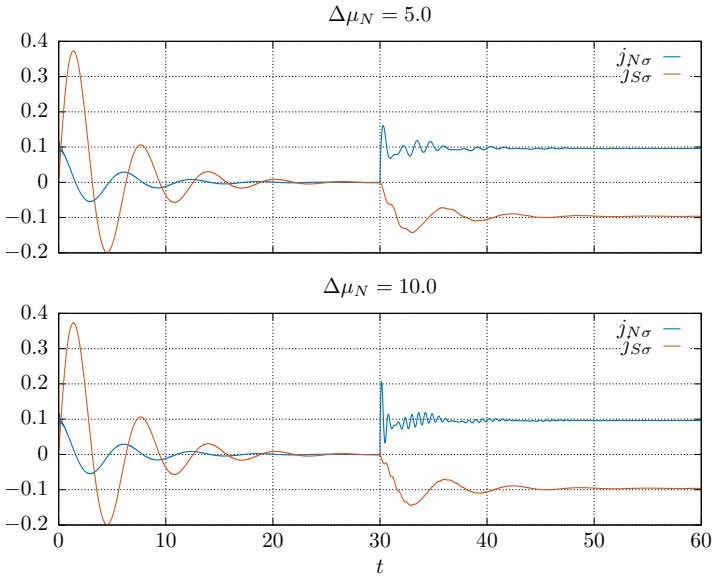

Figure 3.6: The transient evolution of currents (in units of e/h), after a sudden coupling of the quantum dot to both external leads at $t = 0^+$ and their evolution after the jump of chemical potential level $\mu_N \to \mu_N + \Delta\mu_N$ at $t \geq 30$. The other model parameters: $\mu_N = 0$, $\Gamma_N = 0.2$, $\Gamma_S = 1$, $\varepsilon_d = 0$, $U = 0$ [119].

At this point, we would like to recall the essential properties of the quantum dot system without the presence of superconductor. It has been shown that the abrupt change of the source-drain voltage has significant influence on the current flowing through the quantum dot placed between

normal leads [120–122]. After the sudden application of the source-drain voltage, the time-dependent current structure shows the coherent oscillations with the frequency $\omega = |\mu_N - \varepsilon_d|$.

In our system, the proximitized quantum dot is characterized by a pair of in-gap bound states with energies $\pm\Gamma_S/2$, therefore the current $j_{N\sigma}(t)$ is a superposition of two contributing currents with the frequencies $\omega_{1/2} = \mu_N \pm \Gamma_S/2$, respectively. In consequence, the current $j_{N\sigma}(t)$ is combination of the high frequency component $\omega = \mu_N$ and the low frequency beats with the time period $T = 2\pi/\Gamma_S$. Moreover, we notice that the current $j_{S\sigma}(t)$ oscillates with only lower frequency. Difference between these two currents is caused by the time-dependent occupancy of the quantum dot, obeying the local charge conservation $\frac{d}{dt}n_\sigma(t) = j_{N\sigma}(t) + j_{S\sigma}(t)$.

Analysis of the experimentally measured time-dependent current can indirectly give information about the coupling strength between the quantum dot and the superconducting reservoir, by determining the period of current oscillations $\Gamma_S = 2\pi/T$.

3.6 Quench in orbital level position

Let us consider influence of the quench imposed on the quantum dot energy level. In this scenario, we abruptly change the quantum dot energy level $\varepsilon_d \to \varepsilon_d + \Delta\varepsilon_d$ at time $t = 30/\Gamma_S$ (like previously, after the transient processes are completed) and observe the system's response with completely different behaviour of evolution for all observables (Fig. 3.7). The post-quench evolution exhibits the oscillatory structure of all observables. The oscillations depend on the energy level of the quantum dot and the coupling to the superconducting lead $T = 2\pi/\sqrt{\Gamma_S^2 + 4(\Delta\varepsilon_d)^2}$ [117]. In absence of the source-drain voltage ($\mu_N = \mu_S$), the oscillations gradually disappear over sufficiently long time and the currents $j_{S\sigma}$, $j_{N\sigma}$ vanish. In evolution after the sudden shift of quantum dot energy level, the envelope function has exponential form

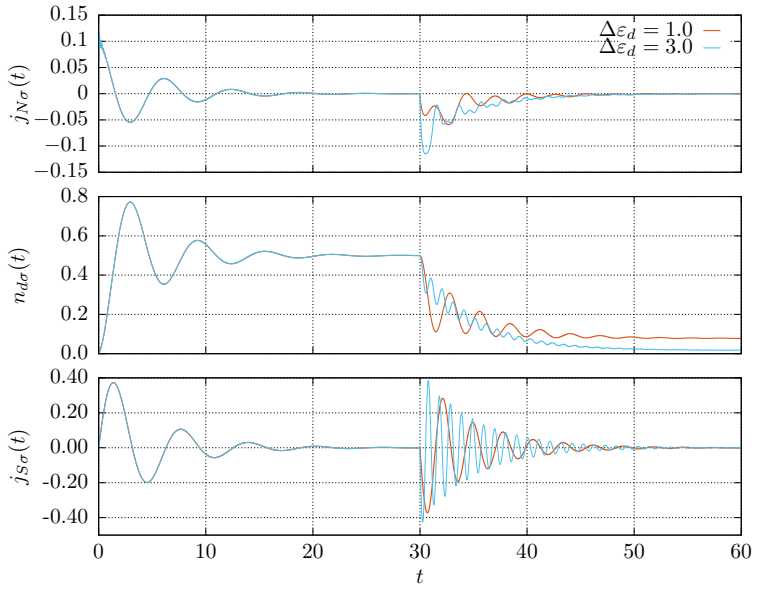

Figure 3.7: The transient evolution of currents (in units of e/h), imposing a sudden coupling of the quantum dot to both external leads at $t = 0^+$ and their the post-quench evolution after the jump of the quantum dot energy level $\varepsilon_d \to \varepsilon_d + \Delta\varepsilon_d$ at $t \geq 30$. The other model parameters: $\mu_N = 0$, $\Gamma_N = 0.2$, $\Gamma_S = 1$, $\varepsilon_d = 0$, $U = 0$ [119].

$\sim e^{-\Gamma_N \bar{t}}$ (where $\bar{t} = t - 30/\Gamma_S$ denotes the time measured from the quench of ε_d).

Influence of electron correlations

We now consider the Coulomb repulsion U between two electrons and its influence on the post-quench evolution induced by the shift of the quantum dot energy level. In the system with the correlated quantum dot, the orbital energy level $\varepsilon_d = -U/2$ corresponds to the particle-hole symmetry point and it is convenient to take this value as the initial condition. Fig. 3.8 shows the evolution of physical observables after the quantum dot energy level is changed from $\varepsilon_d = -U/2$ to its final value ε_d indicated on the y-axis.

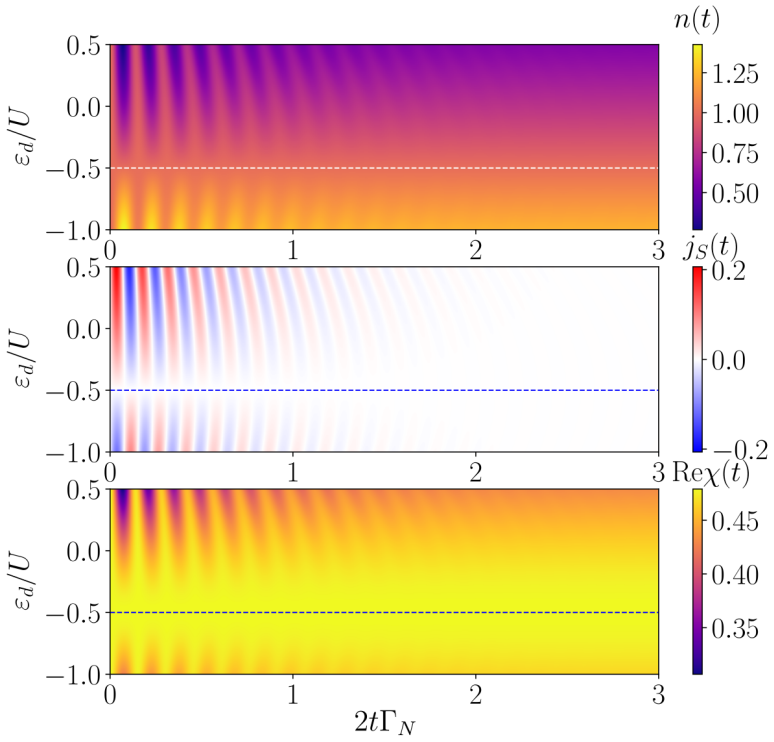

Figure 3.8: The time-dependent quantum dot's occupation $n(t)$, current $j_S(t)$ and the real part of $\langle \hat{d}_\downarrow(t)\hat{d}_\uparrow(t)\rangle$, after a sudden quench in quantum dot energy level from $\varepsilon_d(t \leq 0) = -U/2$ to $\varepsilon_d(t > 0) = \varepsilon_d$. The other model parameters: $\Gamma_N = 0.05$, $\Gamma_S = 4$ and $U = 1$ [110].

In this case of strongly coupled quantum dot to the superconducting lead ($\Gamma_S/U = 4$), the evolution presents the damped oscillating behaviour of observables, similarly like without correlations. The amplitude of the oscillation increases with a greater difference between the quantum energy level before and after the quench $|\varepsilon_d(t \leq 0) - \varepsilon_d(t > 0)|$. The more the energy levels are shifted away from the levels before the change, the stronger we disturb the system, making its response more intense. This is better noticeable as we move away from the particle-hole symmetry point (indicated by the dashed line). When the occupancy of the quantum dot is far from half-filling, the Cooper pair can flow back and forth between the quantum dot and the superconducting lead, what is visible by the well pronounced oscillations in

the observables. Since QD spectrum consists of pairs of the Andreev bound states at $\pm E_A$ these dynamical processes are reminiscent of the two-level Rabi oscillations. As in the uncorrelated case, the damping process occurs with a relaxation rate $\tau \sim 1/\Gamma_N$. What is relevant, the perturbation in the quantum dot energy level affects the post-quench state of the system in the long time limit. For example, the occupancies tend to stationary value $n(t \to \infty) \approx 0.57$, for the final QD energy $\varepsilon_d/U = 0.5$ and $n(t \to \infty) \approx 1.23$, for $\varepsilon_d/U = -1$, respectively.

Another feature appearing in post-quench evolution is π-shift of the oscillations upon crossing the half-filling level $\varepsilon_d = -U/2$, marked by the dashed lines in Fig. 3.8. This phenomenon resembles the $0-\pi$ *transition* reported for Josephson junctions under stationary conditions [123, 124]. The oscillatory behaviour is also visible in the real part of the time-dependent order parameter $\chi(t)$, which can be regarded as a quantitative measure of the on-dot pairing. In a short time after the quench, the value of $\mathrm{Re}\chi(t)$ oscillates with significant amplitude.

In the case, when the quantum dot is weakly coupled to the superconducting lead, $\Gamma_S/U = 1$, we observe significant modifications of the oscillatory time-dependent quantities (see Fig. 3.9). In particular, the weaker the coupling strength Γ_S enlarges the period of the oscillations of all quantities. We observe that the final value of the quantum dot energy level after the quench has an extensive effect on the frequency. For a larger value of $|\varepsilon_d(t \le 0) - \varepsilon_d(t > 0)|$ the shift of frequency to higher values is visible. Moreover, it is important to notice that the change of Γ_S has no impact on amplitude range of the superconducting current $j_S(t)$. Smaller value of Γ_S is equivalent to the lesser value of the on-dot pairing potential. The change of Γ_S affects the final values of the other quantities. For example, $n(t \to \infty) \approx 0.2$ for the quench to $\varepsilon_d/U = 0.5$ and $n(t \to \infty) \approx 1.55$ for $\varepsilon_d/U = -1$, exceed the range of the occupation number in Fig. 3.8.

In addition, to complete our investigation of the system evolution after

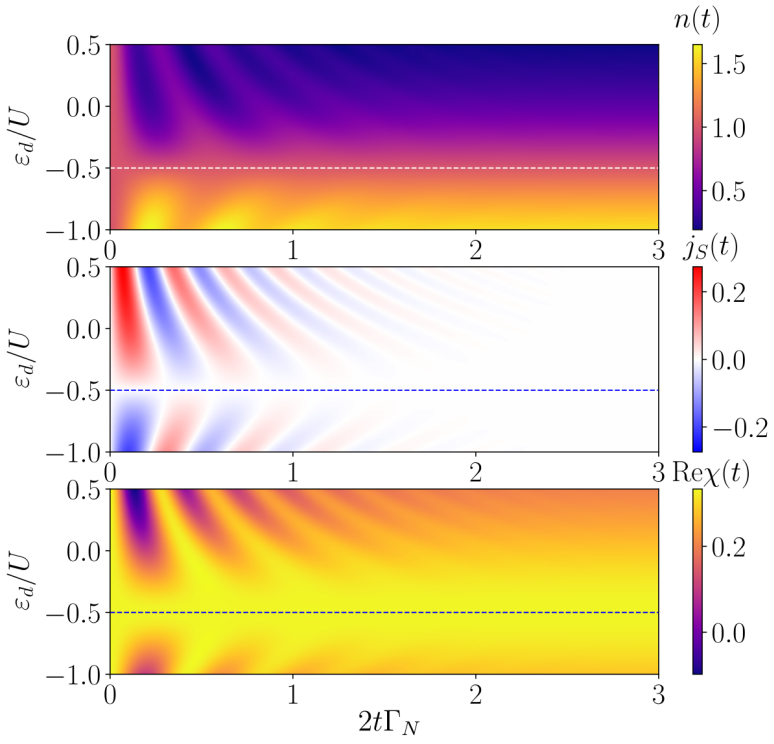

Figure 3.9: The time-dependent quantum dot's occupation $n(t)$, current $j_S(t)$ and the real part of $\langle \hat{d}_\downarrow(t)\hat{d}_\uparrow(t)\rangle$, after a quench in quantum dot's energy level from $\varepsilon_d(t \leq 0) = -U/2$ to $\varepsilon_d(t > 0) = \varepsilon_d$. The other model parameters: $\Gamma_N = 0.05$, $\Gamma_S = 1$, $U = 1$ [110].

shifting the quantum dot energy level we present the differential conductance G_N diagram in Fig. 3.10. In this plot, we demonstrate the evolution of Andreev states and their steady state positions after the shift of the energy level $\varepsilon_d = U/2 \to -U/2$. We visualize the post-quench evolution in the wide spectrum of the source-drain voltage. After the sudden jump of the quantum dot energy level $\varepsilon_d = U/2 \to -U/2$ we observe a similar response of the system like in previous cases. In particular, the quantum oscillations of the differential conductance are damped in time and the Andreev bound states emerge with the same spectral weight located with respect to the chemical potential $\mu_N = eV$.

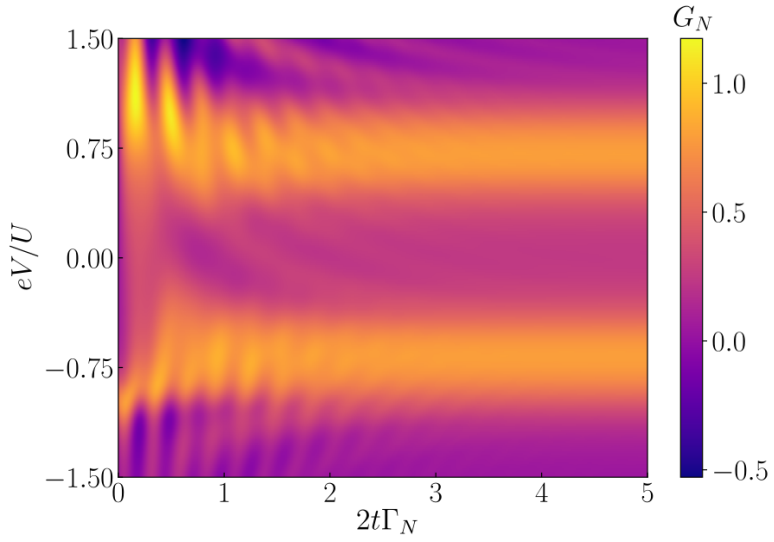

Figure 3.10: The post-quench evolution of the differential conductance G_N (in units of $2e^2/h$) with respect to voltage V and time t, after a sudden change of the quantum dot's energy level $\varepsilon_d = U/2 \to -U/2$ at $t = 0$. The other model parameters: $\Gamma_N = 0.05$, $\Gamma_S = 2$, $U = 1$ [110].

3.7 Response to sudden coupling Γ_S

For further understanding of the dynamics of the perturbed quantum dot system, we investigate another type of quench. In this section we look at evolution after a rapid coupling of the quantum dot to the superconducting lead. Let us remind the stationary solution for the system in the limit of $\Gamma_N = 0$ and $\Delta \to \infty$, where the model parameters ε_d, U and Γ_S determine character of QD ground state. The quantum dot ground state can exist in the singly occupied $|\sigma\rangle$ or in the BCS-type $u|0\rangle - v|\uparrow\downarrow\rangle$ configuration [125]. The border line between the doublet and singlet state occurs at

$$4\xi_d^2 + \Gamma_S^2 = U^2, \tag{3.24}$$

where $\xi_d = \varepsilon_d + U/2$. Crossing from one to another configuration is called a *quantum phase transition* [61] and plays an essential role in the interplay between the on-dot pairing and the correlation effects. Here, Fig. 3.11 shows

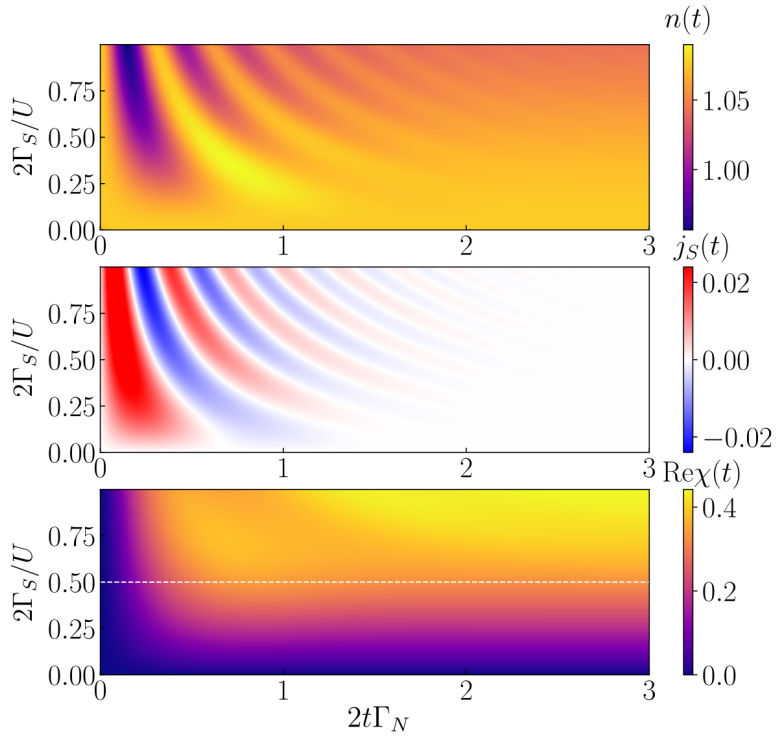

Figure 3.11: The time-dependent quantum dot's occupation $n(t)$, current $j_S(t)$ and the real part of $\langle \hat{d}_\downarrow(t)\hat{d}_\uparrow(t)\rangle$, after a quench in the coupling strength $\Gamma_S(t)$ from zero to its final value Γ_S. The other model parameters: $\varepsilon_d = -U/2 - U/20$, $\Gamma_N = 0.05$ [110].

the evolution of physical quantities after abrupt coupling of the quantum dot to superconducting lead, $0 \to \Gamma_S$, for the half-filled quantum dot ($\varepsilon_d = -U/2$) and weak coupling to the metallic reservoir, $\Gamma_N = 0.05$. As before, we observe the oscillating behaviour of the physical quantities in time, which is the result of the Cooper pairs leaking into the quantum dot and creating the Andreev states. In the system, the quantum phase transition occurs at $\Gamma_S = U$ when the quantum dot level $\varepsilon_d = -U/2$. In Fig. 3.11, by the white dashed line, we marked the theoretical border between the singly occupied and BCS-type ground state configurations. The quantum phase transition is clearly visible in change of $\mathrm{Re}\chi(t)$ in Fig. 3.11, where we observe development of the order

parameter after coupling quantum dot to the superconducting lead. In the doublet region ($\Gamma_S < U$) the order parameter has negligible values. In the same region for $j_S(t)$ (middle panel), we do not observe significant charge flow due to the dominant Coulomb repulsion. The singlet region appears for $\Gamma_S > U$, where the system relaxes to the BCS-type ground state through a sequence of damped quantum oscillations with significant amplitude right after the quench. For stronger coupling Γ_S we observe faster oscillations. The boundary between doublet and singlet states is not sharp. We observe a crossover rather than a transition between these configurations caused by the coupling $\Gamma_N \neq 0$.

Quench in the coupling to the superconducting lead can be analysed in the differential conductance plots. Fig. 3.12 presents the results obtained for $\Gamma_S = 0 \to 2$. For this specific scenario, we consider the half-filled quantum dot $\varepsilon_d = -U/2$ and set the Coulomb potential $U = 1$. Before the quench, the

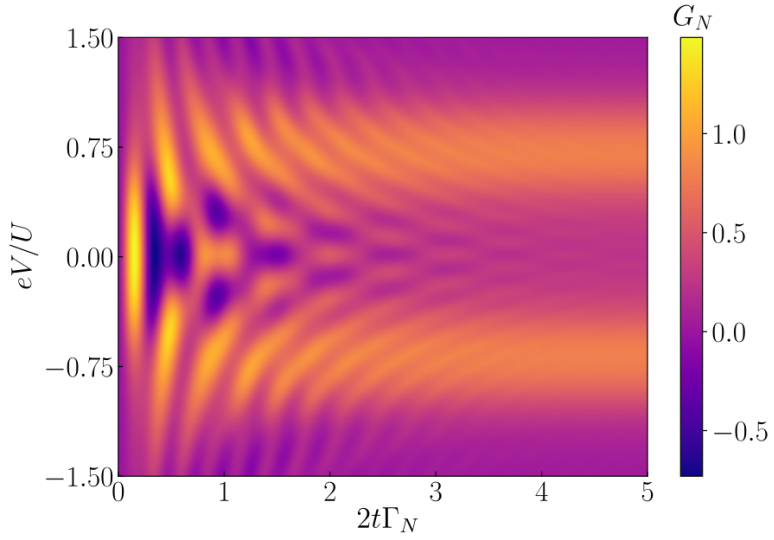

Figure 3.12: The post-quench evolution of the differential conductance G_N (in units of $2e^2/h$) with respect to voltage V and time t, imposed by a quench in hybridization strength $\Gamma_S = 0 \to 2$ at $t = 0$. The other model parameters: $\varepsilon_d = -U/2$, $\Gamma_N = 0.05$, $U = 1$ [110].

correlated quantum dot is characterized by two quasiparticle peaks at energies ε_d and $\varepsilon_d + U$. The rapid coupling to the superconducting lead induces the proximity effect which entails the creation of new states at energies $\pm E_A$. Additionally, the energies of new-created Andreev states, in the limit of $\Gamma_N = 0$ are $E_A \sim \sqrt{(\varepsilon_d + U/2)^2 + (\Gamma_S/2)^2}$. In the limit of $\Gamma_N = 0$ the border between the singlet and the doublet configuration is well specified by (3.24). From the cognitive point of view, we can ask what is the response of the system when the coupling to the superconducting lead drives the system from one to another configuration. In Fig. 3.13 we present two cases, the first when we observe the transition from the doublet to singlet configuration by increasing the coupling Γ_S (upper panel) and the second situation when change of the value of Γ_S induces a conversion in the opposite direction (lower panel). Starting from the initial conditions, at $t > 0$, the quantum dot is coupled to both reservoirs and its energy level is detuned to the half-filled occupation $\varepsilon_d = -U/2$, where the upper panel shows strong coupling to superconducting lead with $\Gamma_S > U$ and lower panel a weak coupling case $\Gamma_S < U$. Until the time $t = 5/2\Gamma_N$, both panels show the transient effects and formation of the doublet/singlet state on the quantum dot. When the system reaches equilibrium, the quantum oscillations of G_N will no longer occur. We abruptly reverse these couplings Γ_S at $t = 5/2\Gamma_N$. This shift of Γ_S value caused transitions from the doublet-to-singlet (panel a) and from the singlet-to-doublet (panel b), respectively. Regardless of the type of transition, we observe the quantum oscillations with period $T = 2\pi/E_A$, where $E_A \sim \sqrt{(\varepsilon_d + U/2)^2 + (\Gamma_S/2)^2}$ are Andreev bound states in the limit of $\Gamma_N = 0$. Moreover, the post-quench evolution is not completely identical to the transients of G_N. Differences have origin in the slightly varied initial configurations of the system before the quench.

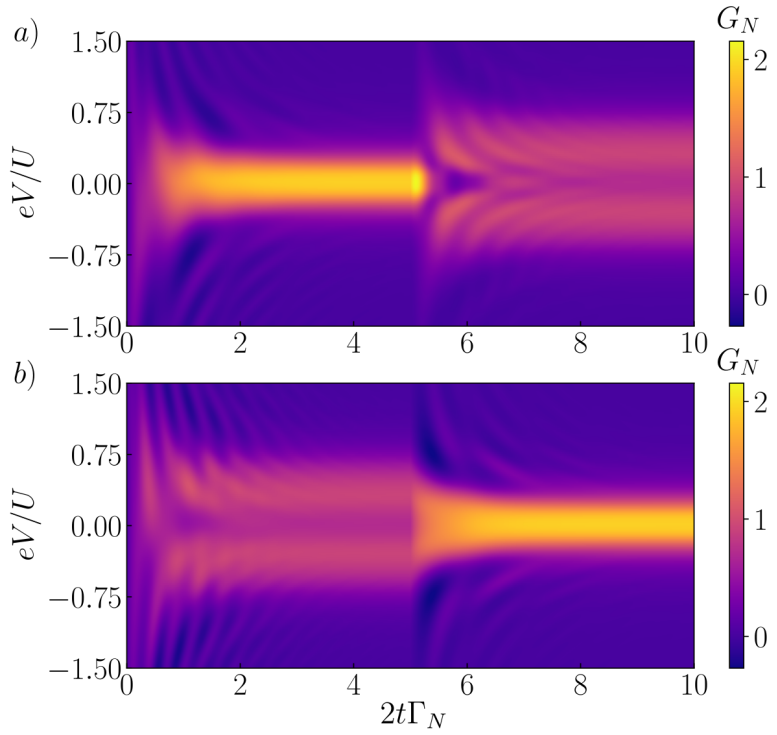

Figure 3.13: The evolution of the differential conductance G_N (in units of $2e^2/h$) with respect to voltage V and time t, obtained across the doublet-singlet transition due to the quench of Γ_S performed at $t = \frac{5}{2\Gamma_N}$. The upper panel presents transition from doublet to singlet: $\Gamma_S = 0.6 \to 1.4$. The lower panel present transition from singlet to doublet: $\Gamma_S = 1.4 \to 0.6$. The other model parameters: $\varepsilon_d = -U/2$, $\Gamma_N = 0.05$, $U = 1$ [110].

3.8 Summary

In this chapter, we have analysed the transient effects originating from linking the system components together. We have shown that the activation of quantum oscillations in transient charge currents strongly depends on the initial conditions. They are not observed if the quantum dot is initially occupied by a single electron. Otherwise, when the quantum dot is initially empty, the evolution to the steady state of the system exhibits quantum oscillations with the period $T = 2\pi/E_A$, where $E_A = \pm\sqrt{(\varepsilon_d + U/2)^2 + (\Gamma_S/2)^2}$

is energy of the Andreev bound states.

We noticed, that in the evolution of the system (uncorrelated quantum dot) after the sudden change of source-drain voltage the beats in the current $j_{N\sigma}(t)$ appear. The current $j_{N\sigma}(t)$ is a superposition of two contributing currents with the frequencies $\omega_{1/2} = \mu_N \pm \Gamma_S/2$, respectively.

For the uncorrelated quantum dot, the evolution after the shift of orbital level position exhibits the oscillatory structure of observables. The oscillations depend on the energy level of the quantum dot and the coupling to the superconducting lead $T = 2\pi/\sqrt{\Gamma_S^2 + 4(\Delta\varepsilon_d)^2}$. Investigating the system including the correlations, we have shown the π-shift in the oscillations upon crossing the half-filling level, which resembles the $0-\pi$ *transition* found for Josephson junctions in stationary conditions.

Finally, we also investigated the evolution of the system from its singlet configuration to doublet state and vice versa by changing the coupling strength Γ_S. This dynamic change of configuration activates the quantum oscillations with the period $T = 2\pi/E_A$ regardless of the direction of the transition, where $E_A = \pm\sqrt{(\varepsilon_d + U/2)^2 + (\Gamma_S/2)^2}$.

Independently of the initial state, the relaxation of the post-quench processes are governed by function $e^{-\Gamma_N t}$.

Chapter 4

Periodically driven quantum dot

In this chapter, we consider another dynamical scenario for N-QD-S heterostructure, where the quantum dot energy level is periodically varied by external fields. We investigate the influence of external fields on the Andreev bound states, the charge current averaged over a period of oscillations and the differential conductance. The periodically driven quantum systems constitute a broad field of physics, and we would like to explore the phenomena that appear in our N-QD-S nanojunction under such conditions. The suitable method to study systems described by periodic Hamiltonian $H(t) = H(t+T)$, with period $T = 2\pi/\omega$, is Floquet theory [126, 127]. We will present the basics of Floquet theory and its application to the considered quantum system. Results presented in this chapter were obtained by combining the Floquet theory with Green's function method.

4.1 Floquet theory

Let us start by presenting essential ingredients of the Floquet approach. For the time periodic Hamiltonian the solution of time-dependent Schrödinger equation

$$i\hbar\frac{d}{dt}|\psi(t)\rangle = \hat{H}(t)|\psi(t)\rangle \tag{4.1}$$

takes the special form called Floquet state $|\psi_n(t)\rangle$, where

$$|\psi_n(t)\rangle = |u_n(t)\rangle e^{-i\varepsilon_n t/\hbar} \tag{4.2}$$

is time-periodic mode $|u_n(t)\rangle = |u_n(t+T)\rangle$ (called *micromotion* of the system) and ε_n is the corresponding quasienergy. These Floquet states (4.2) are eigenstates of the time-evolution operator over one driving period

$$\hat{U}(t_0+T,t_0)|\psi_n(t_0)\rangle = e^{-i\varepsilon_n T/\hbar}|\psi_n(t_0)\rangle. \tag{4.3}$$

The eigenvalue $e^{-i\varepsilon_n T/\hbar}$ (the phase factor) is independent of t_0, at which the evolution over one time period starts. The time-dependent Floquet states $|\psi_n(t)\rangle$ can be computed by acting with the time-evolution operator on the Floquet state in specific time t_0: $|\psi_n(t)\rangle = U(t,t_0)|\psi_n(t_0)\rangle$. The time-evolution operator can be written in the form

$$\hat{U}(t_2,t_1) = \sum_n e^{-i\varepsilon_n(t_2-t_1)/\hbar}|u_n(t_2)\rangle\langle u_n(t_1)|, \tag{4.4}$$

because for every Floquet state one can choose a complete orthonormal basis at arbitrary time t. Then the evolution of a state $|\psi(t)\rangle$ can be expressed as

$$|\psi(t)\rangle = \sum_n c_n e^{-i\varepsilon_n(t-t_0)/\hbar}|u_n(t)\rangle, \tag{4.5}$$

where c_n denote the time-independent coefficients, $c_n = \langle u_n(t_0)|\psi(t_0)\rangle$.

The dynamics of the quantum system over times longer than the single driving period can be studied in a stroboscopic manner. In this approach the evolution is studied in the steps of the driving period T. This stroboscopic time evolution is simply expressed by

$$\hat{U}(t_0+T,t_0) \equiv e^{-iT\hat{H}^F_{t_0}/\hbar} \tag{4.6}$$

and depends of the Hamiltonian $\hat{H}^F_{t_0}$ represented in the Floquet space

$$\hat{H}^F_{t_0} = \sum_n \varepsilon_n |u_n(t_0)\rangle\langle u_n(t_0)|. \tag{4.7}$$

It is important to notice that the quasienergies ε_n and the Floquet modes $u_n(t)$ are not uniquely defined. The shift of quasienergy ε_n by energy $\hbar\omega$ does not affect the phase factor $e^{-i\varepsilon_n T/\hbar}$. Due to this fact, the quasienergy ε_n can be chosen arbitrarily and their shift by energy $\hbar\omega$ can be performed multiple times, then the quasienergy can be marked by additional index

$$\varepsilon_{nm} = \varepsilon_n + m\hbar\omega. \tag{4.8}$$

Next, the corresponding Floquet mode takes a form $|u_{nm}(t)\rangle = e^{im\omega t}|u_n(t)\rangle$. At this step, the solution of Schrödinger equation has a general form

$$|\psi_n(t)\rangle = e^{-i\varepsilon_n t/\hbar}|u_n(t)\rangle = e^{-i\varepsilon_{nm} t/\hbar}|u_{nm}(t)\rangle. \tag{4.9}$$

Substituting (4.9) into the time dependent Schrödinger equation (4.1) we obtain

$$\left(\hat{H}(t) - i\hbar\frac{d}{dt}\right)|u_{nm}(t)\rangle = \varepsilon_{nm}|u_{nm}(t)\rangle, \tag{4.10}$$

in an extended Hilbert space $\mathcal{F} = \mathcal{H} \otimes \mathcal{L}_T$. The Floquet space $\mathcal{F}$ is a product of the spatial space $\mathcal{H}$ for quantum systems and the space $\mathcal{L}_T$ of square-integrable functions that are periodic in time. In the extended space $\mathcal{F}$, the scalar product of states can be averaged over a time period as

$$\langle\langle u|v\rangle\rangle = \frac{1}{T}\int_0^T dt\langle u(t)|v(t)\rangle, \tag{4.11}$$

where double braket notation is used for elements of $\mathcal{F}$, corresponding to state at time t and its spatial coordinates in $\mathcal{H}$. The left side of (4.10) is called a quasienergy operator $\hat{Q}(t) = \hat{H}(t) - i\hbar\frac{d}{dt}$. To distinguish the quasienergy operator in the Floquet space $\mathcal{F}$ and Hilbert space $\mathcal{H}$, let us denote the quasienergy operator by $\bar{Q}$ if it acts on $\mathcal{F}$. Then, the quasienergy equation can be written as $\bar{Q}|u_{nm}\rangle\rangle = \varepsilon_{nm}|u_{nm}\rangle\rangle$ in $\mathcal{F}$ space.

In the Floquet space $\mathcal{F}$ the set of orthonormal basis states $|\alpha m\rangle\rangle$ can be constructed as a combination of the orthonormal basis states $|\alpha\rangle$ of $\mathcal{H}$ and the set of time-periodic functions $e^{im\omega t}$ as $|\alpha m(t)\rangle\rangle = |\alpha\rangle e^{im\omega t}$. In this basis

the quasienergy operator $\bar{Q}$ takes block structure

$$\begin{aligned}\langle\langle \alpha' m' | \bar{Q} | \alpha m \rangle\rangle &= \frac{1}{T}\int_0^T dt e^{-im'\omega t}\langle \alpha' | \hat{H}(t) - i\hbar\frac{d}{dt}|\alpha\rangle e^{im\omega t} \\ &= \langle \alpha' | \hat{H}_{m'-m} | \alpha \rangle + \delta_{m'm}\delta_{\alpha'\alpha} m\hbar\omega \end{aligned} \tag{4.12}$$

where $\hat{H}_m = \frac{1}{T}\int_0^T dt e^{-im\omega t}\hat{H}(t) = \hat{H}^\dagger_{-m}$ is the Fourier transform of $\hat{H}(t)$. This block structure of $\bar{Q}$ is also dubbed *Floquet matrix Hamiltonian* H^F_{nm} which has the following form

$$\begin{aligned} H^F_{nm} &= \frac{1}{T}\int_0^T dt e^{in\omega t}\bar{Q}(t)e^{-im\omega t} \\ &= \hat{H}_{n-m} - m\hbar\omega\delta_{nm}\mathbb{1}. \end{aligned} \tag{4.13}$$

It acquires the block structure

$$H^F = \left[\begin{array}{c|c|c|c|c} \ddots & \vdots & \vdots & \vdots & \iddots \\ \hline \cdots & \hat{H}_0 + 1\hbar\omega & \hat{H}_{-1} & \hat{H}_{-2} & \cdots \\ \hline \cdots & \hat{H}_1 & \hat{H}_0 & \hat{H}_{-1} & \cdots \\ \hline \cdots & \hat{H}_2 & \hat{H}_1 & \hat{H}_0 - 1\hbar\omega & \cdots \\ \hline \iddots & \vdots & \vdots & \vdots & \ddots \end{array}\right], \tag{4.14}$$

where the diagonal elements are shifted by $\hbar\omega$ which are related with absorption or emission of "*energy quanta*" from the environment.

4.2 Solution for time-periodic Hamiltonian

The Green's function formalism (Sec. A.3) and Floquet theory (Sec. 4.1) can be combined and used to describe the quantum system driven by periodic external fields. For example, the single quantum dot Hamiltonian presented in (3.1) can be simply converted to the time-dependent form

$$\hat{H} = \hat{H}_{QD}(t) + \hat{H}_N + \hat{H}_{N-QD} + \hat{H}_S + \hat{H}_{S-QD}, \tag{4.15}$$

with an oscillating quantum dot energy level $\hat{H}_{QD}(t) = \sum_\sigma \varepsilon_d(t)\hat{d}^\dagger_\sigma\hat{d}_\sigma$, where $\varepsilon_d(t) = \varepsilon^0_d + A\cos(\omega t)$ and ε^0_d is a stationary quantum dot energy level.

For the proximitized quantum dot it is convenient to introduce the matrix Green's function $\mathbf{G}^c_{QD}(t,t')$ (Nambu representation)

$$\mathbf{G}^c_{QD}(t,t') = \begin{pmatrix} -i\langle \hat{T}_C\{\hat{d}_\uparrow(t);\hat{d}^\dagger_\uparrow(t')\}\rangle & -i\langle \hat{T}_C\{\hat{d}_\uparrow(t);\hat{d}_\downarrow(t')\}\rangle \\ -i\langle \hat{T}_C\{\hat{d}^\dagger_\downarrow(t);\hat{d}^\dagger_\uparrow(t')\}\rangle & -i\langle \hat{T}_C\{\hat{d}^\dagger_\downarrow(t);\hat{d}_\downarrow(t')\}\rangle \end{pmatrix}. \tag{4.16}$$

whose elements come from the general definition for the contour ordered Green's function

$$G^c_{A,B}(t,t') = -i\langle \hat{T}_C\{A(t);B(t')\}\rangle. \tag{4.17}$$

From the equation of motion for Green's function $G^c_{d_\sigma,d^\dagger_{\sigma'}}(t,t')$ we obtain

$$\begin{aligned} &i\partial_t G^c_{d_\sigma,d^\dagger_{\sigma'}}(t,t') = \delta_c(t-t')\delta_{\sigma\sigma'} - i\langle \hat{T}_C\{i\partial_t \hat{d}_\sigma(t);\hat{d}^\dagger_{\sigma'}(t')\}\rangle = \\ &\delta_c(t-t')\delta_{\sigma\sigma'} + \varepsilon_d(t)G^c_{d_\sigma,d^\dagger_{\sigma'}}(t,t') + \sum_q V_q G^c_{c_{Sq\sigma},d^\dagger_{\sigma'}}(t,t') \\ &+ \sum_k V_k G^c_{c_{Nk\sigma},d^\dagger_{\sigma'}}(t,t'), \end{aligned} \tag{4.18}$$

where the mixed Green's functions

$$G^c_{c_{Sq\sigma},d^\dagger_{\sigma'}}(t,t') = -i\langle \hat{T}_C\{\hat{c}_{Sq\sigma}(t);\hat{d}^\dagger_{\sigma'}(t')\}\rangle, \tag{4.19}$$

$$G^c_{c_{Nk\sigma},d^\dagger_{\sigma'}}(t,t') = -i\langle \hat{T}_C\{\hat{c}_{Nk\sigma,}(t);\hat{d}^\dagger_{\sigma'}(t')\}\rangle, \tag{4.20}$$

describe the particle propagation between the superconducting/normal electrode and the quantum dot, respectively. For uncorrelated quantum dot the equation (4.18) simplifies to

$$\begin{aligned} (i\partial_t - \varepsilon_d(t))G^c_{d_\sigma,d^\dagger_{\sigma'}}(t,t') = \delta_c(t-t')\delta_{\sigma\sigma'} + \sum_q V_q G^c_{c_{Sq\sigma},d^\dagger_{\sigma'}}(t,t') \\ + \sum_k V_k G^c_{c_{Nk\sigma},d^\dagger_{\sigma'}}(t,t'). \end{aligned} \tag{4.21}$$

The contour-ordered Green's function can be rewritten as

$$\begin{aligned} G^c_{d_\sigma,d^\dagger_{\sigma'}}(t,t') = \delta_{\sigma\sigma'} g^c_{d_\sigma,d^\dagger_{\sigma'}}(t,t') + \sum_q V_q \int_C d\tau\, g^c_{d_\sigma,d^\dagger_{\sigma'}}(t,\tau)G^c_{c_{Sq\sigma},d^\dagger_{\sigma'}}(\tau,t') \\ + \sum_k V_k \int_C d\tau\, g^c_{d_\sigma,d^\dagger_{\sigma'}}(t,\tau)G^c_{c_{Nk\sigma},d^\dagger_{\sigma'}}(\tau,t'), \end{aligned} \tag{4.22}$$

where $g^c_{d_\sigma, d^\dagger_{\sigma'}}(t,t')$ is bare Green's function of isolated quantum dot. Determination of the mixed Green's function is discussed in Appendix A.8. At this step, let us consider the particle propagator $G^c_{d_\uparrow, d^\dagger_\uparrow}(t,t')$. To solve (4.22) we need the following functions

$$G^c_{c_{Nk\uparrow}, d^\dagger_\uparrow}(t,t') = V_k \int_C d\tau\, g^c_{c_{Nk\uparrow}, c^\dagger_{Nk\uparrow}}(t,\tau) G^c_{d_\uparrow, d^\dagger_\uparrow}(\tau,t'), \tag{4.23}$$

$$\begin{aligned} G^c_{c_{Sq\uparrow}, d^\dagger_\uparrow}(t,t') = -V_q \int_C d\tau\, g^c_{c^\dagger_{S-q\uparrow}, c^\dagger_{Sq\downarrow}}(t,\tau) G^c_{d^\dagger_\downarrow, d^\dagger_\uparrow}(\tau,t') \\ + \int_C d\tau\, g^c_{c_{Sq\uparrow}, c^\dagger_{Sq\downarrow}}(t,\tau) V_q G^c_{d_\uparrow, d^\dagger_\uparrow}(\tau,t'). \end{aligned} \tag{4.24}$$

Substituting (4.23) and (4.24) into (4.22), we obtain

$$\begin{aligned} G^c_{d_\uparrow, d^\dagger_\uparrow}(t,t') = g^c_{d_\uparrow, d^\dagger_\uparrow}(t,t') \\ + \int_C d\tau \int_C d\tau' g^c_{d_\uparrow, d^\dagger_\uparrow}(t,\tau) \Sigma^c_{c_{N\uparrow}, c^\dagger_{N\uparrow}}(\tau,\tau') G^c_{d_\uparrow, d^\dagger_\uparrow}(\tau',t') \\ + \int_C d\tau \int_C d\tau' g^c_{d_\uparrow, d^\dagger_\uparrow}(t,\tau) \Sigma^c_{c^\dagger_{S\uparrow}, c^\dagger_{S\downarrow}}(\tau,\tau') G^c_{d^\dagger_\downarrow, d^\dagger_\uparrow}(\tau',t') \\ + \int_C d\tau \int_C d\tau g^c_{d_\uparrow, d^\dagger_\uparrow}(t,\tau) \Sigma^c_{c_{S\uparrow}, c^\dagger_{S\uparrow}}(\tau,\tau') G^c_{d_\uparrow, d^\dagger_\uparrow}(\tau',t') \end{aligned} \tag{4.25}$$

where the contour-ordered self-energies are defined as

$$\Sigma^c_{c_{N\uparrow}, c^\dagger_{N\uparrow}}(\tau,\tau') = \sum_k V_k^2 g^c_{c_{Nk\uparrow}, c^\dagger_{Nk\uparrow}}(\tau,\tau'), \tag{4.26}$$

$$\Sigma^c_{c^\dagger_{S\uparrow}, c^\dagger_{S\downarrow}}(\tau,\tau') = \sum_q V_q^2 g^c_{c^\dagger_{S-q\uparrow}, c^\dagger_{Sq\downarrow}}(\tau,\tau'), \tag{4.27}$$

$$\Sigma^c_{c_{S\uparrow}, c^\dagger_{S\uparrow}}(\tau,\tau') = \sum_q V_q^2 g^c_{c_{Sq\uparrow}, c^\dagger_{Sq\uparrow}}(\tau,\tau'). \tag{4.28}$$

In the same manner, we can obtain the other element of the Green's function (4.16) in the Nambu representation

$$\begin{aligned} G^c_{d^\dagger_\downarrow, d^\dagger_\uparrow}(t,t') = \int_C d\tau \int_C d\tau' g^c_{d^\dagger_\downarrow, d_\downarrow}(t,\tau) \Sigma^c_{c^\dagger_{N\uparrow}, c_{N\uparrow}}(\tau,\tau') G^c_{d^\dagger_\downarrow, d^\dagger_\uparrow}(\tau',t') \\ + \int_C d\tau \int_C d\tau' g^c_{d^\dagger_\downarrow, d_\downarrow}(t,\tau) \Sigma^c_{c^\dagger_{S\uparrow}, c^\dagger_{S\downarrow}}(\tau,\tau') G^c_{d^\dagger_\downarrow, d^\dagger_\uparrow}(\tau',t') \\ + \int_C d\tau \int_C d\tau' g^c_{d^\dagger_\downarrow, d_\downarrow}(t,\tau) \Sigma^c_{c^\dagger_{S\downarrow}, c_{S\downarrow}}(\tau,\tau') G^c_{d_\uparrow, d^\dagger_\uparrow}(\tau',t'). \end{aligned} \tag{4.29}$$

The solution for diagonal elements of (4.16) is sufficient to find other related functions. According to the Langreth's theorem (A.57), the contour-ordered casual functions can be expressed in the terms of *retarded* and *advanced* ones

$$\begin{aligned} G^{r,a}_{d_\uparrow,d^\dagger_\uparrow}(t,t') &= g^{r,a}_{d_\uparrow,d^\dagger_\uparrow}(t,t') \\ &+ \int_{-\infty}^{\infty} d\tau \int_{-\infty}^{\infty} d\tau' g^{r,a}_{d_\uparrow,d^\dagger_\uparrow}(t,\tau)\Sigma^{r,a}_{c_{N\uparrow},c^\dagger_{N\uparrow}}(\tau,\tau')G^{r,a}_{d_\uparrow,d^\dagger_\uparrow}(\tau',t') \\ &+ \int_{-\infty}^{\infty} d\tau \int_{-\infty}^{\infty} d\tau' g^{r,a}_{d_\uparrow,d^\dagger_\uparrow}(t,\tau)\Sigma^{r,a}_{c^\dagger_{S\uparrow},c^\dagger_{S\downarrow}}(\tau,\tau')G^{r,a}_{d^\dagger_\downarrow,d^\dagger_\uparrow}(\tau',t') \\ &+ \int_{-\infty}^{\infty} d\tau \int_{-\infty}^{\infty} d\tau' g^{r,a}_{d_\uparrow,d^\dagger_\uparrow}(t,\tau)\Sigma^{r,a}_{c_{S\uparrow},c^\dagger_{S\uparrow}}(\tau,\tau')G^{r,a}_{d_\uparrow,d^\dagger_\uparrow}(\tau',t'), \end{aligned} \tag{4.30}$$

$$\begin{aligned} G^{r,a}_{d^\dagger_\downarrow,d^\dagger_\uparrow}(t,t') &= \int_{-\infty}^{\infty} d\tau \int_{-\infty}^{\infty} d\tau' g^{r,a}_{d^\dagger_\downarrow,d_\downarrow}(t,\tau)\Sigma^{r,a}_{c^\dagger_{N\uparrow},c_{N\uparrow}}(\tau,\tau')G^{r,a}_{d^\dagger_\downarrow,d^\dagger_\uparrow}(\tau',t') \\ &+ \int_{-\infty}^{\infty} d\tau \int_{-\infty}^{\infty} d\tau' g^{r,a}_{d^\dagger_\downarrow,d_\downarrow}(t,\tau)\Sigma^{r,a}_{c^\dagger_{S\uparrow},c^\dagger_{S\downarrow}}(\tau,\tau')G^{r,a}_{d^\dagger_\downarrow,d^\dagger_\uparrow}(\tau',t') \\ &+ \int_{-\infty}^{\infty} d\tau \int_{-\infty}^{\infty} d\tau' g^{r,a}_{d^\dagger_\downarrow,d_\downarrow}(t,\tau)\Sigma^{r,a}_{c^\dagger_{S\downarrow},c_{S\downarrow}}(\tau,\tau')G^{r,a}_{d_\uparrow,d^\dagger_\uparrow}(\tau',t'). \end{aligned} \tag{4.31}$$

At this step, we can perform the Fourier transform of the Green's function

$$f_{nm}(\varepsilon) = \int_{-\infty}^{\infty} dt' \frac{1}{T} \int_0^T dt e^{i(\varepsilon+n\omega)t - i(\varepsilon+m\omega)t'} f(t,t'), \tag{4.32}$$

where the contour integral of the functions $C(t,t') = \int_C d\tau A(t,\tau)B(\tau,t')$ is equal to $C_{nm}(\varepsilon) = \sum_k A_{nk}(\varepsilon)B_{km}(\varepsilon)$ in Fourier space (the proof of this property is included in Appendix A.5). Finally, we obtain the Green's functions expressed by the Fourier coefficients

$$\begin{aligned} G^{r,a}_{d_\uparrow,d^\dagger_\uparrow;nm}(\varepsilon) &= g^{r,a}_{d_\uparrow,d^\dagger_\uparrow;nm}(\varepsilon) + \sum_{k,l} g^{r,a}_{d_\uparrow,d^\dagger_\uparrow;nk}(\varepsilon)\Sigma^{r,a}_{c_{N\uparrow},c^\dagger_{N\uparrow};kl}(\varepsilon)G^{r,a}_{d_\uparrow,d^\dagger_\uparrow;lm}(\varepsilon) \\ &+ \sum_{k,l} g^{r,a}_{d_\uparrow,d^\dagger_\uparrow;nk}(\varepsilon)\Sigma^{r,a}_{c^\dagger_{S\uparrow},c^\dagger_{S\downarrow};kl}(\varepsilon)G^{r,a}_{d^\dagger_\downarrow,d^\dagger_\uparrow;lm}(\varepsilon) \\ &+ \sum_{k,l} g^{r,a}_{d_\uparrow,d^\dagger_\uparrow;nk}(\varepsilon)\Sigma^{r,a}_{c_{S\uparrow},c^\dagger_{S\uparrow};kl}(\varepsilon)G^{r,a}_{d_\uparrow,d^\dagger_\uparrow;lm}(\varepsilon), \end{aligned} \tag{4.33}$$

$$\begin{aligned} G^{r,a}_{d^\dagger_\downarrow,d^\dagger_\uparrow;nm}(\varepsilon) &= \sum_{k,l} g^{r,a}_{d^\dagger_\downarrow,d_\downarrow;nk}(\varepsilon)\Sigma^{r,a}_{c^\dagger_{N\uparrow},c_{N\uparrow};kl}(\varepsilon)G^{r,a}_{d^\dagger_\downarrow,d^\dagger_\uparrow;lm}(\varepsilon) \\ &+ \sum_{k,l} g^{r,a}_{d^\dagger_\downarrow,d_\downarrow;nk}(\varepsilon)\Sigma^{r,a}_{c^\dagger_{S\uparrow},c^\dagger_{S\downarrow};kl}(\varepsilon)G^{r,a}_{d^\dagger_\downarrow,d^\dagger_\uparrow;lm}(\varepsilon) \\ &+ \sum_{k,l} g^{r,a}_{d^\dagger_\downarrow,d_\downarrow;nk}(\varepsilon)\Sigma^{r,a}_{c^\dagger_{S\downarrow},c_{S\downarrow};kl}(\varepsilon)G^{r,a}_{d_\uparrow,d^\dagger_\uparrow;lm}(\varepsilon). \end{aligned} \tag{4.34}$$

At this step, we can recast (4.33) and (4.34) into the Dyson equation in matrix form

$$\mathbf{G}^{r,a}_{QD,nm}(\varepsilon) = \mathbf{g}^{r,a}_{QD,nm}(\varepsilon) + \sum_{k,l} \mathbf{g}^{r,a}_{QD,nk}(\varepsilon)\mathbf{\Sigma}^{r,a}_{kl}(\varepsilon)\mathbf{G}^{r,a}_{QD,lm}(\varepsilon), \tag{4.35}$$

where $\mathbf{\Sigma}^{r,a}_{nm}(\varepsilon) = \mathbf{\Sigma}^{r,a}_{N,nm}(\varepsilon) + \mathbf{\Sigma}^{r,a}_{S,nm}(\varepsilon)$ is the total self-energy of the system. The individual self-energies (4.39) are defined as follows

$$\mathbf{\Sigma}^{r,a}_{N,nm}(\varepsilon) = \mp \begin{bmatrix} \frac{i\Gamma_N}{2} & 0 \\ 0 & \frac{i\Gamma_N}{2} \end{bmatrix} \delta_{nm}, \tag{4.36}$$

$$\mathbf{\Sigma}^{r,a}_{S,nm}(\varepsilon) = -\frac{\alpha(\tilde{\varepsilon})\Gamma_S/2}{\sqrt{|(\tilde{\varepsilon} \pm i0^+)^2 + \Delta^2_{sc}|}} \begin{bmatrix} \tilde{\varepsilon} & -\Delta_{sc} \\ -\Delta_{sc} & \tilde{\varepsilon} \end{bmatrix} \delta_{nm}, \tag{4.37}$$

where $\alpha(\tilde{\varepsilon}) = \Theta(\Delta_{sc} - |\tilde{\varepsilon}|) \pm i\,\mathrm{sgn}(\tilde{\varepsilon})\Theta(|\tilde{\varepsilon}| - \Delta_{sc})$ and $\tilde{\varepsilon} = \varepsilon + n\omega$. More specific calculations are presented in Appendix A.9.

According to Ref. [128], the Dyson equation (4.35) can be solved when the self-energies of the system are diagonal in Floquet space. Then the solution of the matrix equation (4.35) becomes

$$[\mathbf{G}^{r,a}_{QD}(\varepsilon)] = \left[\mathbf{I} - \mathbf{g}^{r,a}_{QD}(\varepsilon)\mathbf{\Sigma}^{r,a}(\varepsilon)\right]^{-1} [\mathbf{g}^{r,a}_{QD}(\varepsilon)], \tag{4.38}$$

which can be explicitly shown as

$$[\mathbf{G}^{r,a}_{QD}(\varepsilon)] = \begin{pmatrix} \ddots & \vdots & \vdots & \vdots & \iddots \\ \cdots & \gamma_{-1,-1} & \gamma_{-1,0} & \gamma_{-1,1} & \cdots \\ \cdots & \gamma_{0,-1} & \gamma_{0,0} & \gamma_{0,1} & \cdots \\ \cdots & \gamma_{1,-1} & \gamma_{1,0} & \gamma_{1,1} & \cdots \\ \iddots & \vdots & \vdots & \vdots & \ddots \end{pmatrix}^{-1} [\mathbf{g}^{r,a}_{QD}(\varepsilon)], \tag{4.39}$$

where $\gamma_{nm} = \delta_{nm}\mathbf{I} - \mathbf{g}^{r,a}_{QD,nm}\mathbf{\Sigma}^{r,a}_{mm}$ and $\mathbf{I}$ denotes the identity matrix.

The bare Green's function $\mathbf{g}^{r,a}_{QD,nm}$ of isolated quantum dot can be diagonalized with respect to the Floquet coordinates n, m by appropriate unitary matrix $\mathbf{\Lambda}_{nl}$ [129]

$$\sum_{nm} \mathbf{\Lambda}_{ln}(\mathbf{g}^{r,a}_{QD})^{-1}_{nm}\mathbf{\Lambda}_{ml} = (\mathbf{D}^{r,a}_{QD})^{-1}_{ll}. \tag{4.40}$$

In this basis, the diagonal retarded and advanced Green's functions are expressed by

$$(\mathbf{D}^{r,a}_{QD})^{-1}_{ll} = (\varepsilon + l\omega \pm i0^{+})\mathbf{I} - \varepsilon^{0}_{d}\sigma_{z}, \tag{4.41}$$

where σ_z is the Pauli matrix. Making back projection, the isolated bare Green's function can be written as follows

$$\mathbf{g}^{r,a}_{QD,nm}(\varepsilon) = \sum_{l} \mathbf{\Lambda}^{\dagger}_{nl}\mathbf{D}^{r,a}_{QD,ll}(\varepsilon)\mathbf{\Lambda}_{lm}. \tag{4.42}$$

Since we consider oscillating energy level $\varepsilon_d(t)$, the matrix operator $\mathbf{\Lambda}_{nl}$ is expressed by the Bessel functions of a first kind (see Eqs. (A.82)-(A.95))

$$\mathbf{\Lambda}_{nm} = \begin{bmatrix} J_{n-m}\left(\frac{A}{\omega}\right) & 0 \\ 0 & J_{n-m}\left(\frac{-A}{\omega}\right) \end{bmatrix}. \tag{4.43}$$

Then the matrix representation of the bare Green's function ((A.96)-(A.97)) simplifies to [66]

$$\mathbf{g}^{r,a}_{QD,nm}(\varepsilon) = \sum_{l} \begin{bmatrix} \frac{J_{n-l}(A/\omega)J_{m-l}(A/\omega)}{\varepsilon \pm i0^{+} + l\omega - \varepsilon^{0}_{d}} & 0 \\ 0 & \frac{J_{n-l}(-A/\omega)J_{m-l}(-A/\omega)}{\varepsilon \pm i0^{+} + l\omega + \varepsilon^{0}_{d}} \end{bmatrix}. \tag{4.44}$$

In the case of time-periodic driving of the system, the effective quantum dot spectrum is determined by

$$\langle \rho_d(\varepsilon) \rangle = -\frac{1}{\pi} \operatorname{Im}\left[\mathbf{G}^{r}_{QD,00}(\varepsilon + i0^{+})\right]_{11}, \tag{4.45}$$

which is equivalent to averaging over a single period T [128]. In general, this spectral representation function must be positive [130].

To calculate time-dependent charge current we use general formula introduced in (3.11) for particle transport into the metallic lead [65, 131, 132]. The charge current equation can be written in the form

$$j_{N\sigma}(t) = \frac{2e}{\hbar} \sum_{k} V_k \operatorname{Re}\left[i\langle \hat{c}_{k\sigma}(t); \hat{d}^{\dagger}_{\sigma}(t) \rangle\right] = \frac{2e}{\hbar} \sum_{k} V_k \operatorname{Re}\left[G^{<}_{c_{k\sigma}, d^{\dagger}_{\sigma}}(t,t)\right], \tag{4.46}$$

where the *lesser* Green's function can be expressed as a convolution of Green's function for quantum dot and bare Green's function

$$G^{<}_{c_{k\sigma},d^{\dagger}_{\sigma}}(t,t') = V_k \int_C d\tau \left[G^{r}_{d_\sigma,d^{\dagger}_{\sigma}}(t,\tau) g^{<}_{c_{Nk\sigma},c^{\dagger}_{Nk\sigma}}(\tau,t') + G^{<}_{d_\sigma,d^{\dagger}_{\sigma}}(t,\tau) g^{a}_{c_{Nk\sigma},c^{\dagger}_{Nk\sigma}}(\tau,t') \right]. \tag{4.47}$$

Substituting the *lesser* Green's function to (4.46) we obtain the Landauer's formula

$$j_{N\sigma}(t) = \frac{2e}{\hbar} \int_C d\tau \,\mathrm{Re}\left[G^{r}_{d_\sigma,d^{\dagger}_{\sigma}}(t,\tau) \Sigma^{<}_{c_{N\sigma},c^{\dagger}_{N\sigma}}(\tau,t) + G^{<}_{d_\sigma,d^{\dagger}_{\sigma}}(t,\tau) \Sigma^{a}_{c_{N\sigma},c^{\dagger}_{N\sigma}}(\tau,t) \right]. \tag{4.48}$$

Using the Nambu representation, the Andreev current (flowing through the normal lead) can be expressed in the matrix form

$$j_{N\uparrow}(t) = \frac{e}{\hbar} \int_C d\tau \,\mathrm{Re}\left[\mathbf{G}^{r}_{QD}(t,\tau) \mathbf{\Sigma}^{<}_{N}(\tau,t) + \mathbf{G}^{<}_{QD}(t,\tau) \mathbf{\Sigma}^{a}_{N}(\tau,t) \right]_{11-22}, \tag{4.49}$$

where the diagonal elements 11 and 22 correspond to the particle and hole terms, respectively. Transforming (4.46) into Fourier space, it is possible to express the time-dependent current in Floquet space

$$\begin{aligned} j_{N\uparrow}(t) = \frac{e}{\hbar} \sum_{n,m,p} \int_{-\omega/2}^{\omega/2} \frac{d\varepsilon}{2\pi} \mathrm{Re}\{ e^{-i(n-p)\omega t} [& \mathbf{G}^{r}_{QD,nm}(\varepsilon) \mathbf{\Sigma}^{<}_{N,mp}(\varepsilon) \\ & + \mathbf{G}^{<}_{QD,nm}(\varepsilon) \mathbf{\Sigma}^{a}_{N,mp}(\varepsilon)] \}_{11-22}. \end{aligned} \tag{4.50}$$

Assuming that the indices n, p are equal, we obtain the average current over single period T

$$\langle j_{N\uparrow} \rangle = \frac{e}{\hbar} \sum_{n,m} \int_{-\omega/2}^{\omega/2} \frac{d\varepsilon}{2\pi} \mathrm{Re}\{ [\mathbf{G}^{r}_{QD,nm}(\varepsilon) \mathbf{\Sigma}^{<}_{N,mn}(\varepsilon) + \mathbf{G}^{<}_{QD,nm}(\varepsilon) \mathbf{\Sigma}^{a}_{N,mn}(\varepsilon)] \}_{11-22}. \tag{4.51}$$

Here, in (4.50) and (4.51) the *lesser* Green's function of a single quantum dot

in Nambu-Floquet space is equal to

$$\begin{aligned}\left[\mathbf{G}^{<}_{QD,nm}(\varepsilon)\right]_{\mu\nu} = \sum_{kl}\{&[\mathbf{G}^{r}_{QD,nk}]_{\mu 1}[\mathbf{\Sigma}^{<}_{kl}(\varepsilon)]_{11}[\mathbf{G}^{a}_{QD,lm}]_{1\nu} \\ &+ [\mathbf{G}^{r}_{QD,nk}]_{\mu 1}[\mathbf{\Sigma}^{<}_{kl}(\varepsilon)]_{12}[\mathbf{G}^{a}_{QD,lm}]_{2\nu} \\ &+ [\mathbf{G}^{r}_{QD,nk}]_{\mu 2}[\mathbf{\Sigma}^{<}_{kl}(\varepsilon)]_{21}[\mathbf{G}^{a}_{QD,lm}]_{1\nu} \\ &+ [\mathbf{G}^{r}_{QD,nk}]_{\mu 2}[\mathbf{\Sigma}^{<}_{kl}(\varepsilon)]_{22}[\mathbf{G}^{a}_{QD,lm}]_{2\nu}\}, \end{aligned} \tag{4.52}$$

where $\mathbf{\Sigma}^{<}(\varepsilon) = \mathbf{\Sigma}^{<}_{N}(\varepsilon)+\mathbf{\Sigma}^{<}_{S}(\varepsilon)$ is sum of the *lesser* self-energies of the reservoirs. The lesser self-energy for single electrode is the result of the subtraction of *advanced* and *retarded* functions

$$\mathbf{\Sigma}^{<}_{N,nm}(\varepsilon) = \left(\mathbf{\Sigma}^{a}_{N,nm}(\varepsilon) - \mathbf{\Sigma}^{r}_{N,nm}(\varepsilon)\right)\begin{pmatrix} f_N(\varepsilon+n\omega) & 0 \\ 0 & 1-f_N(-\varepsilon-n\omega)\end{pmatrix} \tag{4.53}$$

$$\mathbf{\Sigma}^{<}_{S,nm}(\varepsilon) = \left(\mathbf{\Sigma}^{a}_{S,nm}(\varepsilon) - \mathbf{\Sigma}^{r}_{S,nm}(\varepsilon)\right) f_S(\varepsilon+n\omega), \tag{4.54}$$

multiplied by the Fermi-Dirac distribution function

$$f_{N/S}(x) = 1/[e^{(x-\mu_{N/S})/k_BT}+1]. \tag{4.55}$$

4.3 Numerical results

The method applied in this chapter, based on the Green's function and Floquet approach, allows to calculate the time dependent observables and observables averaged over the single period. In this method the system is adiabatically switched on and the time-dependent functions describing the system become cyclic with the same period as the drive. All results in this chapter are obtained for the temperature limit $T \to 0$. As an example of the time-dependent currents we present Fig. 4.1. In this figure, we show the charge current $I_N(t) = j_{N\uparrow}(t)$ for different values of oscillation amplitudes in regime of the superconducting atomic limit $\Delta_{sc} \to \infty$. For the system described by Hamiltonian (4.15) with applied source-drain voltage $V = 1\omega$, we

observe oscillatory character of the plots in single period window of the drive. At this stage, we would like to highlight the complex nature of these charts. For a larger amplitude, a more wrinkled structure of the plot can be seen. The reason for this phenomenon is that there are more eigenenergies in a transport window. Localization and behaviour of those eigenenergies will be revealed in the further part of this chapter. For the specific time window, the time-dependent currents obey the symmetry relation $I_N(-V,t) = -I_N(V,t+T/2)$.

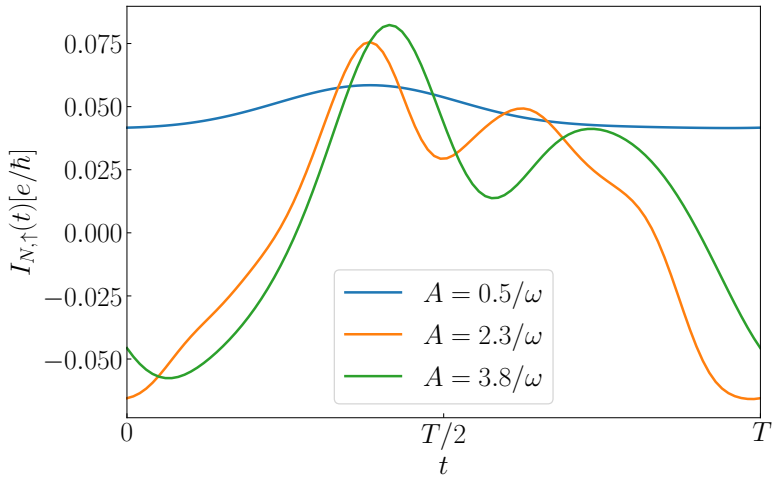

Figure 4.1: The time-dependent currents for the periodically driven $\varepsilon_d(t)$ obtained for: $V = 1\omega$, $\Gamma_N = 0.1\omega$, $\Gamma_S = 1\omega$, $U = 0$. The results were obtained from the numerical solution of (4.50).

One of the convenient ways to study the periodically driven system is to compute the observables averaged over a period. Using the Landauer formula in (4.51), we computed the time average current $\langle I_N \rangle$ and differential conductance $\langle G_N \rangle$ averaged over one driving period versus the source-drain voltage V applied across the junction, considering the in-gap states by assuming $\Delta_{sc} \to \infty$. In Fig. 4.2, we can notice that in the absence of source-drain voltage the current $\langle I_N \rangle$ is zero, because the incoming and outgoing charge flows cancel each other. For larger source-drain voltage V, we observe an

increasing value and plateau regions of $\langle I_N \rangle$. Using standard definition of the differential conductance $\langle G_N \rangle = \frac{d\langle I_N \rangle}{dV}$, we reveal the energy states appearing in the driven system. We notice that the conductance peaks perfectly coincide with the slope parts of charge current plots, which exhibit the positions of eigenenergies. The differential conductance $\langle G_N \rangle$ shows that the rapid growth of the averaged current occurs if the voltage V comes close to the eigenenergies of the system.

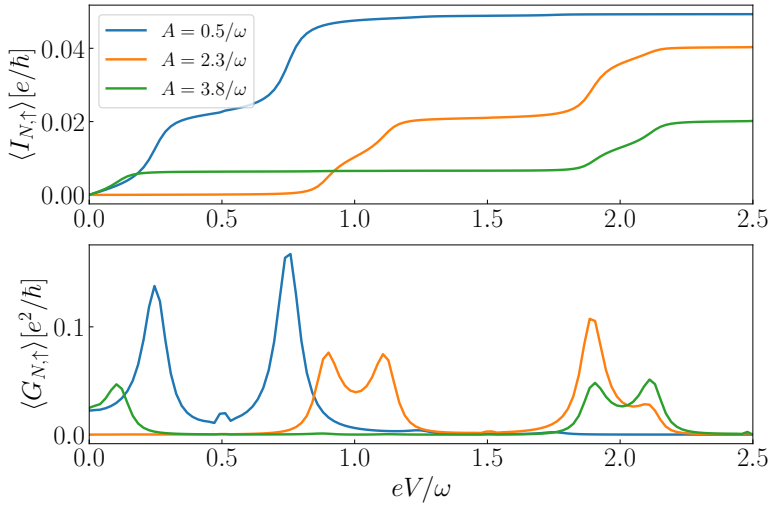

Figure 4.2: The averaged current $\langle I_N \rangle$ and differential conductance $\langle G_N \rangle$ with respect to voltage V obtained for the periodically driven $\varepsilon_d(t)$, using: $\Gamma_N = 0.1\omega$, $\Gamma_S = 1\omega$, $U = 0$.

To gain a broader view of the quasiparticle eigenenergies, let us present results for the spectral function $\langle \rho_d(\varepsilon) \rangle$ defined by (4.45). In the time-periodic system described by Hamiltonian $H(t) = H(t+T)$ the spectral function is equivalent to averaging over a period T. In Fig. 4.3 and Fig. 4.4 we present the spectral function for N-QD-N and N-QD-S heterostructure, respectively.

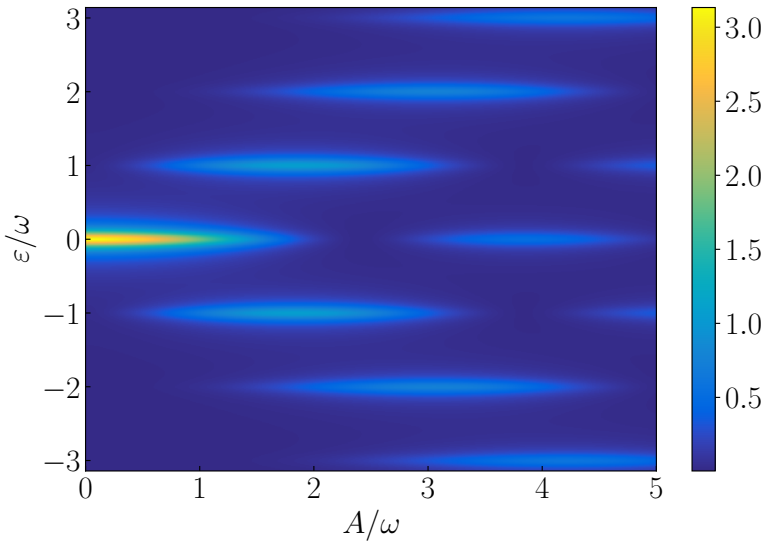

Figure 4.3: The averaged spectral function of QD versus the amplitude of driving field. Results are obtained using: $\Gamma_N = 0.1\omega$, $\Gamma_S = 0$, $U = 0$ assuming $\varepsilon_d(t) = A\cos(\omega t)$.

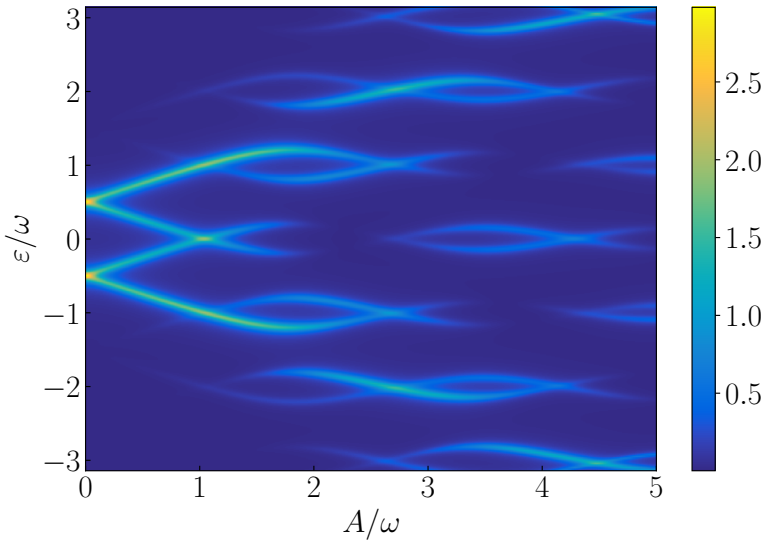

Figure 4.4: The same as in Fig. 4.3 but for the N-QD-S heterostructure, assuming $\Gamma_S = 1\omega$.

The results for the normal junction will be a reference point. The case of N-QD-N heterojunction in Fig. 4.3 shows the spectral function dependent on energy ε and driving amplitude A, which include a series of equidistant states at energies $\varepsilon_d^0 + n\omega$, where n is an integer number. Those states are called the photo-assisted tunnelling states (PAT), harmonic states or Floquet states for the driven system [65–67]. We observe the emergence and extinction of these states and their greater number with larger amplitude of the drive. The zero harmonic peak vanishes for ratio $A/\omega \simeq 2.405$ which corresponds to the zero value of Bessel function $J_0(A/\omega)$. We see the finite broadening of the peaks which comes from the coupling to the metallic reservoirs.

For N-QD-S heterostructure, such spectral function dependent on energy level ε and driving amplitude A is presented in Fig. 4.4. In contrast to the N-QD-N junction, in this particular case, we observe the splitting of the zero and higher-order harmonics. In the stationary case ($A = 0$), the quasiparticle peaks in the subgap spectrum coincide with two Andreev bound states at energies $\pm\sqrt{(\varepsilon_d^0)^2 + (\Gamma_S/2)^2}$ [61] broadened by Γ_N. For small amplitudes, the evolution of the quasiparticle energies shows that the branches of the zero-harmonic mode split. Simultaneously new higher-order harmonic states appear, shifted by energy $n\omega$. We observe that the zero-harmonic states linearly branch out and they are headed to the horizontal lines corresponding to energies $n\omega$. One pair of the zero-harmonic branch crosses each other around $A = 1.1\omega$ on the line corresponding to the zero energy. The second pair of the zero-harmonic state evolves to the horizontal lines for $n = 1$ and $n = -1$, where they interlace with the higher-order harmonics. For larger amplitudes, we observe overlapping and interlacing of the states between neighboring harmonics. Together with the larger amplitude the distance between mixed branches and their intensity slightly decrease.

Comparing the differential conductance $\langle G_N \rangle$ in Fig. 4.2 with the quasiparticle spectrum for corresponding amplitudes, we see that the additional states in charge transport perfectly coincide with the positions of the harmonic

states. The slightly smaller splitting of mixed branches along $n = 0$ comes together with the lesser expectation value of the on-dot pairing potential

$$\langle \hat{d}_{\downarrow} \hat{d}_{\uparrow} \rangle_T = - \int_{-\omega/2}^{\omega/2} \frac{d\varepsilon}{2\pi} [\mathbf{G}^r_{QD,00}(\varepsilon)]_{12} \tag{4.56}$$

averaged over a period T. Its dependence on the amplitude A is presented in Fig. 4.5. We observe that this induced order parameter is correlated with the amount of spectral weight of the zeroth-order harmonic. The proximity induced order parameter vanishes for such amplitude where the zero-level harmonic states lose their spectral weights.

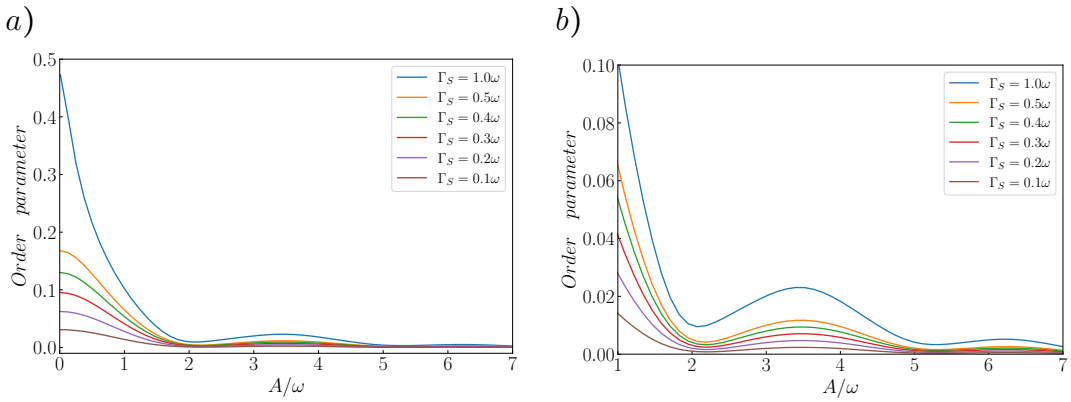

Figure 4.5: *a*) Expectation value of the proximity induced order parameter $\langle \hat{d}_{\downarrow} \hat{d}_{\uparrow} \rangle$ versus the amplitude A, obtained for several values of Γ_S, as indicated. Using: $\varepsilon_d^0 = 0$, $\Gamma_N/\omega = 0.1$. *b*) Zoom of the plot shown in panel *a*.

To investigate the influence of the driving frequency, in Fig. 4.6, we present the time-averaged density of states versus ω/Γ_S. The results are obtained for the amplitude $A = 2.2\Gamma_S$. This quasiparticle spectrum illustrates one pair of the Andreev quasiparticles (zero mode) with the higher-order harmonic states and their linear evolution along $n\omega$. The higher-order states are aligned along $\varepsilon_d^0 + n\omega$ lines and disappear for large ω. In the high frequency limit $\omega \to \infty$, the numerical results agree with the analytical solution of Magnus expansion for the proximitized system Hamiltonian (discussed in the Sec. 4.4).

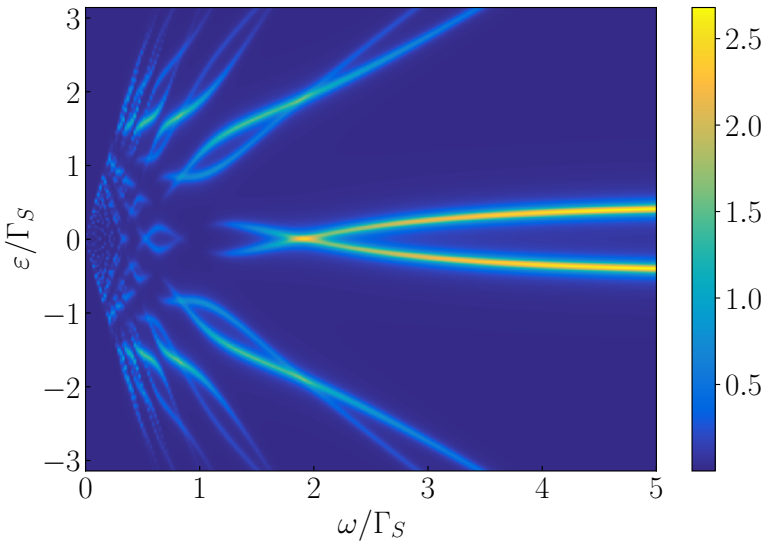

Figure 4.6: The quantum dot's spectral function of N-QD-S heterostructure versus the driving frequency ω. Results are obtained for A=2.2Γ_S, $\Gamma_N = 0.1\Gamma_S$, $U = 0$.

Influence of the pairing gap Δ_{sc}

To investigate a more realistic situation, we would like to focus on a case when the superconducting energy gap Δ_{sc} takes a finite value. Usually, the value of the energy gap is a few or fractions of meV. Fig. 4.7 presents the quasiparticle spectral function with respect to the amplitude A, obtained for $\Delta_{sc} = 0.5\omega$. In this plot, we observe that the quasiparticle function does not follow the main properties of the energy spectrum displayed in Fig. 4.4. We can notice that the higher-order harmonics ($|n| \neq 0$) are pushed out of the superconducting gap and their splitting is reduced in comparison to the results in the limit $\Delta_{sc} \to \infty$. This behaviour depends on the efficiency of the pairing which gradually decreases with increasing amplitude, due to the larger influence of the continuum of electron states above the superconductor energy gap. Raising the QD energy level above the superconducting energy gap causes a partial leakage of the spectral weight towards the in-gap regime. A feature of this phenomenon is a continuous background which appears in the spectral function, what is visible in Figs 4.7 and 4.8. This continuous

background corresponds to incoherent subgap states.

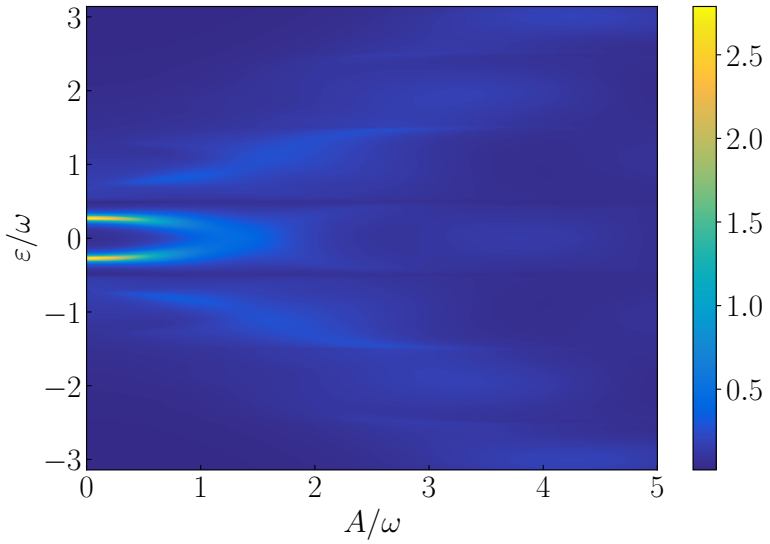

Figure 4.7: The quantum dot's spectral function of N-QD-S heterostructure with respect to the driving amplitude A. The results are obtained for $\Delta_{sc} = 0.5\omega$, $\Gamma_N = 0.1\omega$, $\Gamma_S = 1\omega$, $U = 0$.

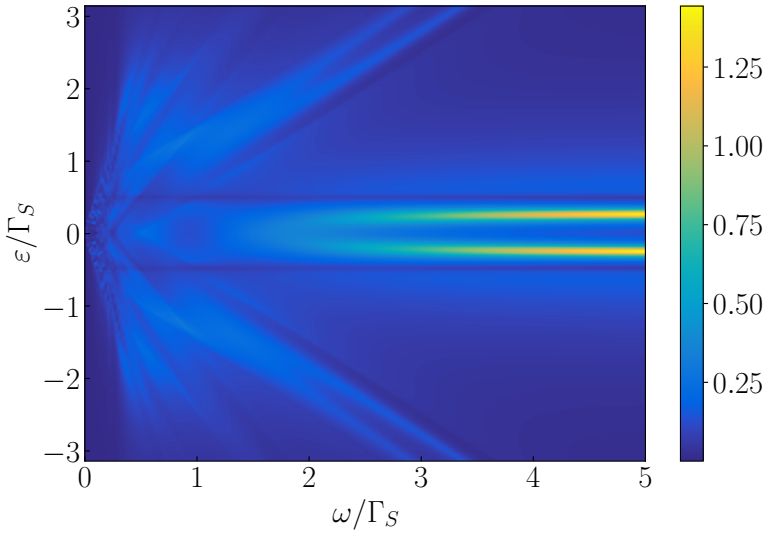

Figure 4.8: The quantum dot's spectral function of N-QD-S heterostructure with respect to the driving frequency ω, using: $\Delta_{sc} = 0.5\Gamma_S$, A=$2.2\Gamma_S$, $\Gamma_N = 0.1\Gamma_S$, $U = 0$.

To illustrate the influence of driving frequency in the case of the finite value of the superconducting energy gap, we present Fig. 4.8. This figure displays the distribution of the spectral weight between the multiple harmonics, presents their splitting, and shows the presence of the incoherent in-gap states. Like in Fig. 4.6, we observe zero-harmonic and higher-order modes along $\varepsilon_d^0 \pm n\omega$, which are mixed with the continuous background. In the high-frequency limit, the quasiparticle energies (zero-level) resemble the stationary Andreev states, whereas the continuum electron spectrum is far outside the energy gap. For such driven system, the superconducting energy gap is manifested in a unique manner, its properties can not be treated like in a static situation.

4.4 Floquet-Magnus expansion

In the high frequency limit, the Floquet Hamiltonian H^F can be expanded in powers of the perturbation, called the Floquet-Magnus expansion [127, 133]

$$H_{t_0}^F = \sum_{\nu=1}^{\infty} H_{t_0}^{F(\nu)}. \tag{4.57}$$

The first part is the zero component of Fourier transform of Hamiltonian

$$H_{t_0}^{F(1)} = \hat{H}_0 \tag{4.58}$$

and the second is defined as follows

$$H_{t_0}^{F(2)} = \sum_{m\neq 0} \frac{1}{m\hbar\omega} \left[\hat{H}_m \hat{H}_{-m} + e^{im\omega t_0} \left[\hat{H}_0, \hat{H}_m \right] \right]. \tag{4.59}$$

Here, the Fourier transform is defined as previously $\hat{H}_m = \frac{1}{T}\int_0^T dt e^{im\omega t} H(t)$. This high frequency expansion can be adapted to the proximitized quantum dot Hamiltonian introduced in (3.7) with the oscillating quantum dot energy level

$$\hat{H}(t) = \sum_{\sigma} \left(\varepsilon_d^0 + A\cos(\omega t) \right) \hat{d}_\sigma^\dagger \hat{d}_\sigma + \frac{\Gamma_S}{2} \left(\hat{d}_\downarrow^\dagger \hat{d}_\uparrow^\dagger + h.c. \right). \tag{4.60}$$

The Fourier transform of Hamiltonian (4.60) can be performed in few mathematical steps, presented below

$$\begin{aligned}
&\hat{H}_m = \frac{1}{T}\int_0^T e^{im\omega t} H(t) = \\
&\sum_\sigma \frac{1}{T}\int_0^T e^{im\omega t}\left(\sum_\sigma \left(\varepsilon_d^0 + A\cos(\omega t)\right)\hat{d}_\sigma^\dagger \hat{d}_\sigma + \frac{\Gamma_S}{2}\left(\hat{d}_\downarrow^\dagger \hat{d}_\uparrow^\dagger + h.c.\right)\right) = \\
&\sum_\sigma \frac{1}{T}\int_0^T e^{im\omega t}\varepsilon_d^0 \hat{d}_\sigma^\dagger \hat{d}_\sigma + \sum_\sigma \frac{1}{T}\int_0^T e^{im\omega t} A\frac{1}{2}\left(e^{-i\omega t} + e^{i\omega t}\right)\hat{d}_\sigma^\dagger \hat{d}_\sigma \\
&+ \sum_\sigma \frac{1}{T}\int_0^T e^{im\omega t}\frac{\Gamma_S}{2}\hat{d}_\downarrow^\dagger \hat{d}_\uparrow^\dagger + \sum_\sigma \frac{1}{T}\int_0^T e^{im\omega t}\frac{\Gamma_S}{2}\hat{d}_\uparrow \hat{d}_\downarrow = \\
&\delta_{0,m}\left(\sum_\sigma \varepsilon_d^0 \hat{d}_\sigma^\dagger \hat{d}_\sigma + \frac{\Gamma_S}{2}\hat{d}_\downarrow^\dagger \hat{d}_\uparrow^\dagger + \frac{\Gamma_S}{2}\hat{d}_\uparrow \hat{d}_\downarrow\right) + \sum_\sigma \frac{1}{T}\int_0^T e^{im\omega t}\frac{A}{2}e^{-i\omega t(1-m)}\hat{d}_\sigma^\dagger \hat{d}_\sigma \\
&+ \sum_\sigma \frac{1}{T}\int_0^T e^{im\omega t}\frac{A}{2}e^{i\omega t(1+m)}\hat{d}_\sigma^\dagger \hat{d}_\sigma. \qquad (4.61)
\end{aligned}$$

In the result, we obtain the Hamiltonian as follows

$$\hat{H}_m = \delta_{0,m}\left(\sum_\sigma \varepsilon_d^0 \hat{d}_\sigma^\dagger \hat{d}_\sigma + \frac{\Gamma_S}{2}\hat{d}_\downarrow^\dagger \hat{d}_\uparrow^\dagger + \frac{\Gamma_S}{2}\hat{d}_\uparrow \hat{d}_\downarrow\right) + \left(\delta_{1,m} + \delta_{1,-m}\right)\frac{A}{2}\sum_\sigma \hat{d}_\sigma^\dagger \hat{d}_\sigma, \quad (4.62)$$

where the diagonal elements are connected to the discrete quantum dot energy level ε_d^0 and the superconducting order parameter defined by $\Gamma_S/2$. The off-diagonal elements are the result of the driving in the system. The first element of the Floquet-Magnus expansion, which is the zero element of Fourier transformed Hamiltonian, is equal to

$$H_{t_0}^{F(1)} = \hat{H}_0 = \sum_\sigma \varepsilon_d^0 \hat{d}_\sigma^\dagger \hat{d}_\sigma + \frac{\Gamma_S}{2}\hat{d}_\downarrow^\dagger \hat{d}_\uparrow^\dagger + \frac{\Gamma_S}{2}\hat{d}_\uparrow \hat{d}_\downarrow. \qquad (4.63)$$

The block form of the Floquet Hamiltonian acquires the symmetry property $\hat{H}_{-1} = \hat{H}_1 = \frac{A}{2}\sum_\sigma \hat{d}_\sigma^\dagger \hat{d}_\sigma$. The second element of the expansion can be calculated

as follows

$$
\begin{aligned}
&H_{t_0}^{F(2)} = \sum_{m\neq 0} \frac{1}{m\hbar\omega}\left[\hat{H}_m\hat{H}_{-m} + e^{im\omega t_0}\left[\hat{H}_0,\hat{H}_m\right]\right] = \\
&-\frac{1}{\hbar\omega}\left(\hat{H}_{-1}\hat{H}_1 + e^{-im\omega t_0}[\hat{H}_0,\hat{H}_{-1}]\right) + \frac{1}{\hbar\omega}\left(\hat{H}_{-1}\hat{H}_1 + e^{im\omega t_0}[\hat{H}_0,\hat{H}_1]\right) = \\
&\frac{1}{\hbar\omega}\left(\hat{H}_{-1}\hat{H}_1 + e^{im\omega t_0}[\hat{H}_0,\hat{H}_1] - \hat{H}_{-1}\hat{H}_1 - e^{-im\omega t_0}[\hat{H}_0,\hat{H}_{-1}]\right) = \\
&\frac{1}{\hbar\omega}\left([\hat{H}_1,\hat{H}_{-1}] + e^{im\omega t_0}[\hat{H}_0,\hat{H}_1] - e^{-im\omega t_0}[\hat{H}_0,\hat{H}_{-1}]\right) = \\
&\frac{1}{\hbar\omega}\left([\hat{H}_1,\hat{H}_{-1}] + e^{im\omega t_0}[\hat{H}_0,\hat{H}_1] - e^{-im\omega t_0}[\hat{H}_0,\hat{H}_1]\right) = \\
&\frac{1}{\hbar\omega}\left([\hat{H}_1,\hat{H}_{-1}] + \left(e^{im\omega t_0} - e^{-im\omega t_0}\right)[\hat{H}_0,\hat{H}_1]\right).
\end{aligned}
\tag{4.64}
$$

This expansion requires to calculate two commutators of different Floquet matrix Hamiltonian $[\hat{H}_1,\hat{H}_{-1}] = 0$, $[\hat{H}_0,\hat{H}_1] = -A\frac{\Gamma_S}{2}\hat{d}^\dagger_\downarrow\hat{d}^\dagger_\uparrow + A\frac{\Gamma_S}{2}\hat{d}_\uparrow\hat{d}_\downarrow$. Substituting the solution of the calculated commutators into (4.64) the second term of the expansion is

$$
H_{t_0}^{F(2)} = \frac{2i\sin(\omega t_0)}{\hbar\omega}\left(A\frac{\Gamma_S}{2}\hat{d}_\uparrow\hat{d}_\downarrow - A\frac{\Gamma_S}{2}\hat{d}^\dagger_\downarrow\hat{d}^\dagger_\uparrow\right). \tag{4.65}
$$

In this case, the higher order terms vanish. The final expansion of the Hamiltonian which is truncated to the second term $H^F_{t_0} = H^{F(1)}_{t_0} + H^{F(2)}_{t_0}$, takes form

$$
H^F_{t_0} = \sum_\sigma \varepsilon^0_d\hat{d}^\dagger_\sigma\hat{d}_\sigma + \left(\frac{\Gamma_S}{2} - i\frac{A\Gamma_S}{\hbar\omega}\sin(\omega t_0)\right)d^\dagger_\downarrow d^\dagger_\uparrow + \left(\frac{\Gamma_S}{2} + i\frac{A\Gamma_S}{\hbar\omega}\sin(\omega t_0)\right)\hat{d}_\uparrow\hat{d}_\downarrow. \tag{4.66}
$$

The expansion of the Hamiltonian in the high frequency regime rescales the induced on-dot pairing potential. The high frequency expansion results are consistent with the Green's function calculations (for large frequencies) presented in Fig. 4.6.

4.5 Summary

In this chapter we studied an effective spectrum of the driven quantum dot placed between the superconducting and metallic reservoirs. The single

quantum dot energy level was periodically stimulated by the external potential. We have analysed the effective spectrum with respect to the amplitude A and frequency ω of the drive. We found that the proximity induced electron pairing leads to the splitting of each harmonic level. The maximum distance between mixed states slightly decreases with larger amplitude of the drive. In quasiparticle spectrum, distribution of the harmonics is controlled by the amplitude to frequency ratio.

The charge transport averaged over a period of driven oscillations and its differential conductance were also analysed. In the plots of differential conductance, we detected the multi-harmonic quasiparticle energies, their splitting and the distribution of the spectral weights.

Additionally, we studied the influence of the finite size of the superconducting energy gap on the quasiparticle spectrum. In a case, when the amplitude of oscillations exceeds the energy gap the incoherent states appear in the subgap regime. Those states correspond to short-time living quasiparticles and emerge near such values of the amplitude to frequency ratio, where the spectral weight of the zeroth harmonic vanishes.

Chapter 5

Dynamics of Andreev states in double quantum dot system

This chapter presents description of the dynamical effects obtained for a double quantum dot system (N-DQD-S), schematically presented in Fig. 5.1. We consider geometry in which the quantum dots are placed in series between the metallic and the superconducting leads. Theoretical analysis of such system gives rise to the possible qubit development. The qubit based on the double quantum dot and similar layouts has been studied by several scientific groups [56–59]. Knowledge about dynamical properties of the system would be important for sequential manipulation and operation on them.

In this section, we explore the time-dependent processes related to the creation of bound states and other properties that describe the evolution of the system. Specifically, we study transient effects and the evolution of the system after step-like or continuous changes in its parameters. In particular, we investigate the following quench protocols: transient effects (Sec. 5.3), rapid change of source-drain voltage (Sec. 5.4), quench in energy level position (Sec. 5.5), periodic driving (Sec. 5.6).

5.1 Model Hamiltonian

The heterostructure, consisting of the two quantum dots QD_i $(i = 1, 2)$ placed in linear configuration between the normal (N) and superconducting (S) leads, can be described by the following Hamiltonian

$$\hat{H} = \hat{H}_S + \hat{H}_{S-QD_1} + \hat{H}_{DQD} + \hat{H}_{N-QD_2} + \hat{H}_N. \tag{5.1}$$

The double quantum dot term is modelled by the single-level localized states

$$\hat{H}_{DQD} = \sum_{i\sigma} \varepsilon_{i\sigma} \hat{c}^\dagger_{i\sigma} \hat{c}_{i\sigma} + U_i \hat{n}_{i\uparrow} \hat{n}_{i\downarrow} + \sum_{\sigma} \left(V_{12} \hat{c}^\dagger_{1\sigma} \hat{c}_{2\sigma} + \mathrm{h.c.} \right), \tag{5.2}$$

where $\hat{c}^\dagger_{i\sigma}(\hat{c}_{i\sigma})$ is the creation (annihilation) operator of electron at i-th quantum dot, $\varepsilon_{i\sigma}$ denote the energy levels, and V_{12} is the interdot coupling. We also consider electron-electron Coulomb repulsion between electrons localized on quantum dots $U_i \hat{n}_{i\uparrow} \hat{n}_{i\downarrow}$.

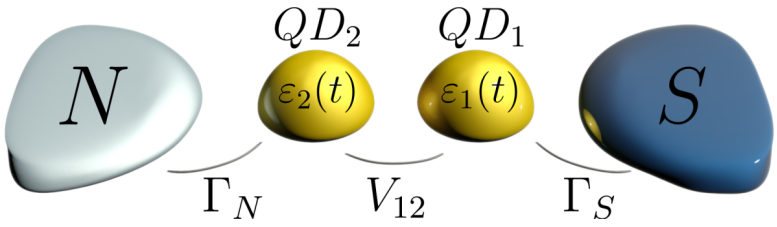

Figure 5.1: Illustration of double quantum dot's sytem placed between the normal metallic and the superconducting reservoirs [134].

The quantum dots are hybridized with the external reservoirs via

$$\hat{H}_{N-QD_2} = \sum_{k\sigma} \left(V_{Nk} \hat{c}^\dagger_{Nk\sigma} \hat{c}_{2\sigma} + \mathrm{h.c.} \right) \tag{5.3}$$

and

$$\hat{H}_{S-QD_1} = \sum_{q\sigma} \left(V_{Sq} \hat{c}^\dagger_{Sq\sigma} \hat{c}_{1\sigma} + \mathrm{h.c.} \right), \tag{5.4}$$

where V_{Nk} (V_{Sq}) denotes the coupling to normal (superconducting) lead.

In absence of the metallic lead $(\Gamma_N = 0)$ and for the superconducting atomic limit $(\Delta_{sc} = \infty)$ the Hilbert space of the proximitized DQD is spanned

by 16 vectors. In the occupancy representation the matrix Hamiltonian has a block structure, consisting of 6 subspaces [135]. Two 4-dimensional subspaces contain states with odd number of electrons $|\mathrm{QD}_2,\mathrm{QD}_1\rangle \Rightarrow |0,\uparrow\rangle$, $|\uparrow,0\rangle$, $|\uparrow\downarrow,\uparrow\rangle$, $|\uparrow,\uparrow\downarrow\rangle$ and $|0,\downarrow\rangle$, $|\downarrow,0\rangle$, $|\uparrow\downarrow,\downarrow\rangle$, $|\downarrow,\uparrow\downarrow\rangle$, respectively. The next two states $|\uparrow,\uparrow\rangle$, $|\downarrow,\downarrow\rangle$ are decoupled from other ones. The remaining 6-dimensional subspace contains the states with even number of electrons, $|0,0\rangle$, $|0,\uparrow\downarrow\rangle$, $|\uparrow\downarrow,0\rangle$, $|\uparrow\downarrow,\uparrow\downarrow\rangle$, $|\uparrow,\downarrow\rangle$ and $|\downarrow,\uparrow\rangle$, respectively. Diagonalizing the effective matrix Hamiltonian for $U_i = 0$, one obtains the following eigenvalues ϵ_i and eigenfunctions $|\phi_i\rangle$:

i	ϵ_i	$\lvert\phi_i\rangle$
$1/2$	$\pm E$	$a_i(\lvert 0,\uparrow\rangle \mp \lvert\uparrow\downarrow,\uparrow\rangle) + b_i(\pm\lvert\uparrow,0\rangle \pm \lvert\uparrow,\uparrow\downarrow\rangle)$
$3/4$	$\pm E \mp \Gamma_S/2$	$a_i(\lvert 0,\uparrow\rangle \pm \lvert\uparrow\downarrow,\uparrow\rangle) + b_i(\lvert\uparrow,0\rangle \mp \lvert\uparrow,\uparrow\downarrow\rangle)$
$5/6$	$\pm E$	$a_i(\lvert 0,\downarrow\rangle \mp \lvert\uparrow\downarrow,\downarrow\rangle) + b_i(\lvert\downarrow,0\rangle \pm \lvert\downarrow,\uparrow\downarrow\rangle)$
$7/8$	$\pm E \mp \Gamma_S/2$	$a_i(\lvert 0,\downarrow\rangle \pm \lvert\uparrow\downarrow,\downarrow\rangle) + b_i(\lvert\downarrow,0\rangle \mp \lvert\downarrow,\uparrow\downarrow\rangle)$
9	0	$\lvert\uparrow,\uparrow\rangle$
10	0	$\lvert\downarrow,\downarrow\rangle$
11	0	$\frac{\sqrt{2}}{\sqrt{4V_{12}^2+\Gamma_S^2/4}}(V_{12}(\lvert 0,0\rangle + \lvert\uparrow\downarrow,\uparrow\downarrow\rangle)$ $-\frac{\Gamma_S}{4}(\lvert\uparrow,\downarrow\rangle - \lvert\downarrow,\uparrow\rangle))$
12	0	$\frac{1}{\sqrt{2}}(\lvert\uparrow,\downarrow\rangle - \lvert\downarrow,\uparrow\rangle)$
13/14	$\pm\Gamma_S/2$	$\frac{1}{2}\left(\lvert 0,0\rangle - \lvert\uparrow\downarrow,\uparrow\downarrow\rangle \pm \lvert 0,\uparrow\downarrow\rangle \mp \lvert\uparrow\downarrow,0\rangle\right)$
15/16	$\pm\sqrt{4V_{12}^2+\Gamma_S^2/4}$	$\frac{\Gamma_S}{4\sqrt{4V_{12}^2+\Gamma_S^2/4}}(\lvert 0,0\rangle + \lvert\uparrow\downarrow,\uparrow\downarrow\rangle)$ $\pm\frac{1}{2}(\lvert 0,\uparrow\downarrow\rangle + \lvert\uparrow\downarrow,0\rangle) +$ $\frac{V_{12}}{\sqrt{4V_{12}^2+\Gamma_S^2/4}}(\lvert\uparrow,\downarrow\rangle \mp \lvert\downarrow,\uparrow\rangle)$

Table 5.1: Table of the eigenenergies and eigenfunctions of the uncorrelated proximitized double quantum dot system obtained for $\Gamma_N = 0$, $\Delta_{sc} = \infty$ [134].

where $E = \frac{1}{2}\left(\sqrt{4V_{12}^2+\Gamma_S^2/4}+\Gamma_S/2\right)$, $a_i = \frac{1}{\sqrt{2}}\frac{V_{12}}{\sqrt{V_{12}^2+E_i^2}}$ and $b_i = \frac{1}{\sqrt{2}}\frac{E_i}{\sqrt{V_{12}^2+E_i^2}}$.

The repulsive on-dot interactions $U_i\hat{n}_{i\uparrow}\hat{n}_{i\downarrow}$ compete with the proximity-induced electron pairing, leading to important changes of the bound states. Here, we consider their influence on dynamical phenomena within the mean-field approximation, using the Hartree-Fock-Bogoliubov decoupling scheme

$$\hat{n}_{i\uparrow}\hat{n}_{i\downarrow} \simeq \hat{n}_{i\uparrow}\langle\hat{n}_{i\downarrow}\rangle + \hat{n}_{i\downarrow}\langle\hat{n}_{i\uparrow}\rangle + \hat{c}^{\dagger}_{i\uparrow}\hat{c}^{\dagger}_{i\downarrow}\langle\hat{c}_{i\downarrow}\hat{c}_{i\uparrow}\rangle + \hat{c}_{i\downarrow}\hat{c}_{i\uparrow}\langle\hat{c}^{\dagger}_{i\uparrow}\hat{c}^{\dagger}_{i\downarrow}\rangle. \tag{5.5}$$

The Coulomb interactions and the superconducting proximity effect can be described by the effective mean-field Hamiltonian

$$\begin{aligned} H_{eff} \approx & \sum_{i,\sigma}\tilde{\varepsilon}_{i\sigma}(t)\hat{c}^{\dagger}_{i\sigma}\hat{c}_{i\sigma} - \sum_{i}\left(\Delta_i(t)\hat{c}^{\dagger}_{i\uparrow}\hat{c}^{\dagger}_{i\downarrow} + \text{h.c.}\right) + \sum_{\sigma}\left(V_{12}\hat{c}^{\dagger}_{1\sigma}\hat{c}_{2\sigma} + \text{h.c.}\right) \\ & + \sum_{k\sigma}\left(V_{Nk}\hat{c}^{\dagger}_{Nk\sigma}\hat{c}_{2\sigma} + \text{h.c.}\right) + \sum_{k\sigma}\xi_{Nk\sigma}\hat{c}^{\dagger}_{Nk\sigma}\hat{c}_{Nk\sigma}, \end{aligned} \tag{5.6}$$

where $\tilde{\varepsilon}_{i\sigma}(t) = \varepsilon_{i\sigma}(t) - U_i n_{i\sigma}(t)$, $\Delta_1(t) = \frac{\Gamma_S}{2} - U_1\langle\hat{c}_{1\downarrow}(t)\hat{c}_{1\uparrow}(t)\rangle$, $\Delta_2(t) = U_2\langle\hat{c}_{2\downarrow}(t)\hat{c}_{2\uparrow}(t)\rangle$. Such approximation would be reliable only in the weak interaction case ($U < \Gamma_S$).

5.2 Selected experimental realization

The double quantum dot heterostructure has been studied intensively theoretically and experimentally by various groups [57, 136–138]. These investigations established, that in this system the manipulation of spin and its readout are experimentally accessible [56–58]. Such possibilities provide opportunity to construct a qubit based on a double quantum dot, as proposed by DiVincenzo [59] for both normal leads and in Ref. [139] for the superconducting electrodes, respectively.

Recently, the double quantum dot system Fig.5.1 has been further studied experimentally, revealing the Andreev blockade effect [64]. Mechanism of such Andreev blockade relies on the triplet configuration of electrons in quantum dots [60, 140, 141], which suppresses the Andreev reflection processes, thus blocking the flow of current. This configuration offers many possibilities for

investigating time-dependent properties and post-quench dynamics, which will be addressed in this chapter.

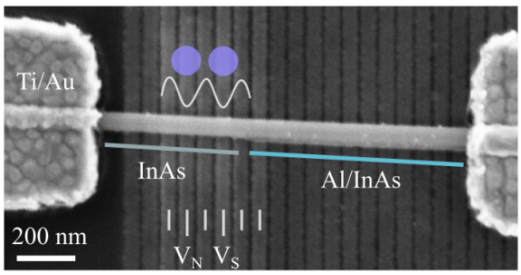

Figure 5.2: Example of the experimental realisation of the double quantum dot system, using InAs nanowire [64].

5.3 Transient effects

We start by investigating the transient effects of the double quantum dot system, similarly as has been done for the junction with the single quantum dot [Sec. 3.4]. All results for the double quantum dot system have been obtained by the equation of motion technique (for details see Sec. 3.3). To calculate the current flowing to the normal lead $j_{N\sigma}(t)$ we modify the formula (3.20) to following form

$$j_{N\sigma}(t) = 2\,\mathrm{Im}\left[\sum_k V_k e^{-i\varepsilon_{k\sigma}t}\langle \hat{d}^\dagger_{2\sigma}(t)\hat{c}_{k\sigma}(0)\rangle - \frac{i\Gamma_{N\sigma}}{2}\langle \hat{n}_{2\sigma}(t)\rangle\right], \tag{5.7}$$

which has been formally derived in Ref. [117]. For numerical purposes, we had to solve the set of coupled differential equations, which are presented in Appendix A.2.

Like in Sec. 3.4, let us present the result for the evolution from the initial conditions to the equilibrium state. We assume that initially, at $t \leq 0$, the quantum dots are disconnected from both external reservoirs and next they are rapidly connected to the electrodes at $t = 0^+$. Fig. 5.3 presents numerical results obtained for currents $j_{N\uparrow}(t)$, $j_{S\uparrow}(t)$, occupancy of quantum dots $n_{i\uparrow}(t)$ and the real part of the order parameter $\chi_i(t) = \langle \hat{d}_{i\downarrow}(t)\hat{d}_{i\uparrow}(t)\rangle$. For

zero source-drain voltage, we observe the evolution of the system towards an equilibrium state for initially empty quantum dots. In this scenario, the oscillations in currents and occupations are mainly caused by the flow of Cooper pairs into and out of the system. Those oscillations are dumped in time due to presence of a continuum of free electrons of the metallic lead. The buildup of the order parameter for individual quantum dots is presented in the plot of $\mathrm{Re}\chi_i(t)$. Imaginary part of $\chi_i(t)$ is negligibly small ($\sim 10^{-7}$).

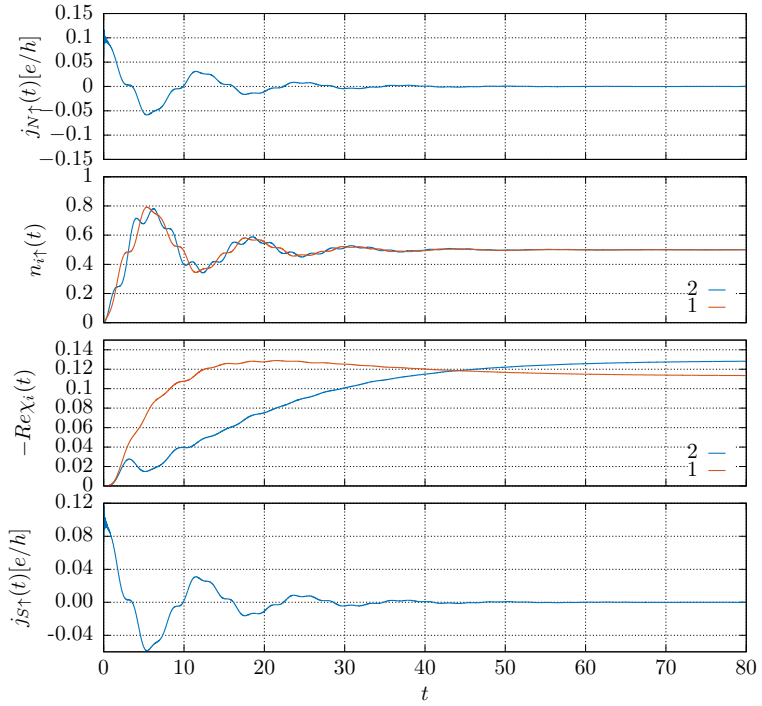

Figure 5.3: The transient evolution of currents $j_{N\uparrow}(t)$, $j_{S\uparrow}(t)$, occupancy $n_{i\uparrow}(t)$ and the order parameter $\mathrm{Re}\,\chi_i(t)$, imposing a sudden coupling of the quantum dot to both external leads at $t = 0^+$ for initial occupancy $(n_\uparrow(0), n_\downarrow(0))$. The results are obtained for zero source-drain voltage and system parameters: $\varepsilon_{di} = 0$, $V_{12} = 1$, $\Gamma_N = 0.2$, $\Gamma_S = 1$, $U = 0$.

We observe rapid development of $\chi_1(t)$ in time and delayed with respect to it formation of the order parameter in the second quantum dot. The character of this buildup of the order parameters directly depends on the strength to

the superconductor Γ_S and the coupling between quantum dots V_{12}.

Development of the bound states can by practically detected by the differential conductance. Using the definition of the time-dependent differential conductance $G_{N\sigma}(V_{sd},t) = \frac{d}{dV_{sd}} j_{N\sigma}(t)$ we present the transient evolution of the uncorrelated system in Fig. 5.4 and the correlated system in Fig. 5.5. These figures present the the differential conductance versus time and the source-drain voltage V_{sd} lifting the chemical potential of metallic lead ($\mu_N = V_{sd}, \mu_S = 0$) for various interdot couplings and the Coulomb potential. The transient evolution of the system exhibits emergence of the Andreev bound states induced by the proximity effect in the quantum dots. The Andreev bound states appearing in $G_{N\sigma}(V_{sd},t)$ can be interpreted as the excitation energies between eigenstates with the even and odd number of electrons. In the stationary limit ($t \to \infty$) the peaks occur at $E = \pm\frac{1}{2}\left(\sqrt{4V_{12}^2 + \Gamma_S^2/4} \pm \Gamma_S/2\right)$ (for the uncorrelated case and $\varepsilon_{i\sigma} = 0$). Their broadening is caused by the relaxation processes on a continuous spectrum of the metallic lead.

In the correlated case (Fig. 5.5) we observe substantial reorganization of the bound states. For larger U we observe smaller separation between their position, see panels in the first and second column of Fig. 5.5. This tendency proves, that the Coulomb repulsion suppresses the effects of the interdot hybridization and the superconducting proximity effect. In the third and fourth column of Fig. 5.5, the peaks merge, but presumably this is an artificial consequence of the mean-field approximation which is hardly reliable for the strongly correlated limit $U > \Gamma_S$.

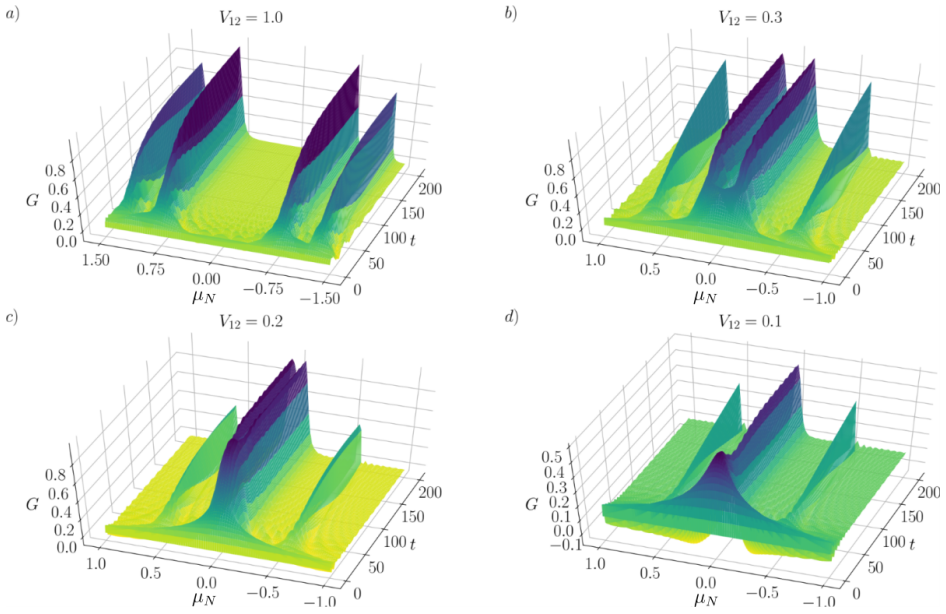

Figure 5.4: The transient evolution of the differential conductance $G = G_{N\sigma}(V_{sd}, t)$ (in units of $2e^2/h$) with respect to source-drain voltage $V_{sd} = \mu_N$ and time t, obtained for $V_{12} = 1, 0.3, 0.2, 0.1$, respectively. We used the model parameters: $\varepsilon_{i\sigma} = 0$, $\Gamma_N = 0.1$, $\Gamma_S = 1$, $U = 0$ [142].

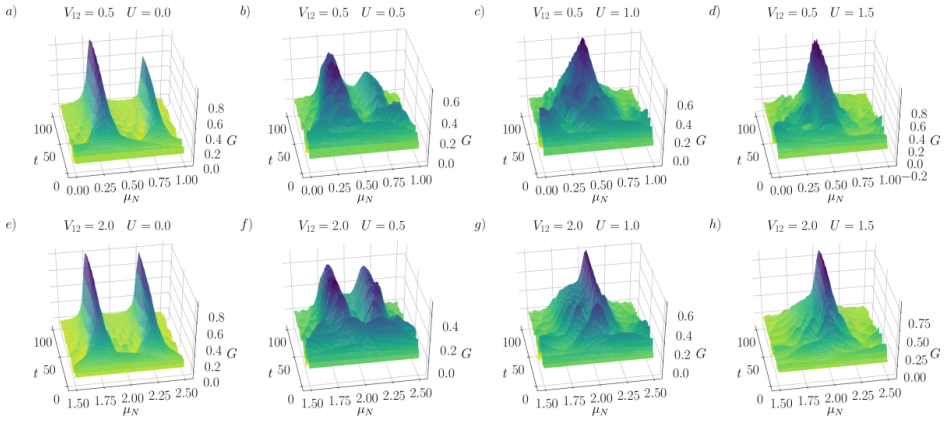

Figure 5.5: The transient evolution of the differential conductance $G = G_{N\sigma}(V_{sd}, t)$ (in units of $2e^2/h$) with respect to source-drain voltage $V_{sd} = \mu_N$ and time t, obtained in the weak $V_{12} = 0.5$ (upper row) and strong interdot coupling limit $V_{12} = 2$ (bottom row) for several values of the Coulomb potential (as indicated) for: $\varepsilon_{i\sigma} = -U/2$, $\Gamma_N = 0.1$, $\Gamma_S = 1$ [142].

5.4 Dynamics induced by abrupt source-drain voltage

In analogy to the single quantum dot system (Sec. 3.5) we analyze dynamics caused by a rapid change of the source-drain voltage. The components of N-DQD-S system are initially disconnected (till $t = 0$) and they are coupled at $t = 0^+$, exhibiting the transient evolution presented in Fig. 5.6. We observe

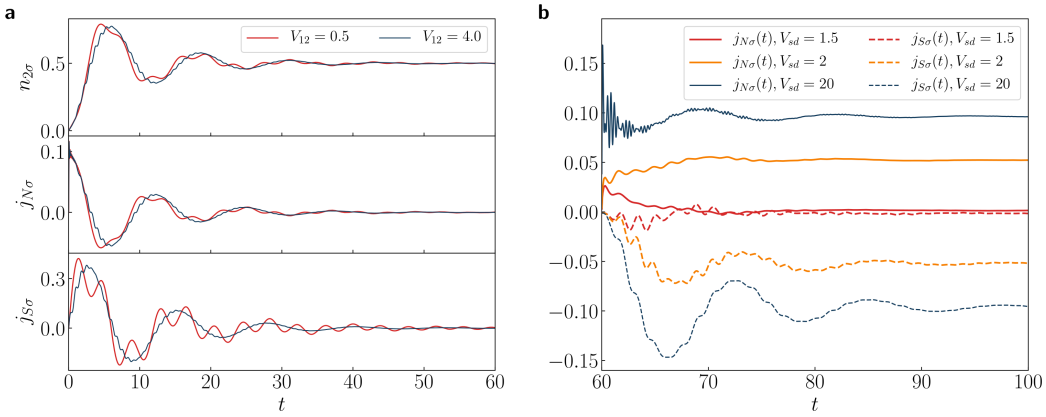

Figure 5.6: The time-dependent currents (in units of e/h) and quantum dot's occupancy (a), after a sudden coupling of the quantum dots to both external leads at $t = 0^+$. The post-quench evolution (b) after applying the source-drain voltage V_{sd} at $t = 60$. Results are obtained for: $\varepsilon_{i\sigma} = 0$, $\Gamma_N = 0.2$, $\Gamma_S = 1$, $U = 0$ [134].

the relaxation process imposed on top of the quantum oscillations of the characteristics. The steady state is approximately achieved at $t \simeq 60$, after a sequence of quantum oscillations, damped in time with the exponential envelope function $e^{-t\Gamma_N/2}$. Frequency of the quantum oscillations coincide with quasiparticle energies of the in-gap bound states of N-DQD-S heterostructure. In particular, for $\varepsilon_{i\sigma} = 0$, the period is equal to $T = 4\pi/\Gamma_S$.

At $t = 60$ we perform the quench, applying the source-drain voltage. Rapid change of the chemical potential of the metallic lead induces the charge flow through the system. The oscillating currents $j_{N\sigma}(t)$ and $j_{S\sigma}(t)$, are shown in Fig. 5.6b and Fig. 5.7 for different interdot coupling values. Here, the superconducting lead is grounded and the source-drain voltage

$V_{sd} = \mu_N - \mu_S$ lifts the chemical potential μ_N. For the source-drain voltage much larger than the interdot coupling $|V_{sd}| \gg V_{12}$, we notice emergence of the quantum beats with the time period $T_B = \pi/V_{12}$ superimposed with higher frequency oscillations. The appearance of these quantum beats originates from a superposition of the sinusoidal waves of different frequencies. An analogy of this phenomenon can be found in acoustics, where an interference pattern results from the superposition of several sound waves of slightly different frequencies. In the present case for $\varepsilon_{i\sigma} = 0$, $\Gamma_N = 0$, $U = 0$, the charge transport involves the Andreev scattering related to position of the in-gap bound states, which are formed at energies $E = \pm\frac{1}{2}(\sqrt{4V_{12}^2 + \Gamma_S^2/4} \pm \Gamma_S/2)$. It has been shown [120–122], that for the single quantum dot coupled to the normal leads, the jump of the source-drain voltage induces coherent oscillations in the current characteristics, with frequency $\omega = |V_{sd} - \varepsilon_d|$. For the double quantum dot setup, we should replace the quantum dot energy level by the four quasiparticle energies at which the Andreev scattering is amplified. Taking into account the number of these quasiparticle energies, the total current is a superposition of sinusoidal waves $\sum_{i=1}^{4} a_i e^{-\lambda_i t} \sin(\Omega_i t)$, with frequencies $\Omega_{1/2} = V_{sd} \pm \omega_1$ and $\Omega_{3/4} = V_{sd} \pm \omega_2$, where $\omega_{1/2} = V_{12} \pm \Gamma_S/4$. The sinusoidal waves are damped with corresponding parameters λ_i and multiplied by the coefficients a_i which control the the contributions to total current from these in-gap bound states.

In Ref. [143], the authors have shown that in the normal junction the beating pattern depends on the ratio

$$r = \frac{\omega_1 + \omega_2}{|\omega_1 - \omega_2|}, \tag{5.8}$$

which can be applied to our case. This ratio can be expressed by the coupling between the dots and hybridization to superconducting lead

$$r = \frac{4V_{12}}{\Gamma_S}. \tag{5.9}$$

The numerical results of $j_{N\sigma}(t)$ obtained for $V_{sd} = 20$ (Fig. 5.6b) show that

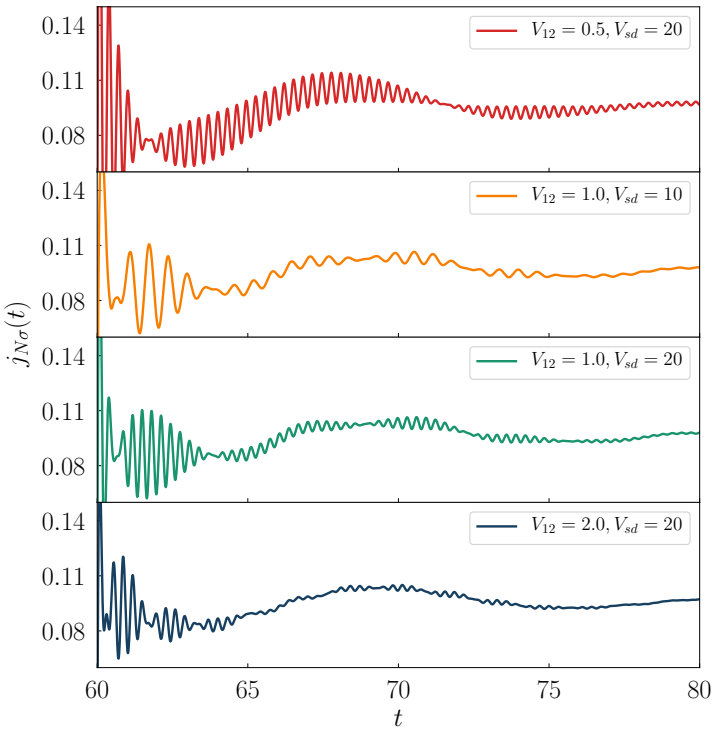

Figure 5.7: The post-quench currents $j_{N\sigma}(t)$ (in units of e/h), obtained for several values of the interdot coupling V_{12} and source-drain voltage V_{sd}, using: $\varepsilon_{i\sigma} = 0$, $\Gamma_N = 0.2$, $\Gamma_S = 1$, $U = 0$ [134].

the ratio is $r = 8$ and the following sequence of the beats can be detected: $\frac{\pi}{4}, 7 \times \frac{\pi}{2}$. If the ratio r is not an integer number, then the beating patterns are significantly more complex. The plot of $j_{N\sigma}(t)$ current shown in Fig. 5.6b indicates, that for large $V_{sd} = 20$ the post-quench evolution is mainly composed of the quantum oscillation with period $T_B = \pi/V_{12}$ superimposed with the faster oscillations, whose frequency is equal to V_{sd}. In the steady state limit, the current $j_{N\sigma}(t)$ is larger for $V_{sd} = 2$ than for $V_{sd} = 1.5$, because of the broader transport window which involves all in-gap Andreev bound states. Additionally, we notice that the current $j_{S\sigma}(t)$ differs from $j_{N\sigma}(t)$, and their difference is more pronounced upon increasing V_{sd}. We can attribute this behaviour to the fact that quantum dots between the external leads wash

out small fluctuations of the current $j_{S\sigma}(t)$. It also imposes the period of oscillations equal $4\pi/\Gamma_S$. A closer look on this beating structure presented in Fig. 5.7, displays the time-dependent current $j_{N\sigma}(t)$ after the abrupt rise of the source-drain voltage. Here, we clearly see the influence of the interdot coupling V_{12} on the interference pattern by observing the oscillations with time period $T_B = \pi/V_{12}$. In real measurements the period of beating oscillations could serve as a tool to evaluate the interdot coupling V_{12}. For example, if the coupling to the superconducting lead $\Gamma_S \sim 200\mu eV$ and $V_{12} = 0.5\Gamma_S$, $1\Gamma_S$ and $2\Gamma_S$ the beating period would be $T_B \sim 21$, 10 and 5 picoseconds, respectively. This time-scale is nowadays attainable experimentally.

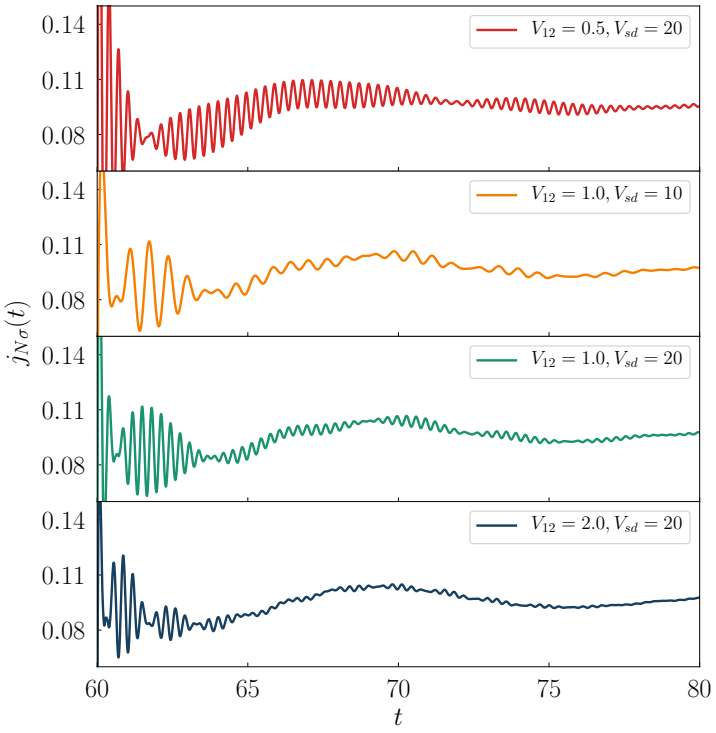

Figure 5.8: The same as in Fig. 5.7 but for the correlated half-filled quantum dots $U = 0.5$.

Fig. 5.8 displays results obtained for the correlated case assuming both quantum dots to be half-filled $\varepsilon_{i\sigma} = -U/2$. In this particular case, the evolution

after the quench looks almost the same as in Fig. 5.7. We notice only the slightly different shapes of the curves. Nevertheless, the oscillation period remains unchanged. The different profiles of the time evolution between uncorrelated and correlated cases can be explained by almost the same initial conditions right before the jump of the source-drain voltage. In both cases, the functions of quantum statistical averaging of operators $\langle \dots \rangle$ have almost the same values for half-filled scenario. In other cases than the half-filled scheme, we can expect analogous behaviour of the oscillations if initially (before the jump) the quantum statistical averaging of observables takes the same values with and without correlations.

5.5 Quench in the quantum dot energy levels

In this section, we explore dynamics of the double quantum dot system driven by the change of the quantum dot energy levels. We consider the sequence of quenches imposed on the quantum dot energy levels $\varepsilon_{i\sigma}$. First quench occurs at $t_1 = 60$, when the energy level of both quantum dots are raised up by the gate potential V_g: $\varepsilon_{i\sigma} \to \varepsilon_{i\sigma} + V_g$. Second quench takes place, when the system achieves a new stationary state (at time $t_2 = 120$), then we abruptly change the energy levels back to their initial values: $\varepsilon_{i\sigma} + V_g \to \varepsilon_{i\sigma}$.

Let us first inspect the quantum dot occupancy of the stationary limit $t \to \infty$ (Fig. 5.9) of the quantum dots with respect to the initial energy level $\varepsilon_{1\sigma} = \varepsilon_{2\sigma}$, for a few values of the interdot coupling V_{12}. We notice that quantum dot occupancies are almost identical $n_{1\sigma} \simeq n_{2\sigma}$. Here, we observe step-like functions of the charge occupancy characterized by plateau regions. Upon varying the energy level the charge evolves from the filled to nearly empty quantum dots, through the plateau regions corresponding to $n_{i\sigma} \approx 1$, 0.5, and 0, respectively. The width of the half-filling plateau region depends on the interdot coupling and we observe its contraction with smaller V_{12}. Changeover between plateau regions occurs at $\varepsilon_{i\sigma} \approx \pm V_{12}$.

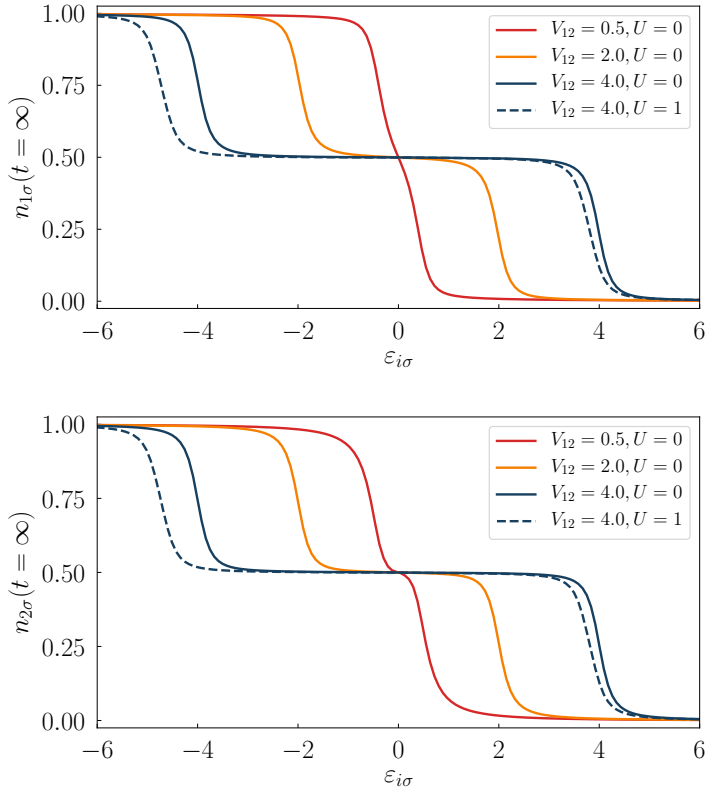

Figure 5.9: Charge occupancy of QD_i in the stationary limit as a function of the energy level $\varepsilon_{2\sigma} = \varepsilon_{1\sigma}$ determined for several interdot couplings V_{12}. The dashed line refers to the correlated system, $U = 1$. Results are obtained for: $V_{sd} = 0$, $\Gamma_N = 0.1$, $\Gamma_S = 1$ [134].

In Fig. 5.10, we present the current $j_{N\sigma}(t)$ obtained for the strong interdot coupling $V_{12} = 4$ and identical energy levels $\varepsilon_{i\sigma} = 0$. We display the post-quench evolution after the first and the second quench for several gate potentials $V_g = 3.0$, 3.2, 5, and 6, respectively. We notice that the post-quench evolution has the same general properties if the energy level position $\varepsilon_{i\sigma}$ corresponds to the same value of $n_{i\sigma}(t = \infty)$ for arbitrary V_{12}. We thus need only to consider the case of any value of the interdot coupling and a set of various jumps of $\varepsilon_{i\sigma}$.

In Fig. 5.11, we show $n_{2\sigma}(t)$, $j_{N\sigma}(t)$, $j_{S\sigma}(t)$ obtained for the interdot

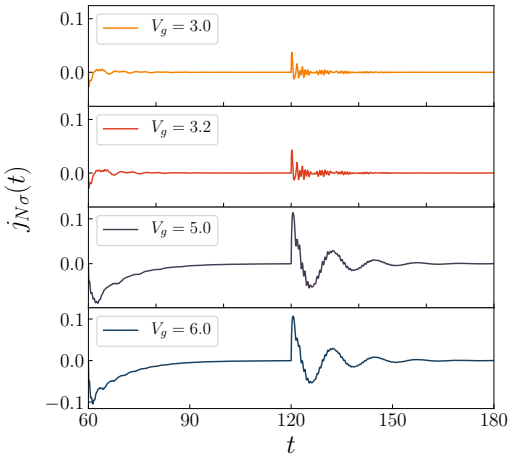

Figure 5.10: Evolution of $j_{N\sigma}(t)$ (in units of e/h), after step-like variation of the quantum dots energy levels $\varepsilon_{i\sigma} \to \varepsilon_{i\sigma} + V_g$ at $t = 60$ and $\varepsilon_{i\sigma} + V_g \to \varepsilon_{i\sigma}$ at $t = 120$. We assumed model parameters: $\varepsilon_{i\sigma} = 0$, $V_{12} = 4$, $V_{sd} = 0$, $\Gamma_N = 0.2$, $\Gamma_S = 1$, $U = 0$ [134].

coupling $V_{12} = 4$ and energy levels $\varepsilon_{i\sigma} = 0$, where the post-quench evolution after the first and the second quench had been obtained for gate potentials $V_g = 3.2$, 3.8, 4, and 5, respectively. Such values of V_g correspond to the quantum dot's occupancies equal to ~ 0.48, ~ 0.4, ~ 0.25 and ~ 0.015 (see Fig. 5.9). In the first case, the jump from $\varepsilon_{i\sigma} = 0$ to $\varepsilon_{i\sigma} + V_g = 3.2$ (top rows in Fig. 5.11), we notice that the stationary value $n_{2\sigma}(t \simeq 120) \simeq 0.48$ and it is nearly the same as the initial quantum dot occupancy $n_{2\sigma}(t = 60) = 0.5$. Therefore, $n_{2\sigma}(t)$ remains nearly unchanged exhibiting only small fluctuations. Likewise, the currents $j_{N\sigma}$ and $j_{S\sigma}$ exhibit negligibly small oscillations in their characteristics. After the second quench, the occupancy $n_{2\sigma}$ is almost intact ~ 0.5, but immediately after the quench the transient beating structure appears. For the larger amplitude V_g ($V_g = 3.8$ and $V_g = 4$), the fluctuations are more pronounced. We observe the oscillations with period $T = \pi/V_{12}$ and the beating structure with the period $T_B = 2\pi/\Gamma_S$. Rising the value of gate voltage V_g up to $V_g = 5$ and above, the evolution after the quench differs from the previous cases. After the first quench, $n_{2\sigma}$ (for $V_g = 5$) it shows almost exponential decay, down to nearly zero value with the damped oscillations.

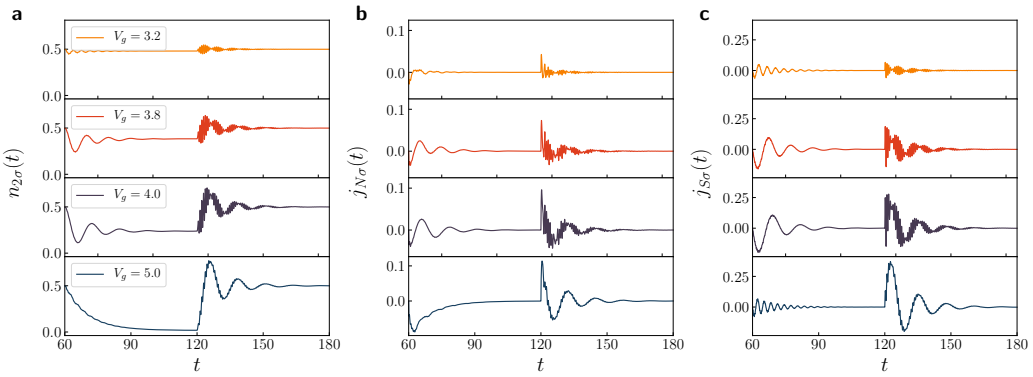

Figure 5.11: Evolution of the quantum dot's occupancy (a) and currents (b-c) (in units of e/h), after step-like variation of the quantum dots energy levels $\varepsilon_{i\sigma} \to \varepsilon_{i\sigma} + V_g$ at $t = 60$ and $\varepsilon_{i\sigma} + V_g \to \varepsilon_{i\sigma}$ at $t = 120$. We assumed model parameters: $\varepsilon_{i\sigma} = 0$, $V_{12} = 4$, $V_{sd} = 0$, $\Gamma_N = 0.2$, $\Gamma_S = 1$, $U = 0$ [134].

In the evolution, after the second quench, the oscillations of quantities with the period $T = 2\pi/\Gamma_S$ are visible without the beating structure. We conclude that, after the second quench, the beating structure appears if $\varepsilon_{i\sigma}$ corresponds to the slopes of $n_{2\sigma}(t = \infty)$ with respect to $\varepsilon_{2\sigma}$ (Fig. 5.9) and it is absent if $\varepsilon_{i\sigma}$ coincides to the bottom plateau of these same curves. For $V_{12} \leq 1$, the evolution after the first quench is similar to the case with large V_{12}, but after the second quench the beating patterns are not visible, only the oscillations with the period $4\pi/\Gamma_S$ can be detected.

We have also performed calculations considering the Coulomb interactions $U = 1$ and applying the same quench procedure, see Fig. 5.12. For $V_g = 3.35$, 4.0, 4.25 and 5.3 (which correspond to the tilted part of the curve calculated for $U = 1$ in Fig. 5.9), the occupancies $n_{2\sigma}$ are the same as in the uncorrelated case. In the post-quench evolution we obtain almost identical behaviour of all quantities. Like in previous chapter (Sec. 5.4), the initial conditions before the quench are almost the same for uncorrelated and correlated cases, which is the reason why the post-quench evolution is almost identical. This specific scenario presents the weak influence of the correlations on the post-quench

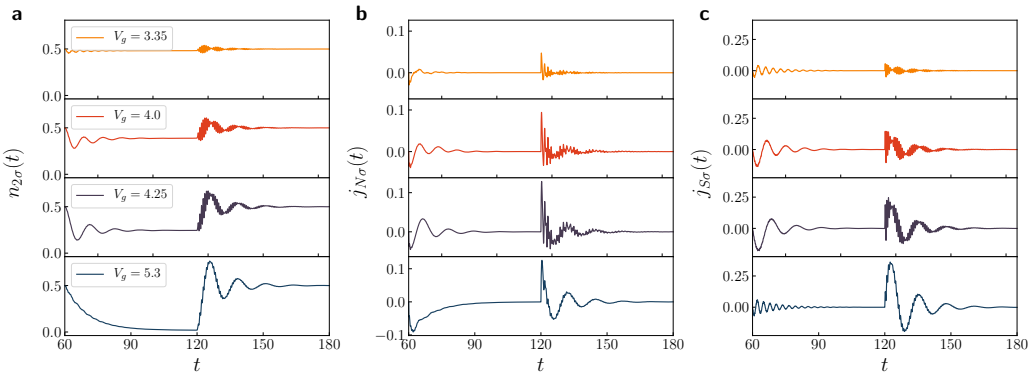

Figure 5.12: The same as in Fig. 5.11 but for the correlated system $U = 1$, assuming the initial energy levels $\varepsilon_{i\sigma} = -U/2$.

evolution. Notice that the results in Fig. 5.12 were obtained for $U = \Gamma_S$ on the borderline of applicability of the mean-field approximation. For larger Coulomb potential the calculations need to be done by more sophisticated methods.

5.6 Periodic driving of orbital level positions in DQD

We extended our investigation of driven systems, discussing the double quantum dot system under the drive of the energy levels $\varepsilon_{i\sigma}(t) = A\sin(\omega t)$. For simplicity, we assume that both quantum dots oscillate with the same amplitude A and frequency ω. Left panel in Fig. 5.13 presents the time-dependent current $j_{S\sigma}(t)$ obtained for $\omega = 0.1$ and for several amplitudes A, neglecting the correlation effects. The right panel in Fig. 5.13 presents the time-dependent current $j_{S\sigma}(t)$ for various Coulomb potentials U. Top panel of Fig. 5.13a shows the transient evolution of the unbiased system ($V_{sd} = 0$) which is characterized by damped oscillations with the time period $4\pi/\Gamma_S$. Similar behaviour of the time-dependent currents is visible in the next plots presented in the left panel. We observe different profiles of the quantum oscillations damped in time (up to $t = 20$) and the long-term fluctuations caused by the periodic driving appearing upon increasing amplitude A. In the

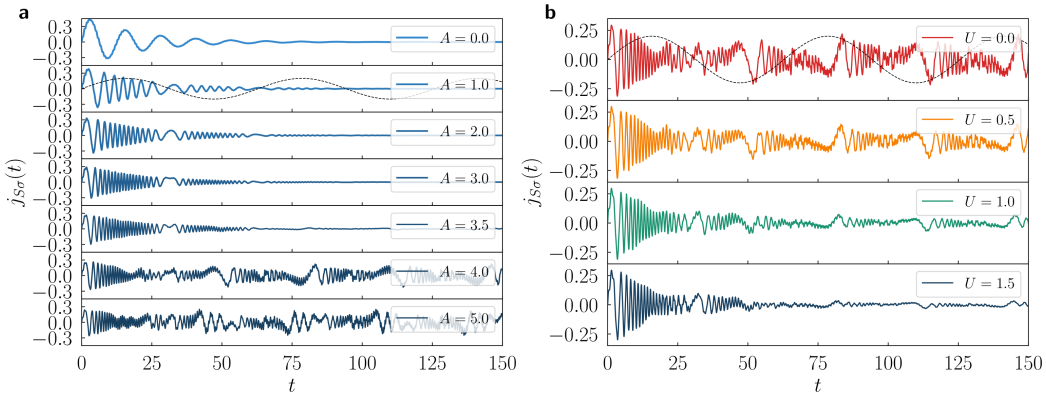

Figure 5.13: The time-dependent currents (in units of e/h) for the periodically driven $\varepsilon_{i\sigma}(t)$, where the oscillations are turned on at $t = 0^+$. The panel a) presents the results obtained for $V_{12} = 4$, $U = 0$ and several amplitudes A. The panel b) presents the results obtained within the mean-field approximation for $V_{12} = 3$, $A = 3$ and several values of U. The dashed line shows the profile of the oscillations energy levels (not in scale). The other model parameters: $V_{sd} = 0$, $\omega = 0.1$, $\Gamma_N = 0.1$, $\Gamma_S = 1$ [134].

case of strong interdot coupling, $V_{12} = 4$, we notice that the time-dependent currents vanish in the asymptotic limit for amplitudes $A \leq 3.5$ (see Fig. 5.13a). For $A \geq 3.5$, the amplitude A exceeds the energy of subgap quasiparticles therefore the oscillation of the time-dependent currents can be observed. It turns out that the current $j_{S\sigma}(t)$ remains oscillating through all time region, including the asymptotic limit $t \to \infty$. We observe that the period of this oscillatory behaviour matches with the driving period.

In the right panel in Fig. 5.13, we present the numerical results for the current $j_{S\sigma}(t)$ obtained for the Coulomb correlations $U_1 = U_2 = U$ within the mean-field approximation. For comparison, the upper curve in Fig. 5.13b presents the results for uncorrelated case. The results are obtained for the unbiased system $V_{sd} = 0$ with interdot coupling $V_{12} = 3$ and the driving amplitude $A = 3$. We note that this case, $V_{12} = A$, corresponds to the situation when the current $j_{S\sigma}(t)$ oscillates in the entire time window.

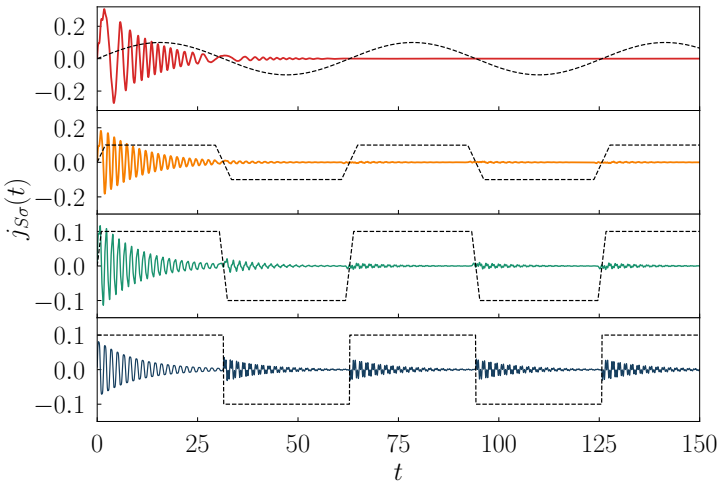

Figure 5.14: The time-dependent currents (in units of e/h) for the periodically driven $\varepsilon_{i\sigma}(t)$, where the oscillations are turned on at $t = 0^+$. The results are obtained for the different periodic driving schemes with profiles marked by the dashed lines (not in scale). The other model parameters: $A = 2$, $\omega = 0.1$, $V_{12} = 4$, $V_{sd} = 0$, $\Gamma_N = 0.2$, $\Gamma_S = 1$, $U = 0$ [134].

Fig. 5.13b displays the influence of electron correlations. With increasing U, we observe the suppressed amplitude of the current. However, the details of the oscillations remain still visible.

Studying the periodically perturbed double quantum dot heterostructure we now consider different profiles of the drive. Fig. 5.14 presents the time-dependent current $j_{S\sigma}(t)$ imposed by the periodically driven energy levels $\varepsilon_{i\sigma}(t) = \varepsilon_{i\sigma}(t+T)$. In each plot, we included the corresponding driving profile marked by dashed lines (the amplitude is not in scale). Moreover, we assumed the same amplitudes and frequencies. For the step-like variations of the quantum dot's energy level, we observe the enhancement of the current after each change of $\varepsilon_{i\sigma}$. Those oscillations are damped in time and their lifetime is smaller than the period of the drive. For more smooth profiles of $\varepsilon_{i\sigma}$ the amplitude of the revival oscillations decreases and the current characteristics are correlated with the current plot for sinusoidal changes of the quantum

dot's energy level.

In the periodically driven system, we can calculate the averaged quantities over one driving period, e.g., current and differential conductance. This has been done for one single quantum dot system in Sec. 4.3 using the Green's function method. The observable averaged over one driving period gives more precise information about the role of the amplitude A and frequency ω of the oscillating quantum dot's energy level. Here, we use the Heisenberg equation of motion method, inspecting the charge currents averaged over a single period $T = 2\pi/\omega$ of the perturbation and we analyse the quasiparticle features visible in the nonequilibrium transport properties of the investigated heterostructure. We calculate the Andreev current average over one driving period $\langle j_{N\sigma}(t)\rangle_{t_0} = \frac{1}{T}\int_{t_0}^{t_0+T} j_{N\sigma}(t)dt$ and its differential conductance $G_{N\sigma}(V_{sd}) = \frac{d}{dV_{sd}}\langle j_{N\sigma}(t)\rangle_{t_0}$ with respect to the source-drain voltage V_{sd} and driving amplitude A or frequency ω.

Till $t \leq 0$ we assume both quantum dots to be empty and (at $t > 0$) impose the driving on $\varepsilon_{i\sigma}$ simultaneously with applying the voltage $V_{sd} = \mu_N - \mu_S$. The time-dependent evolution of the currents is presented in Fig. 5.13, where we observe the oscillations due to the driving force. In a long time evolution, the current becomes nearly periodic in time, therefore we can calculate its average value. It is important to notice that the period of the drive and the period of the currents become the same in the long time limit. In Fig. 5.15 we present the numerical results of the differential conductance $G_{N\sigma}(V_{sd}, \omega)$ for the set of the model parameters, where $\Gamma_N \ll \Gamma_S$ and $\varepsilon_d = 0$. The maps present the averaged Andreev conductance obtained for two values of the interdot coupling V_{12} and several amplitudes A, as indicated. Panels in Fig. 5.15 display the characteristic features of the driven quantum system originating from the absorption/emission of the external field quanta. In general, we notice the main quasiparticle peaks appearing at $\pm\frac{1}{2}\left(\sqrt{4V_{12}^2 + \Gamma_S^2/4} \pm \Gamma_S/2\right)$ and their higher harmonic peaks. Moreover, the avoided crossing behaviour between the peaks of different harmonic levels can be noticed.

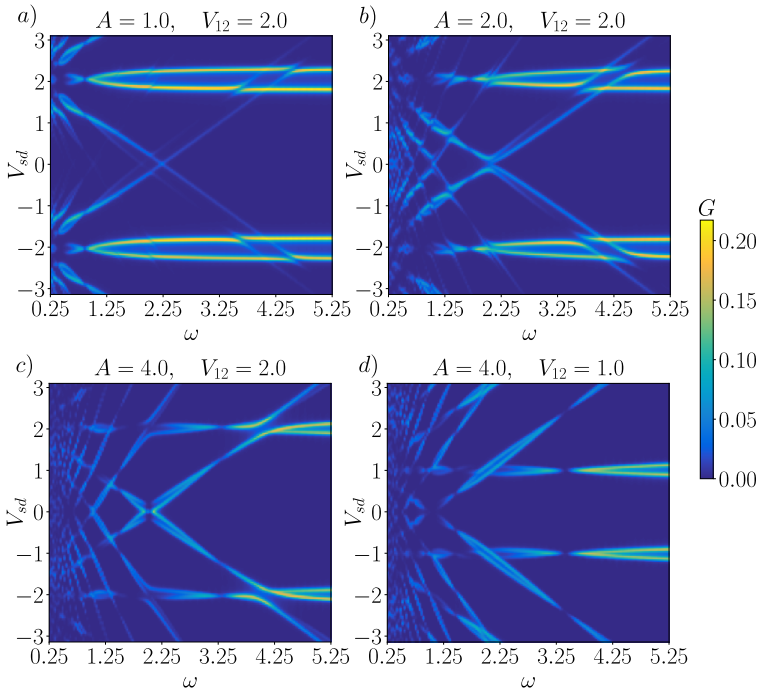

Figure 5.15: The averaged over one driving period Andreev conductance $G_{N\sigma}$ (in units of $2e^2/h$) as a function of frequency ω and the source-drain voltage V_{sd}. The results obtained for several amplitudes A and interdot coupling V_{12} (as indicated). The other model parameters: $\Gamma_N = 0.1$, $\Gamma_S = 1$, $U = 0$ [134].

Some properties of the photon-assisted tunnelling through the quantum dots placed between the normal electrodes have been previously studied in literature [144–146]. For such system, the main resonance peaks and harmonic bands are modulated by the square of the Bessel functions of the first kind $J_n^2(A/\omega)$ (see Fig. 4.3). In the Josephson junction, where the single quantum dot is embedded between two superconducting leads, the quasiparticle peaks are proportional to the following Bessel function $J_n^2(2A/\omega)$ [69, 147]. Here, the argument is doubled due to the fact that the Cooper pairs are the charge current carriers.

In our N-DQD-S heterostructure, we observe that the harmonic peaks are weighted by the squared Bessel function $J_0^2(2A/\omega)$. For the constant

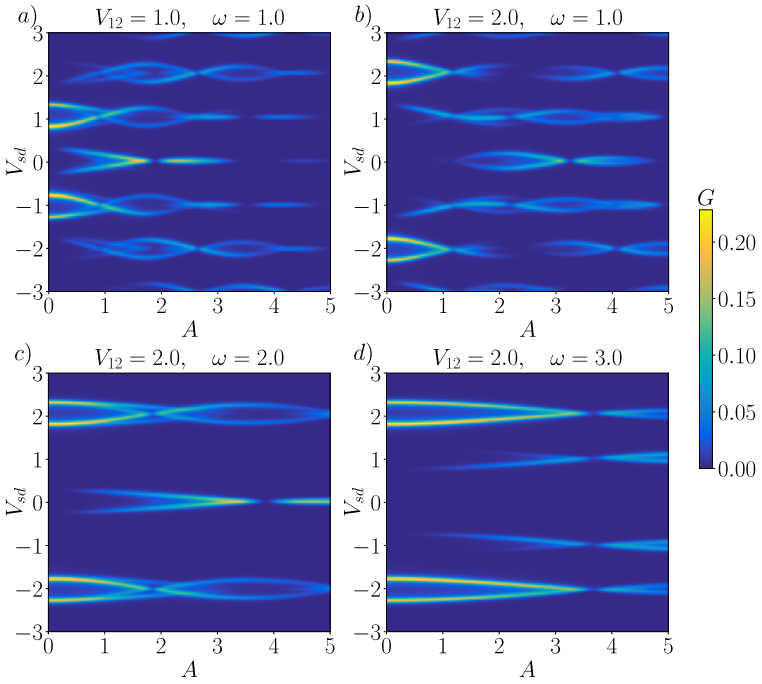

Figure 5.16: $G_{N\sigma}$ (in units of $2e^2/h$) averaged over one driving period Andreev conductance as a function of the amplitude A and the source-drain voltage V_{sd}. The results are obtained for several frequencies ω and interdot coupling V_{12} (as indicated), using: $\Gamma_N = 0.1$, $\Gamma_S = 1$, $U = 0$ [134].

amplitude $A = 4$ (see Fig. 5.15d), the quasiparticle peaks disappear at frequencies ω for which the Bessel function is equal to zero, e.g. $\omega \sim 3.3$, 1.45, 0.92. They correspond to the first, second and third zero of $J_0(2A/\omega)$, respectively. Moreover, comparing Figs.5.15c and 5.15d, we see that the value of ω for which the main quasiparticle peaks and higher harmonics disappear is independent of the interdot coupling V_{12}.

To investigate the influence of the amplitude on the quasiparticle spectrum, we calculated the averaged Andreev conductance with respect to V_{sd} and A, for a few values of the interdot coupling V_{12} and frequency ω (see Fig. 5.16). In the stationary situation, for $A = 0$, there exist four peaks in the differential conductance. Upon increasing the driving power, the main quasiparticle peaks

loose part of the spectral weights (intensity) at expense of the higher order replicas. With the growing amplitude, the larger number of replicas can be detected at energies ω, $\pm\omega$, $\pm 2\omega$. Simultaneously, their total spectral weight undergoes substantial redistribution. Besides this tendency, for specific values of A, the spectral weight of individual harmonics vanishes and then again reappears.

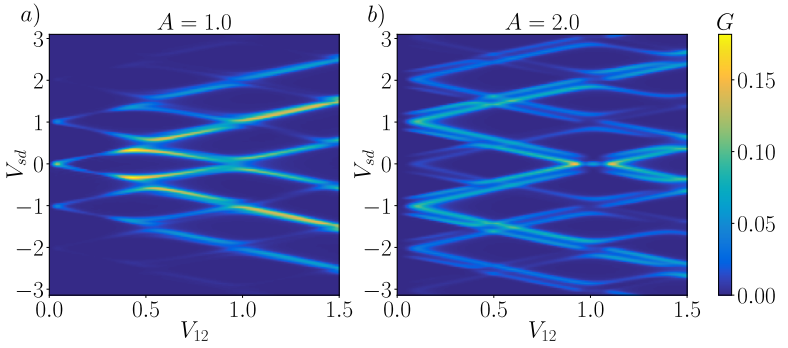

Figure 5.17: The averaged Andreev conductance $G_{N\sigma}$ (in units of $2e^2/h$) as a function of the interdot coupling V_{12} and the source-drain voltage V_{sd}. The results are obtained for several amplitudes A (as indicated), using the model parameters: $\omega = 1$, $\Gamma_N = 0.1$, $\Gamma_S = 1$, $U = 0$ [134].

Fig. 5.17 presents the plots of averaged Andreev conductance against the source-drain voltage V_{sd} and the interdot coupling V_{12}, obtained for two values of the driving amplitude A and frequency $\omega = 1$. The left panel in Fig. 5.17 presents the quasiparticle peaks appearing around $\pm n\omega$. Upon increasing the coupling V_{12} the peaks gradually split into the lower and upper branches. The branches of conductance peaks never cross each other because of the quantum mechanical interference [148]. In the case with the larger driving power (right panel in Fig. 5.17), we also observe this avoided crossing behaviour. Moreover, the harmonics consist of two nearby located peaks.

Finally, we investigate the influence of the electron correlation on the differential conductance $G_{N\sigma}$. Fig. 5.18 shows the results for $G_{N\sigma}$ as a function of the source-drain voltage V_{sd} calculated for several values of the

Coulomb repulsion force U and the following set of parameters: $V_{12} = 2$, $A = 2$ and $\omega = 2.5$. In comparison to the first plot presented in Fig. 5.18 (for uncorrelated case), we observe two doubled main quasiparticle peaks localized at $V_{sd} = \pm E^{\pm} \equiv \pm\frac{1}{2}\left(\sqrt{4V_{12}^2 + \Gamma_S^2/4} \pm \Gamma_S/2\right)$. We observe the first-order harmonics at $V_{sd} = \pm E^{\pm} \mp \hbar\omega$ and the peaks from the second-order harmonics localized at $V_{sd} = \pm E^{+} \mp 2\hbar\omega$. For larger electron correlation, the quasiparticle peaks change their heights. Upon increasing U, we observe more asymmetric distribution among the second-order harmonics as compared to the first-order harmonics, which have nearly symmetric shape. Position of the quasiparticle peaks are nearly insusceptible to the electron correlations.

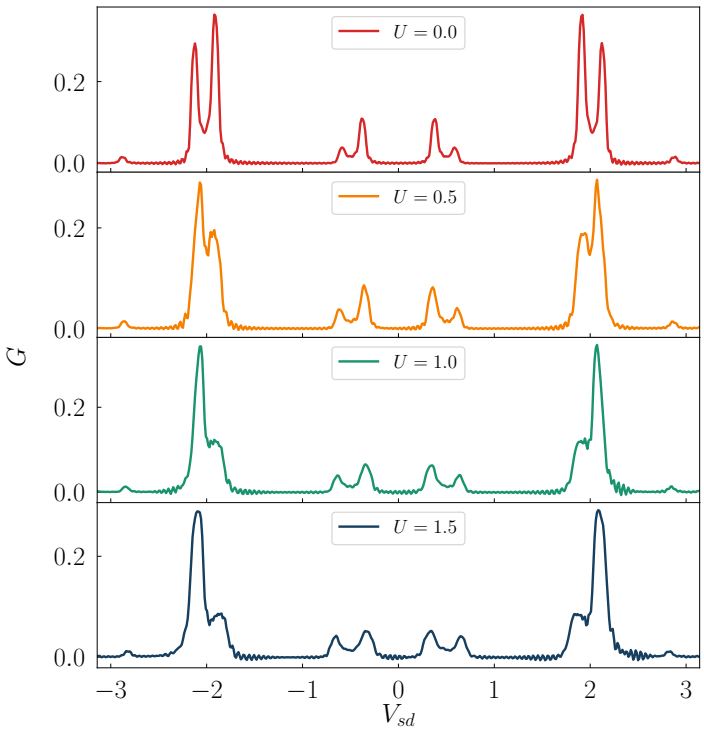

Figure 5.18: The averaged Andreev conductance $G = G_{N\sigma}$ (in units of $2e^2/h$) as a function of the source-drain voltage V_{sd}. The results obtained within mean-field approximation for several values of U (as indicated), using: $V_{12} = 2$, $\omega = 2.5$, $\Gamma_N = 0.1$, $\Gamma_S = 1$ [134].

5.7 Summary

In this chapter, we discussed the transient effects and the post-quench dynamics of the double quantum dot system. We presented that the transient effects are characterized by damped quantum oscillations with the exponential envelope function $e^{-t\Gamma_N/2}$. The period of these quantum oscillation coincides with energies of the in-gap states for the system.

The post-quench evolution induced by jump of the source-drain voltage has shown that the quantum oscillations are the superposition of the sinusoidal waves $\sum_{i=1}^{4} a_i e^{-\lambda_i t}\sin(\Omega_i t)$, with adequate frequencies $\Omega_{1/2} = V_{sd} \pm \omega_1$ and $\Omega_{3/4} = V_{sd} \pm \omega_2$, where $\omega_{1/2} = V_{12} \pm \Gamma_S/4$. For the large source-drain voltage $|V_{sd}| \gg V_{12}$, the beating pattern depends on the ratio $r = 4V_{12}/\Gamma_S$.

We also analysed evolution of the system after the sudden shift of the quantum dot energy levels. We noticed, that the evolution of the system after the quench mostly depends on the initial occupations $n_{i\sigma}$ (right before the quench) and the magnitude of gate potential V_g. For the energy shifts which coincide with the plateau and slope regions presented in Fig. 5.9 (plot of the charge vs. energy level of quantum dots) some universal properties of the oscillations can be detected.

In the last part we presented the results for the system influenced by the periodic driving of the quantum dot energy levels. The oscillations of the time-dependent currents are induced when the amplitude of the drive is close or exceeds the value of the coupling V_{12}. We noticed that for stronger correlations the amplitude of the oscillations decreases, but the characteristic shape of currents remains unchanged. We also presented the conductance averaged over one driving period. Such conductance is characterized by the main quasiparticle peaks appearing at $\pm\frac{1}{2}\left(\sqrt{4V_{12}^2 + \Gamma_S^2/4} \pm \Gamma_S/2\right)$ and emergence of the higher harmonic peaks caused by the emission/absorption of the energy quanta. The correlations affect the distribution of the quasiparticle peaks, mainly by their height (spectral weight). Position of the quasiparticle peaks weakly affected by the electron correlations.

Chapter 6

Machine learning simulations

In this chapter we discuss a computational method of a machine learning (ML) [149, 150] applied in our study to investigation of the driven systems. Considering the double quantum dot system, the numerical solution of the Heisenberg equation of motion consumes a large amount of computational power and time. Our numerical procedure has been parallelized which greatly increased the effectiveness of our code. However, to obtain a single map of the averaged conductance over one driving period using CPU 2x Xeon E5-2660 (2.2GHz 16 cores/ 32 threads) took almost one week of calculations. To avoid such difficulties an auxiliary procedure based on a machine learning algorithm has been developed.

In this section the concept, main principles and structure of the machine learning algorithm will be introduced. For brevity we present here only the most important details.

6.1 Fundamentals of artificial intelligence

In general, the machine learning is a numerical method of data analysis. The purpose of the machine learning is to expose patterns and correlations between the particular variables of the investigated case. The idea of the machine learning algorithm has been presented in 1959 by Arthur Samuel [149],

who was the pioneer in an artificial intelligence (AI) field. The machine learning is a subfield of the artificial intelligence, which can be regarded as a simulation of the human mind. The main purpose of the artificial intelligence is to mimic humans actions, and program machines to behave like humans. Those simulations can be applied to learn and solve some specific problems.

The artificial intelligence is based on an artificial neural network, which is composed of the single nodes called perceptron (see Fig. 6.1). Moreover, the idea of preceptron is based on the working principles of the neuron. In general, the preceptron can have any number of inputs and outputs, which are represented by numerical values. Every input is multiplied by a corresponding

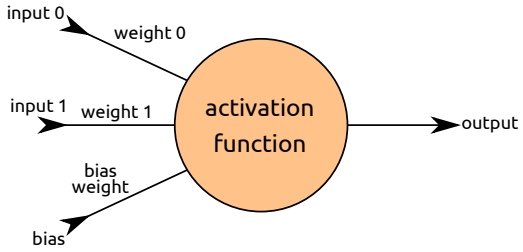

Figure 6.1: Idea of the perceptron.

weight. Then the result of the multiplication is passed to an activation function and finally, in the output, the specific result is obtained. Sometimes, the activation function requires additional bias value. It happens when the sum of inputs does not fulfil the properties of the activation function. For example: *The perceptron returns 1 if the sum of inputs is positive number or 0 if the sum of inputs is negative number.* The problem occurs if the original input is zero. Then an addition of the extra bias value equal $+1$ solves the problem. Mathematically, the concept of the perceptron can be pressented by a simple sum $\sum_{i=0}^{N} w_i x_i + b$, where N denotes number of inputs, w_i is the weight corresponding to the specific input x_i and b is the bias value.

A larger number of perceptrons can create the matrix form that is the neural network, schematically presented in Fig. 6.2. The particular parts of the neural network can be specified: input layer, hidden layer, output layer.

The input layer consists of the perceptrons whose number usually corresponds

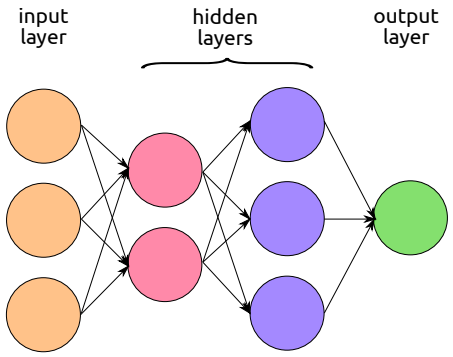

Figure 6.2: Graph of the artificial network.

to the number of features or properties of the considered case. In the center of the neural network, the hidden layers are located. The number of the hidden layers and the number of nodes in the specific layer is an arbitrary value. Often the hidden layers are called the level of abstraction because their outputs do not represent any physical value. At the end of the neural network, the output layer is located. The final layer returns the predicted value of the formed model.

In the model, besides the number of layers and nodes, a crucial role plays the activation function. Depending on the task, the appropriate activation function must be applied. If we consider a classification problem then the logic function will be the appropriate choice. For more complex cases the more dynamic functions will be better. The most common functions having good performance are: Sigmoid function - $S(x) = (1 + e^{-x})^{-1}$, Hyperbolic Tangent - $\tanh(x)$, Rectified Linear Unit (ReLU) $f(x) = x^+ = \max(0, x)$.

6.2 Basics and functions of the learning protocols

To grasp the idea of the learning process, some particular information needs to be presented. First of all, let us consider the case of the single perceptron and its predictions.

For random weights, the output of the perceptron and the expected value are inconsistent. Adjustment of the perceptron weights is called the learning process. To measure the discrepancy between predicted value and the expected value we can use a cost function. The cost function C evaluates the performance of the neuron that is measured by how far off the predictions x are from the true value y. One of the most common function is a *quadratic cost* $C = \sum_{i=0}^{N}(y_i - x_i)^2/N$, which is not an efficient function and could increase the time of the learning process. For this cost function, the larger errors are more pronounced due to the squaring. Another, more efficient cost function is a *cross entropy* $C = -\frac{1}{N}\sum_{i=0}^{N}[y_i \ln(x_i) + (1 - y_i)\ln(1 - x_i)]$. The *cross entropy* allows for a much faster learning process because the larger the difference, the faster the perceptron can learn. The cost functions are indirectly dependent on the perceptron weights.

A subsequent important aspect of the learning process is a *gradient descent* (the delta rule). The *gradient descent* is an algorithm for finding the minimum of the cost function C, schematically presented in Fig. 6.3. As we see in

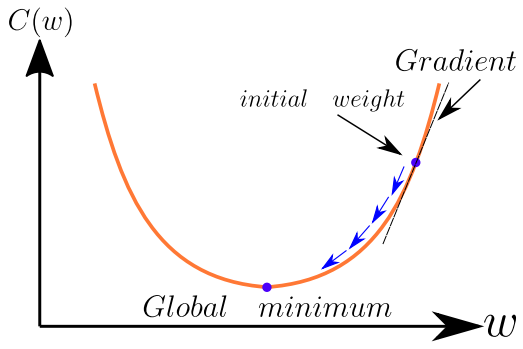

Figure 6.3: Visualization of the gradient descent algorithm.

Fig. 6.3 there exists a value of weight w which for the cost function $C(w)$ has its minimum. The *gradient descent algorithm* is based on an iteration process. The algorithm starts with a random set of perceptron weights and calculates the error for each next step of the iteration, updating the model parameters until the result is the minimum of the cost function. This process

has following pseudocode structure

$$\textbf{while:} \quad C(w_i) \neq \min[C(w)] \quad \{ \\ w_i = w_i - \alpha \frac{\partial C(w_i)}{\partial w_i} \quad \},$$

where α denotes a learning rate. The learning rate define how quickly the *gradient descent algorithm* moves towards the minimum of the cost function. Inappropriate value of the learning rate negatively affects the *gradient descent algorithm*, if α is too small the algorithm makes small steps that extend calculation time. On the other hand, if α is too large the algorithm can overshoot and do not find the solution. One can specify three types of the *gradient descent algorithm*:

- Batch gradient descent - all of the training data is considered by an algorithm to make a single step. The algorithm takes the average of the gradients of all the training points and then uses that mean gradient to update the perceptron weights. One step of gradient descent is called one epoch.

- Mini-batch gradient descent - the algorithm takes small portion of the training data called batch. The batch is used to update the perceptron weights in each iteration.

- Stochastic gradient descent - updates the perceptron weights in each iteration using only a randomly selected single batch from the training data set.

In more complex cases, when the neural network is considered, the larger number of perceptrons and their weights are needed to figure out the solution. To adjust the values for the perceptron weights and minimize the cost function across our entire network by the *gradient descent algorithm* we need to use a *backpropagation*. The *backpropagation algorithm* is a generalization of the *gradient descent algorithm* for the artificial neural network. Such an

algorithm calculates the gradient of the error function with respect to the neural network's weights. The calculations proceed backwards through the neural network. At first, the algorithm calculates the gradient of the loss function for the final layer, then going back calculates the gradient of the loss function using the weights of the subsequent layers up to the first layer. The *backpropagation algorithm* is an algorithm for a supervised learning. Supervised learning is one of the types of machine learning, it uses the labeled data sets to model dependencies between the target predictions and the input features.

The learning protocol is a combination of the particular procedures presented above, schematically visualized in Fig. 6.4. To train the neural network

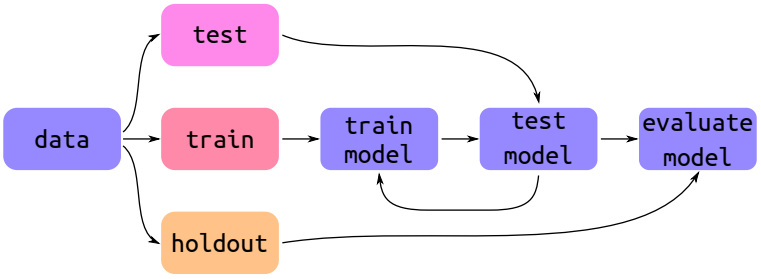

Figure 6.4: Scheme of the learning protocol for the artificial neural network.

we require a prepared dataset, which will be divided into three subsets: train, test, holdout. The train subset contains the data for the training process, which teaches our neural network by using the *gradient descent* and *backpropagation* algorithms. Then the efficiency of the established neural network is checked by data from the test subset. If the predictions of the model are not convergent to the true values the training procedure will be performed again. The final correctness of the neural network is verified by the holdout subset.

6.3 Adaptation of artificial intelligence to the driven double quantum dot system

In our specific case of N-DQD-S heterostructure, we train the neural network using supervised learning and the mini-batch gradient descent. Our data set is a compound of 76 conductance maps. The maps of the conductance averaged over single driving period have different resolutions and in total give 971760 data points. To increase the number of points, every map has been linearly interpolated, giving us 3887040 data points in total. As software we choose Tensorflow, the open-source machine learning library having an integrated programming interface Keras [151].

In the model of the densely connected neural network (see Fig. 6.5), we have four parameters in the intake layer (V_{12}, ω, V_{sd}, A) and the output layer with the single neuron (G), where the hidden layers are composed of the layers consisted of 2048, 1024, 512, and 256 neurons, respectively. The size

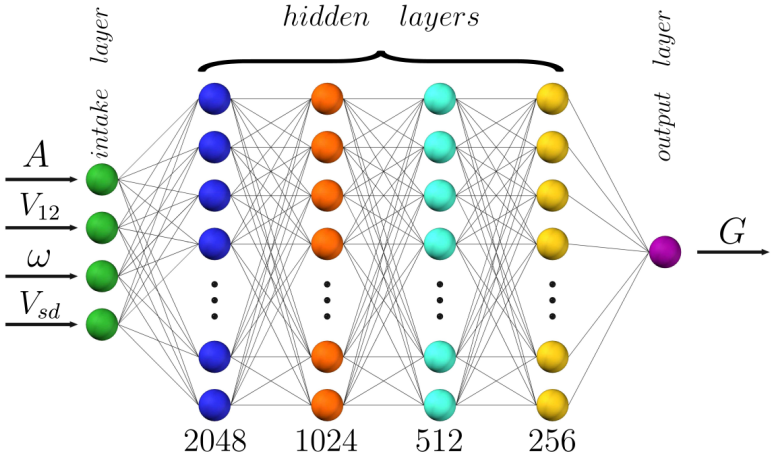

Figure 6.5: The densely connected artificial neural network.

of the neural network is caused by the nonlinearity in the system. Every single neuron has the sigmoid function as the activation function. To avoid overfitting of the model we defined a dropout of 1% neurons on every learning step. In the training process, we established the batch size 1024 and the

number of epochs equal 600, which gave us the fidelity coefficient $R^2 = 0.987$.

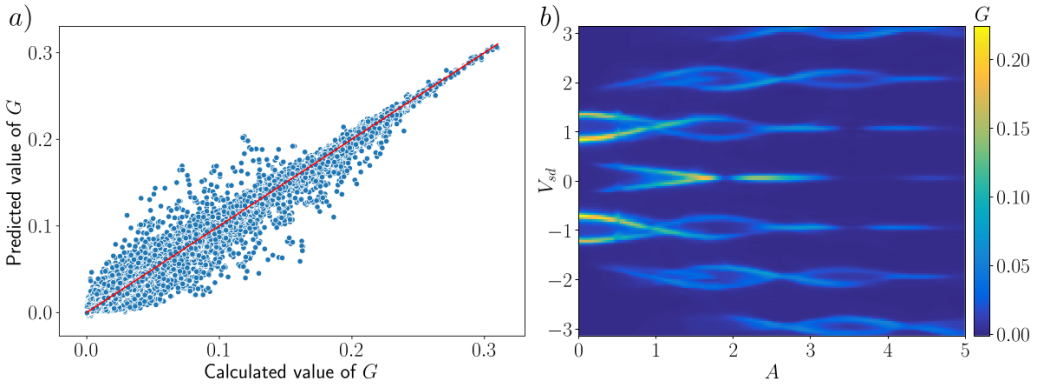

Figure 6.6: a) The plot of the differential conductance predicted by the neural network versus calculated values. b) The reconstruction of the conductance map in Fig. 5.16a generated by the neural network [134].

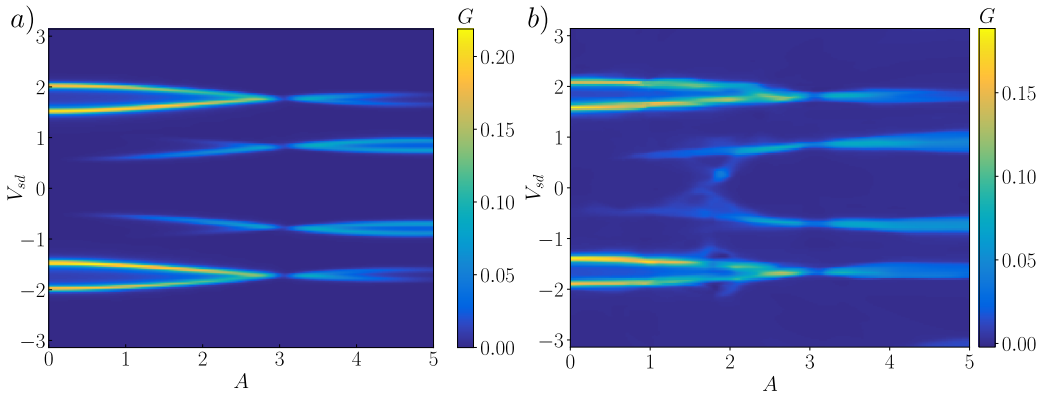

Figure 6.7: The calculated conductance map (panel a) and generated by the neural network (panel b) obtained for $V_{12} = 1.7$, $\omega = 2.5$ [134].

Fig. 6.6a shows the discrepancies between the calculated and predicted values of G for our model, which is deflation of the points from the red line. Fig. 6.6b presents a reconstruction of the conductance map for specific system parameters, which has been included in the train data subset. For comparison, panels in Fig. 6.7 show the conductance maps obtained from the direct calculation (panel a) and by the neural network (panel b). The

map shown in panel a) in Fig. 6.7 has not been used for learning the neural network. Those results have been published in [134].

In Fig. 6.7, we see the qualitative reconstruction of the calculated by equation of motion method conductance map. With this approach, we are able to simulate new conductance maps for a periodically driven double quantum dot system and many different values of the controlling parameters. Recalling that we can control: source-drain bias voltage V_{sd}, amplitude A and frequency ω of driving field and the strength of interdot coupling V_{12}. The analysis and properties of these maps are discussed in Chapter 5.6. The machine learning model of the double quantum dot system allows us to simulate the same conductance map faster. We have managed to reduce the calculation time to less than an hour, where calculations using the equation of motion method required more than a week.

This neural network model is available at the following webpage:
`www.dropbox.com/sh/0hzs9im3d3bf0jr/AADRr3kltw2m0dCCh8tedoIWa?dl=0`

Chapter 7

Summary and Outlook

This dissertation presented a study of the superconducting nanostructures and their time-dependent properties. We have investigated the systems composed of the single and double quantum dots embedded between the normal metallic and superconducting leads. We have inspected response of such systems on various dynamical perturbations, i.e.: transient effects (sudden coupling of the quantum dots to the reservoirs), abrupt application of the source-drain voltage, quench in the quantum dot energy level, sudden change of the coupling to the superconductive electrode. Moreover, we have analysed the evolution of the system under the periodic driving of the energy level of the quantum dots. Variety of the protocols has resulted in a plethora of emergent physical phenomena. Here, we briefly recollect the most important findings.

Single quantum dot

For the single quantum dot system, placed between the normal metal and superconducting electrode, we observed the time-dependent emergence of the Andreev states. Formation of the bound states in the quantum dot at energies $E_A = \pm\sqrt{(\varepsilon_d + U/2)^2 + (\Gamma_S/2)^2}$ has an oscillating character, with period $2\pi/E_A$ and the relaxation processes are governed by envelope function $e^{-\Gamma_N t}$.

After the rapid switching the source-drain bias voltage in the uncorrelated quantum dot system, we also observed the oscillations of the charge current. Those oscillations resulted from the superposition of two contributing currents with the

frequencies $\omega_{1/2} = \mu_N \pm \Gamma_S/2$. We noticed that the current to normal lead $j_{N\sigma}(t)$ is consisted of the high frequency component $\omega = \mu$ and the low frequency one with the time period $T = 2\pi/\Gamma_S$, whereas the current $j_{S\sigma}(t)$ revealed oscillations with only the lower frequency.

In the post-quench evolution of uncorrelated system (imposed by variation of the quantum dot energy), the oscillatory behaviour of the observables revealed the period $T = 2\pi/\sqrt{\Gamma_S^2 + 4(\Delta\varepsilon_d)^2}$. For the correlated quantum dot system, we discovered the phenomenon resembling the $0-\pi$ transition, sign-reversal of the oscillating observables. Investigating the influence of the suddenly changed coupling to the superconducting electrode, we observed the transition from the doublet to singlet configurations.

For the uncorrelated system we found that the periodical driving field induced the harmonic states in the quasiparticle spectrum. Such harmonic states emerged from the Andreev states and showed up in the differential conductivity of N-QD-S heterostructure. We also noticed that the harmonic states linearly depend on the driving frequency and they split due to the superconducting proximity effect.

Double quantum dot

For the double quantum dot system placed in series between the normal metal and superconducting electrode, we observed the time-dependent formation of the Andreev states appearing in the differential conductance at $E = \pm\frac{1}{2}\left(\sqrt{4V_{12}^2 + \Gamma_S^2/4} \pm \Gamma_S/2\right)$ (for $\varepsilon_{i\sigma} = 0$).

In the post-quench evolution induced by the source-drain voltage, we noticed emergence of the quantum beats with the time period $T_B = \pi/V_{12}$. The appearance of the quantum beats is due to the superposition of waves of different frequencies. The total current can be represented as a superposition of sinusoidal waves $\sum_{i=1}^{4} a_i e^{-\lambda_i t}\sin(\Omega_i t)$, with frequencies $\Omega_{1/2} = V_{sd} \pm \omega_1$ and $\Omega_{3/4} = V_{sd} \pm \omega_2$, where $\omega_{1/2} = V_{12} \pm \Gamma_S/4$. For the correlated case at the electron-hole symmetry point $\varepsilon_{i\sigma} = -U/2$, we observed similar behaviour of the observables.

Subsequently, we investigated the quenches imposed on the quantum dot energy levels $\varepsilon_{i\sigma}$. We established the protocol, consisting of the first ($\varepsilon_{i\sigma} \to \varepsilon_{i\sigma} + V_g$) and the second quench ($\varepsilon_{i\sigma} + V_g \to \varepsilon_{i\sigma}$) for $\varepsilon_{i\sigma} = 0$. After the first quench, for $V_g < V_{12}$,

we observed the damped oscillations in the characteristics of observables and almost unchanged occupancies of both QDs. For $V_g \sim V_{12}$, we observed more pronounced oscillations with the period $T = 2\pi/\Gamma_S$ and variation of the occupancy of quantum dots. In the evolution, after the second quench, for $V_g \sim V_{12}$, the fluctuations were more pronounced. We observed the oscillations with period $T = \pi/V_{12}$ and the beating structure with the period $T_B = 2\pi/\Gamma_S$. For $V_g > V_{12}$, the evolution after the second quench revealed the oscillations with the period $T = 2\pi/\Gamma_S$ without the beating structure. The post-quench dynamics proved to be strictly dependent on the ratio between V_g and V_{12}. For the correlated case, at half-filling $\varepsilon_{i\sigma} = -U/2$, we observed similar behaviour of the observables.

Additionally, for the double quantum dot system with the periodic driving, we found appearance of the harmonic peaks weighted by the squared Bessel function $J_0^2(2A/\omega)$. They originated from the Andreev bound states and evolved depending on the amplitude and the frequency of the driving field. These branches of conductance peaks never cross each other. For investigating the emergence of the harmonic peaks we constructed the machine learning model (discussed in Ch. 6).

Outlook

In the future studies, we would like to investigate Majorana modes in systems with the periodic driving. In our opinion, the Majorana modes should have a impact on the conductance map of the system with the single or double quantum dot. In multi-terminal systems with the side-attached Majorana wire [152, 153], the dynamics induced by the different types of quench protocols would be worth addressing as well. Additionally, it would be interesting to explore the influence of strong electron correlations on the post-quench dynamics of states in the double quantum dot.

Furthermore, it would be worthwhile to investigate the dynamics of quantum dot arrays connected to superconducting reservoirs, and analyse their evolution induced by different types of perturbations. Another issue for investigation could be the time-dependent entanglement between quasiparticles in heterostructures with the topological superconductors.

Appendix A

A.1 Differential equations of motion for N-QD-S

Solving the Heisenberg equation of motion for N-QD-S Hamiltonian we get the closed set of equations:

$$d_t f_1 \equiv d_t\langle n_{d\uparrow}(t)\rangle = 2\mathrm{Im}\left[\sum_k V_k e^{-i\varepsilon_{Nk}t} f_{k1} - i\frac{\Gamma_N}{2} f_1 - \Delta_{sc} f_3\right], \tag{A.1}$$

$$d_t f_2 \equiv d_t\langle n_{d\downarrow}(t)\rangle = 2\mathrm{Im}\left[\sum_k V_k e^{-i\varepsilon_{Nk}t} f_{k2} - i\frac{\Gamma_N}{2} f_2 - \Delta_{sc} f_3\right], \tag{A.2}$$

$$\begin{aligned} d_t f_3 \equiv d_t\langle d_\downarrow(t) d_\uparrow(t)\rangle &= -i\left(\varepsilon_{d\uparrow}(t) + \varepsilon_{d\downarrow}(t) - i\Gamma_N\right) f_3 - i\Delta_{sc}(1 - f_1 - f_2) \\ &\quad -i\sum_k V_k e^{-i\varepsilon_{Nk}t} f_{k4} + i\sum_k V_k e^{-i\varepsilon_{Nk}t} f_{k3}, \end{aligned} \tag{A.3}$$

$$\begin{aligned} d_t f_{k1} \equiv d_t\langle d_\uparrow^\dagger(t) c_{k\uparrow}(0)\rangle &= \left[i\varepsilon_{d\uparrow}(t) - \frac{\Gamma_N}{2}\right] f_{k1} + i\Delta_{sc} f_{k4} \\ &\quad + iV_k e^{i\varepsilon_{Nk}t}\bar{n}(\varepsilon_k), \end{aligned} \tag{A.4}$$

$$\begin{aligned} d_t f_{k2} \equiv d_t\langle d_\downarrow^\dagger(t) c_{k\downarrow}(0)\rangle &= \left[i\varepsilon_{d\downarrow}(t) - \frac{\Gamma_N}{2}\right] f_{k2} - i\Delta_{sc} f_{k3} \\ &\quad + iV_k e^{i\varepsilon_{Nk}t}\bar{n}(\varepsilon_k), \end{aligned} \tag{A.5}$$

$$d_t f_{k3} \equiv d_t\langle d_\uparrow(t) c_{k\downarrow}(0)\rangle = \left[-i\varepsilon_{d\uparrow}(t) - \frac{\Gamma_N}{2}\right] f_{k3} - i\Delta_{sc} f_{k2}, \tag{A.6}$$

$$d_t f_{k4} \equiv d_t\langle d_\downarrow(t) c_{k\uparrow}(0)\rangle = \left[-i\varepsilon_{d\downarrow}(t) - \frac{\Gamma_N}{2}\right] f_{k4} + i\Delta_{sc} f_{k1}, \tag{A.7}$$

where $\bar{n}(\varepsilon_k) = \left[1 + \exp\left((\varepsilon_k - \mu_N)/k_B T\right)\right]^{-1}$ is the Fermi distribution function of the normal lead electrons and $d_t \equiv \frac{d}{dt}$.

A.2 Differential equations of motion for N-DQD-S

The closed set of the differential equations corresponding to the N-DQD-S system Hamiltonian:

$$d_t f_1 \equiv d_t\langle n_{1\uparrow}(t)\rangle = 2\mathrm{Im}\left[V_{12} f_7 - \Delta_{sc} f_5\right], \tag{A.8}$$

$$d_t f_2 \equiv d_t\langle n_{1\downarrow}(t)\rangle = 2\mathrm{Im}\left[V_{12} f_8 - \Delta_{sc} f_5\right], \tag{A.9}$$

$$d_t f_3 \equiv d_t\langle n_{2\uparrow}(t)\rangle = 2\mathrm{Im}\left[\sum_k V_k e^{-i\varepsilon_k t} f_{k5} - i\frac{\Gamma_N}{2} f_3 - V_{12} f_7\right], \tag{A.10}$$

$$d_t f_4 \equiv d_t\langle n_{2\downarrow}(t)\rangle = 2\mathrm{Im}\left[\sum_k V_k e^{-i\varepsilon_k t} f_{k6} - i\frac{\Gamma_N}{2} f_4 - V_{12} f_8\right], \tag{A.11}$$

$$\begin{aligned} d_t f_5 \equiv d_t\langle d_{1\downarrow}(t) d_{1\uparrow}(t)\rangle &= -i\left[\varepsilon_{1\uparrow}(t) + \varepsilon_{2\downarrow}(t)\right] f_5 + iV_{12}\left[f_9 - f_{10}\right] \\ &\quad -i\Delta_{sc}\left[1 - f_1 - f_2\right], \end{aligned} \tag{A.12}$$

$$\begin{aligned} d_t f_6 \equiv d_t\langle d_{2\downarrow}(t) d_{2\uparrow}(t)\rangle &= -i\left[\varepsilon_{2\uparrow}(t) + \varepsilon_{2\downarrow}(t) - i\Gamma_N\right] f_6 + iV_{12}\left[f_9 - f_{10}\right] \\ &\quad +i\sum_k V_k e^{-i\varepsilon_k t}\left[f_{k7} - f_{k8}\right], \end{aligned} \tag{A.13}$$

$$\begin{aligned} d_t f_7 \equiv d_t\langle d^\dagger_{1\uparrow}(t) d_{2\uparrow}(t)\rangle &= i\left[\varepsilon_{1\uparrow}(t) - \varepsilon_{2\uparrow}(t) + \frac{i}{2}\Gamma_N\right] f_7 + iV_{12}\left(f_3 - f_1\right) + i\Delta_{sc} f_{10} \\ &\quad -i\sum_k V_k e^{-i\varepsilon_k t} f_{k1}, \end{aligned} \tag{A.14}$$

$$\begin{aligned} d_t f_8 \equiv d_t\langle d^\dagger_{1\downarrow}(t) d_{2\downarrow}(t)\rangle &= i\left[\varepsilon_{1\downarrow}(t) - \varepsilon_{2\downarrow}(t) + \frac{i}{2}\Gamma_N\right] f_8 + iV_{12}\left(f_4 - f_2\right) - i\Delta_{sc} f_9 \\ &\quad -i\sum_k V_k e^{-i\varepsilon_k t} f_{k2}, \end{aligned} \tag{A.15}$$

$$\begin{aligned} d_t f_9 \equiv d_t\langle d_{1\uparrow}(t) d_{2\downarrow}(t)\rangle &= -i\left[\varepsilon_{1\uparrow}(t) + \varepsilon_{2\downarrow}(t) - \frac{i}{2}\Gamma_N\right] f_9 + iV_{12}\left[f_5 + f_6\right] - i\Delta_{sc} f_8 \\ &\quad -i\sum_k V_k e^{-i\varepsilon_k t} f_{k3}, \end{aligned} \tag{A.16}$$

$$\begin{aligned} d_t f_{10} \equiv d_t\langle d_{1\downarrow}(t) d_{2\uparrow}(t)\rangle &= -i\left[\varepsilon_{1\downarrow}(t) + \varepsilon_{2\uparrow}(t) - \frac{i}{2}\Gamma_N\right] f_{10} - iV_{12}\left[f_5 + f_6\right] + i\Delta_{sc} f_7 \\ &\quad -i\sum_k V_k e^{-i\varepsilon_k t} f_{k4}, \end{aligned} \tag{A.17}$$

$$d_t f_{k1} \equiv d_t\langle d^\dagger_{1\uparrow}(t)c_{k\uparrow}(0)\rangle = i\varepsilon_{1\uparrow}(t)f_{k1} + iV_{12}f_{k5} + i\Delta_{sc}f_{k4}, \tag{A.18}$$

$$d_t f_{k2} \equiv d_t\langle d^\dagger_{1\downarrow}(t)c_{k\downarrow}(0)\rangle = i\varepsilon_{1\downarrow}(t)f_{k2} + iV_{12}f_{k6} - i\Delta_{sc}f_{k3}, \tag{A.19}$$

$$d_t f_{k3} \equiv d_t\langle d_{1\uparrow}(t)c_{k\downarrow}(0)\rangle = -i\varepsilon_{1\uparrow}(t)f_{k3} - iV_{12}f_{k7} - i\Delta_{sc}f_{k2}, \tag{A.20}$$

$$d_t f_{k4} \equiv d_t\langle d_{1\downarrow}(t)c_{k\uparrow}(0)\rangle = -i\varepsilon_{1\downarrow}(t)f_{k4} - iV_{12}f_{k8} + i\Delta_{sc}f_{k1}, \tag{A.21}$$

$$d_t f_{k5} \equiv d_t\langle d^\dagger_{2\uparrow}(t)c_{k\uparrow}(0)\rangle = i\left[\varepsilon_{2\uparrow}(t) + \frac{i}{2}\Gamma_N\right]f_{k5} + iV_{12}f_{k1} \tag{A.22}$$

$$+iV_k e^{i\varepsilon_k t}\bar{n}(\varepsilon_k), \tag{A.23}$$

$$d_t f_{k6} \equiv d_t\langle d^\dagger_{2\downarrow}(t)c_{k\downarrow}(0)\rangle = i\left[\varepsilon_{2\downarrow}(t) + \frac{i}{2}\Gamma_N\right]f_{k6} + iV_{12}f_{k2} \tag{A.24}$$

$$+iV_k e^{i\varepsilon_k t}\bar{n}(\varepsilon_k), \tag{A.25}$$

$$d_t f_{k7} \equiv d_t\langle d_{2\uparrow}(t)c_{k\downarrow}(0)\rangle = -i\left[\varepsilon_{2\uparrow}(t) - \frac{i}{2}\Gamma_N\right]f_{k7} - iV_{12}f_{k3}, \tag{A.26}$$

$$d_t f_{k8} \equiv d_t\langle d_{2\downarrow}(t)c_{k\uparrow}(0)\rangle = -i\left[\varepsilon_{2\downarrow}(t) - \frac{i}{2}\Gamma_N\right]f_{k8} - iV_{12}f_{k4}. \tag{A.27}$$

Such systems of differential equations can be solved by iterative methods. In our investigation, we applied Runge-Kutta 4th order method. However, other and faster numerical methods, e.g. Dormand–Prince, can be implemented.

A.3 Non-equilibrium Green's function formalism

In quantum physics the many-body system can be governed by time dependent Hamiltonian $\hat{H}(t)$. The idea of adiabatic switching relies on assumption that in the past $t = -\infty$ the system was in initial state defined by the many-body density matrix $\rho(-\infty)$ and from that point evolves according to the Heisenberg equation of motion $\frac{d}{dt}\rho(t) = -\frac{i}{\hbar}[\hat{H}(t), \rho(t)]$. For $\hbar = 1$ the formal solution is represented by the initial state and the evolution operators $\rho(t) = \hat{U}(t, -\infty)\rho(-\infty)\hat{U}^\dagger(t, -\infty)$, where the operators are defined as follows

$$\hat{U}(t, t') = Te^{-i\int_{t'}^{t}\hat{H}(\tau)d\tau} = \lim_{N\to\infty} e^{-i\hat{H}(t)\delta t}e^{-i\hat{H}(t-\delta t)\delta t}\dots e^{-i\hat{H}(t'+\delta t)\delta t} \tag{A.28}$$

and $\delta t = (t - t')/N$ denotes the infinitesimal time step. The expectation value of observable $\hat{\mathcal{O}}$ for the system at specific time t is defined as

$$\langle\hat{\mathcal{O}}(t)\rangle \equiv \frac{\mathrm{Tr}\{\hat{\mathcal{O}}\rho(t)\}}{\mathrm{Tr}\{\rho(t)\}} = \frac{\mathrm{Tr}\{\hat{U}(-\infty, t)\hat{\mathcal{O}}\hat{U}(t, -\infty)\rho(-\infty)\}}{\mathrm{Tr}\{\rho(t)\}}, \tag{A.29}$$

where the trace is performed over the Hilbert space of many-body Hamiltonian [154–156]. The numerator of the fraction includes the time evolution operator describing the system evolution from $t = -\infty$ to time t and backward to $t = -\infty$.

The zero temperature expectation value of the operator $\hat{\mathcal{O}}$ in equilibrium is defined as $\langle \mathcal{GS}|\hat{\mathcal{O}}|\mathcal{GS}\rangle = \langle 0|\hat{U}(-\infty, t)\hat{\mathcal{O}}\hat{U}(t, -\infty)|0\rangle$, where $|\mathcal{GS}\rangle = \hat{U}(t, -\infty)|0\rangle$ is a ground state of the interacting system and $|0\rangle$ denotes a vacuum [157]. The evolution operators describe the evolution of the non-interacting vacuum state $|0\rangle$ toward the ground state $|\mathcal{GS}\rangle$ through the adiabatic activation of interactions. It is claimed that the adiabatic evolution of the system along the entire contour and back to the starting point results in an additional phase factor $\langle 0|\hat{U}(+\infty, -\infty) = \langle 0|e^{iL}$. To compensate the phase factor in the definition of the expectation value for operator we can divide by this term $\langle \mathcal{GS}|\hat{\mathcal{O}}|\mathcal{GS}\rangle = \langle 0|\hat{U}(+\infty, t)\hat{\mathcal{O}}\hat{U}(t, -\infty)|0\rangle / e^{iL}$, then the evolution describes only the forward path without backward segment.

This approach does not work in nonequilibrium situations. For the case, when the system was driven out of equilibrium, the final state depends on the switching protocol and the entire evolution of the system. The final state does not have to be the same as the initial state. To avoid the needed of knowing state of the system at $t = +\infty$, we can use the Schwinger approach [158]. The evolution of (A.29) can be extended from t to $t = \infty$ and backward by substituting $\hat{U}(t, +\infty)\hat{U}(+\infty, t) = 1$ and written as

$$\langle \hat{\mathcal{O}}(t)\rangle = \frac{\mathrm{Tr}\{\hat{U}(-\infty, +\infty)\hat{U}(+\infty, t)\hat{\mathcal{O}}\hat{U}(t, -\infty)\rho(-\infty)\}}{\mathrm{Tr}\{\rho(-\infty)\}}, \tag{A.30}$$

which is the evolution along the closed time contour C. In temperature limit $T \to 0$, those two branches of the time evolution are depicted by the Keldysh contour in Fig. A.1.

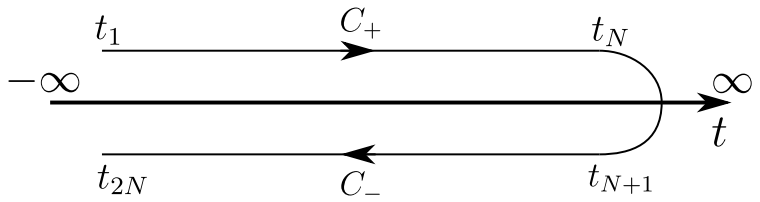

Figure A.1: The Keldysh contour $\mathcal{C}$ including the forward C_+ and the backward C_- branches.

In the Keldysh formalism, where the time evolution of observables is governed by the contour, the path-ordered Green's function is defined as a quantum statistical averaging of the fermion operators

$$G^{c}_{ij}(t,t') = -i\langle \hat{T}_C\{\hat{c}_i(t);\hat{c}^{\dagger}_j(t')\}\rangle, \tag{A.31}$$

where $\hat{c}^{\dagger}_j(t')$ is creation operator for electron in state j and time t', $\hat{c}_i(t)$ is annihilation operator for electron in state i and time t. The single particle Green's function describes its propagation through time and space. Here $\hat{T}_C$ is a time ordering operator which governs the operator's positions on the Keldysh contour [154]. The contour-ordered Green's function can be divided on four different types, depending on the forward or reverse branches:

$$G^{c}_{ij}(t,t') = \begin{cases} G^{c}_{ij}(t,t') = -i\langle \hat{T}_C\{\hat{c}_i(t);\hat{c}^{\dagger}_j(t')\}\rangle & t,t' \in C_+ \quad \textit{"casual"}, \\ G^{>}_{ij}(t,t') = -i\langle \hat{c}_i(t);\hat{c}^{\dagger}_j(t')\rangle & t \in C_-, t' \in C_+ \quad \textit{"greater"}, \\ G^{<}_{ij}(t,t') = +i\langle \hat{c}^{\dagger}_j(t');\hat{c}_i(t)\rangle & t \in C_+, t' \in C_- \quad \textit{"lesser"}, \\ G^{\tilde{c}}_{ij}(t,t') = -i\langle \tilde{T}_c\{\hat{c}_i(t);\hat{c}^{\dagger}_j(t')\}\rangle & t,t' \in C_- \quad \textit{"antitime-ordered"}. \end{cases} \tag{A.32}$$

The "*casual*" Green's function is also called "*time-ordered*" Green's function. For the fermionic operators the time-ordering operator $\hat{T}_C$ fulfils the following conditions

$$\hat{T}_C\{\hat{c}_i(t);\hat{c}^{\dagger}_j(t')\} = \begin{cases} \hat{c}_i(t)\hat{c}^{\dagger}_j(t') & \text{if } t > t' \\ -\hat{c}^{\dagger}_j(t')\hat{c}_i(t) & \text{if } t' > t. \end{cases} \tag{A.33}$$

Fermionic operators obey the anticommutation relations:

$$\{\hat{c}_i, \hat{c}_j\} = 0, \tag{A.34}$$

$$\{\hat{c}_i^\dagger, \hat{c}_j^\dagger\} = 0, \tag{A.35}$$

$$\{\hat{c}_i, \hat{c}_j^\dagger\} = \delta_{ij}, \tag{A.36}$$

where anti-commutator is defined as $\{A, B\} = AB + BA$ and δ_{ij} is the Kronecker delta.

Having defined the contour-ordered functions, we can write down fundamental objects of the Keldysh technique: the *retarded* (r), *advanced* (a) and Keldysh (k) Green's functions

$$\begin{aligned} G_{ij}^r(t,t') &= -i\theta(t-t')\langle\{\hat{c}_i(t); \hat{c}_j^\dagger(t')\}\rangle \\ &= \theta(t-t')\left[G_{ij}^>(t,t') - G_{ij}^<(t,t')\right], \end{aligned} \tag{A.37}$$

$$\begin{aligned} G_{ij}^a(t,t') &= i\theta(t'-t)\langle\{\hat{c}_i(t); \hat{c}_j^\dagger(t')\}\rangle \\ &= \theta(t'-t)\left[G_{ij}^<(t,t') - G_{ij}^>(t,t')\right], \end{aligned} \tag{A.38}$$

$$G_{ij}^k(t,t') = G_{ij}^>(t,t') + G_{ij}^<(t,t'), \tag{A.39}$$

where $\theta(x)$ is a Heaviside step function. These relations are only valid when $t \neq t'$. Since by definition of the *greater* and *lesser* Green's function in (A.32) $[G^<]^\dagger = -G^>$, one notices that

$$[G^r]^\dagger = G^a, \tag{A.40}$$

$$[G^k]^\dagger = -G^k. \tag{A.41}$$

For non-zero temperatures $T > 0$, the Green's function becomes more complex. In order to obtain information about the particle and its space-time position as a function of temperature, we need to introduce the *Matsubara* Green's function [159, 160]. Thermal averaging $\langle\hat{O}\rangle = \mathrm{Tr}\left(e^{-\beta\hat{H}}\right) = \mathrm{Tr}\left(e^{+i(-i\beta)\hat{H}}\right) = \mathrm{Tr}\left(e^{+i\tau\hat{H}}\right)$ is equivalent to evolution along imaginary axis from 0 to $-i\beta$, see Fig. A.2. Therefore, the Matsubara's approach is called the imaginary time approach with

$$t \to i\tau. \tag{A.42}$$

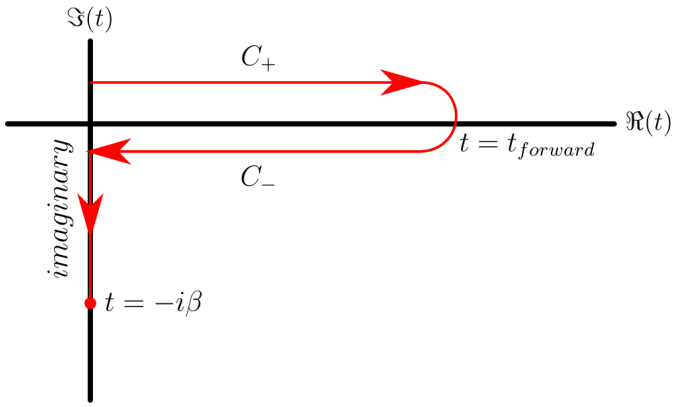

Figure A.2: The Keldysh or Konstantinov-Perel's contour in the complex time plane with forward C_+, backward C_- and imaginary branches.

Recalling that, for general operators A and B, the Green's function is homogeneous with respect to time, i.e. it depends only on a difference of the imaginary times:

$$G_{AB}(\tau_1, \tau_2) = G_{AB}(\tau_1 - \tau_2) \equiv G_{AB}(\tau), \tag{A.43}$$

and that the function $G_{AB}(\tau)$ is periodic (anti-periodic) function for bosonic (fermionic) Green's functions

$$G_{AB}(\tau - m\beta) = -\frac{1}{Z}\mathrm{Tr}\left(e^{-\beta\hat{H}}\hat{T}_C A\,(\tau - m\beta)\,B\right) \tag{A.44}$$

with a general argument τ being in range

$$m\beta < \tau < (m+1)\beta, \tag{A.45}$$

where m denotes an arbitrary integer, we can show its other properties. If $\tau - m\beta > 0$ the Green's function fulfills

$$G_{AB}(\tau - m\beta) = -\frac{1}{Z}\mathrm{Tr}\left(e^{-\beta\hat{H}} BA\,(\tau - (m+1)\beta)\right), \tag{A.46}$$

and if $\tau < 0$ the operators obey $BA(\tau) = -\eta\hat{T}_C A(\tau)B$, where η is an integer number. Since $\tau - (m+1)\beta < 0$ the Green's function follows

$$G_{AB}(\tau - m\beta) = -\eta G_{AB}(\tau - (m+1)\beta). \tag{A.47}$$

In particular case, when $m = -1$, we see that

$$G_{AB}(\tau) = -\eta G_{AB}(\tau + \beta) \tag{A.48}$$

and the *Matsubara* functions are periodic (anti-periodic) for bosonic (fermionic) choice of the time ordering. Since both functions are periodic with period 2β the *Matsubara* Green's function can be expanded in the Fourier series as follows

$$G^M_{AB}(\tau) = \frac{1}{\beta}\sum_{m=-\infty}^{\infty} e^{-i\omega_m\tau} G^M_{AB}(\omega_m) \tag{A.49}$$

with frequencies distinct for bosonic and fermionic propagators

$$\omega_m = \begin{cases} \frac{2m\pi}{\beta} & \text{for bosons,} \\ \frac{(2m+1)\pi}{\beta} & \text{for fermions.} \end{cases} \tag{A.50}$$

A.4 Langreth rules

In the uncorrelated case the contour ordered Green's function satisfies the Dyson equation of the general form

$$G^c(t,t') = g^c(t,t') + \int_C d\tau \int_C d\tau' g^c(t,\tau)\Sigma^c(\tau,\tau')G^c(\tau',t'), \tag{A.51}$$

where $g^c(t,t')$ is bare Green's function and $\Sigma^c(\tau,\tau')$ a self-energy term. In this equation the time convolution between the functions occurs via

$$C(t,t') = \int_C d\tau A(t,\tau)B(\tau,t'), \tag{A.52}$$

with the integrations over the extra time argument τ on the Keldysh contour. We can assume that t is on the first part of the contour and t' belongs to the second half. The time convolution between the functions deforms the Keldysh contour. For future investigation let us analyse a "*lesser*" function

$$C^<(t,t') = \int_{C_1} d\tau A(t,\tau)B^<(\tau,t') + \int_{C_2} d\tau A^<(t,\tau)B(\tau,t'). \tag{A.53}$$

Lesser function $C^<(t,t')$ can be split into two integrals with two different branches C_1 and C_2, which means that we deform the Keldysh contour by adding two extra branches. In the first term, the sign $<$ for function B occurs because in the integration over contour C_1 argument τ is always lesser than t' (similar for the second term). The first part of (A.53) can be slit into two parts

$$\begin{aligned} \int_{C_1} d\tau A(t,\tau)B^<(\tau,t') &= \int_{-\infty}^{t} d\tau A^>(t,\tau)B^<(\tau,t') + \int_{t}^{-\infty} d\tau A^<(t,\tau)B^<(\tau,t') \\ &\equiv \int_{-\infty}^{\infty} d\tau A^r(t,\tau)B^<(\tau,t') \end{aligned} \tag{A.54}$$

due to definition of the *retarded* Green's function (A.37). The second term on the right hand side of (A.53) can be analysed in the similar manner and in the result B function is "*advanced*" function

$$\int_{C_2} d\tau A^<(t,\tau)B(\tau,t') = \int_{C_2} d\tau A^<(t,\tau)B^a(\tau,t'). \tag{A.55}$$

Combining (A.54) and (A.55) we can rewrite (A.53) in form of the first Langreth's rule:

$$C^<(t,t') = \int_{-\infty}^{\infty} d\tau \left[A^r(t,\tau)B^<(\tau,t') + A^<(t,\tau)B^a(\tau,t')\right]. \tag{A.56}$$

The "*retarded*" or "*advanced*" component of a contour ordered $C(t,t')$ (A.52) function is

$$C^{r,a}(t,t') = \int_{-\infty}^{\infty} d\tau A^{r,a}(t,\tau)B^{r,a}(\tau,t'). \tag{A.57}$$

The proof for "*retarded*" function is as follows:

$$\begin{aligned}
C^r(t,t') &= \theta(t-t')\left(C^>(t,t') - C^<(t,t')\right) \\
&= \theta(t-t')\int_{-\infty}^{\infty} d\tau[A^r(t,\tau)(B^>(\tau,t') - B^<(\tau,t')) \\
&+ (A^>(t,\tau) - A^<(t,\tau))B^a(\tau,t')] \\
&= \theta(t-t')[\int_{-\infty}^{t} d\tau(A^>(t,\tau) - A^<(t,\tau))(B^>(\tau,t') - B^<(\tau,t')) \\
&+ \int_{-\infty}^{t'} d\tau(A^>(t,\tau) - A^<(t,\tau))(B^>(\tau,t') - B^<(\tau,t'))] \\
&= \int_{t'}^{t} d\tau A^r(t,\tau)B^r(\tau,t').
\end{aligned} \tag{A.58}$$

For the time convolution of more than two functions $C(t,t') = \int_C ABC$ the "*lesser*" or "*greater*" function type of $C(t,t')$ posses the form

$$C^{><} = \int_t [A^r B^r C^{><} + A^r B^{><} C^a + A^{><} B^a C^a], \tag{A.59}$$

where the integration is over real time axis. The *lesser* function $C^<$ reduces to

$$C^< = \int_t A^r B^< C^a, \tag{A.60}$$

when a steady state is turned on by adiabatic evolution from $t = -\infty$ to t.

A.5 Convolution in Fourier space

With the Keldysh contour function $C(t,t')$ can be rewritten in the form of product of other functions $C(t,t') = \int_{-\infty}^{\infty} d\tau A(t,\tau)B(\tau,t')$. Below, the proof of the time convolution between two-times function in Fourier space is presented:

$$C(t,t') = \int_{-\infty}^{\infty} d\tau A(t,\tau)B(\tau,t') = \int_{-\infty}^{\infty} d\tau \sum_{k,m_1} \int_{-\omega/2}^{\omega/2} d\varepsilon_1 e^{-i(\varepsilon_1+k\omega)t+i(\varepsilon_1+m_1\omega)\tau} A_{km_1}(\varepsilon_1)\times$$
$$\sum_{l,m_2} \int_{-\omega/2}^{\omega/2} d\varepsilon_1 e^{-i(\varepsilon_2+l\omega)\tau+i(\varepsilon_2+m_2\omega)t'} B_{lm_2}(\varepsilon_2) =$$
$$\left(\prod_{i=1,2}\sum_{n_i,m_j}\int_{-\omega/2}^{\omega/2} d\varepsilon_i\right) e^{-i(\varepsilon_1+k\omega)t+i(\varepsilon_1+m_1\omega)\tau} e^{-i(\varepsilon_2+l\omega)\tau+i(\varepsilon_2+m_2\omega)t'} A_{km_1}(\varepsilon_1)B_{lm_2}(\varepsilon_2) =$$
$$\left(\prod_{i=1,2}\sum_{n_i,m_j}\int_{-\omega/2}^{\omega/2} d\varepsilon_i\right) e^{-i(\varepsilon_1+k\omega)t+i(\varepsilon_2+m_2\omega)t'} \delta(\varepsilon_1-\varepsilon_2+m_1\omega-l\omega) A_{km_1}(\varepsilon_1)B_{lm_2}(\varepsilon_2). \tag{A.61}$$

Then we can make the following substitution:
$\left|\varepsilon \in \langle -\omega/2;\omega/2) \Rightarrow \delta(\varepsilon_1-\varepsilon_2+(m_1-l)\omega) = \delta(\varepsilon_1-\varepsilon_1)\delta_{m_1,l}\right|$
obtaining:

$$C(t,t') = \sum_{k,l,m_2} \int_{-\omega/2}^{\omega/2} d\varepsilon e^{-i(\varepsilon+k\omega)t+i(\varepsilon+m_2\omega)t'} A_{km_1}(\varepsilon)B_{lm_2}(\varepsilon). \tag{A.62}$$

In the next step, we change the summation index as follows
$|k \to n, l \to k, m_2 \to m_1|$ to obtain

$$C(t,t') = \sum_{n,m,k} \int_{-\omega/2}^{\omega/2} d\varepsilon e^{-i(\varepsilon+n\omega)t+i(\varepsilon+m\omega)t'} A_{nk}(\varepsilon)B_{km}(\varepsilon). \tag{A.63}$$

After the Fourier transformation, $C(t,t')$ becomes $C_{nm}(\varepsilon)$ equal to the convolution of two functions in Fourier space:

$$C_{nm}(\varepsilon) = \sum_k A_{nk}(\varepsilon)B_{km}(\varepsilon). \tag{A.64}$$

A.6 Bare Green's function in Floquet space

By definition, the bare Green's function for quantum dot has following form

$$g^c_{d_\sigma,d^\dagger_{\sigma'}}(t,t') = -i\langle \hat{T}_C\{d_\sigma(t), d^\dagger_{\sigma'}(t')\}\rangle. \tag{A.65}$$

Solution of the equation of motion for the bare Green's function $g^c_{d_\sigma,d^\dagger_{\sigma'}}(t,t')$ of the single quantum dot described by Hamiltonian $H(t)=\sum_\sigma \varepsilon_d(t)d^\dagger_\sigma d_\sigma$ requires the time derivative of operator $d_\sigma(t)$

$$\partial_t d_\sigma(t) = i[H(t),d_\sigma(t)] = ie^{i\int_0^t dt' H(t')}[H(t),d_\sigma]e^{-i\int_0^t dt' H(t')} \tag{A.66}$$

$$= ie^{i\int_0^t dt' H(t')}[H(t),d_\sigma]e^{-i\int_0^t dt' H(t')} \tag{A.67}$$

$$= i\sum_{\sigma'}\varepsilon_{d\sigma'}(t)e^{i\int_0^t dt' H(t')}[d^\dagger_{\sigma'}(t)d_{\sigma'}(t),d_\sigma(t)]e^{-i\int_0^t dt' H(t')} \tag{A.68}$$

$$= -i\varepsilon_{d\sigma'}(t)e^{i\int_0^t dt' H(t')}d_\sigma e^{-i\int_0^t dt' H(t')} = -i\varepsilon_d(t)d_\sigma(t). \tag{A.69}$$

In result, we obtain

$$i\partial_t g^c_{d_\sigma,d^\dagger_{\sigma'}}(t,t') = \delta_c(t-t')\delta_{\sigma\sigma'} - i\langle\hat{T}_C\{i\partial_t d_\sigma(t),d^\dagger_{\sigma'}(t')\rangle = \tag{A.70}$$

$$\delta_c(t-t')\delta_{\sigma\sigma'} - i\varepsilon_d(t)\langle\hat{T}_C\{d_\sigma(t),d^\dagger_{\sigma'}(t')\rangle = \tag{A.71}$$

$$\delta_c(t-t')\delta_{\sigma\sigma'} + \varepsilon_d(t)g^c_{d_\sigma,d^\dagger_{\sigma'}}(t,t'), \tag{A.72}$$

which can be recast to form:

$$(i\partial_t - \varepsilon_d(t))g^c_{d_\sigma,d^\dagger_{\sigma'}}(t,t') = \delta_c(t-t')\delta_{\sigma,\sigma'}, \tag{A.73}$$

where $\varepsilon_d(t)=\varepsilon_d^0+A\cos(\omega t)$ is time dependent discrete energy level of quantum dot, ε_d^0 is the stationary quantum dot energy level and A amplitude of the perturbation. Writing the discrete time dependent quantum dot energy level $\varepsilon_d(t)=\sum_k \varepsilon^k_{d\sigma}e^{-i\omega kt}$ in Fourier space and applying the Langreth's rule (A.57) we obtain the retarded and advanced equation of motion form of the Green's function

$$(i\partial_t \pm i0^+ - \sum_k \varepsilon^k_{d\sigma}e^{-i\omega kt})g^{r,a}_{d_\sigma,d^\dagger_{\sigma'}}(t,t') = \delta_c(t-t')\delta_{\sigma,\sigma'}. \tag{A.74}$$

Here, our aim is to obtain time-independent equations. For this purpose, we apply the Fourier transform to both sides of the equation

$$\left(i\partial_t \pm i0^+ - \sum_k \varepsilon^k_{d\sigma}e^{-i\omega kt}\right)\sum_{n,m}\int_{-\omega/2}^{\omega/2} d\varepsilon e^{-i(\varepsilon+n\omega)t+i(\varepsilon+m\omega)t'}g^{r,a}_{d_\sigma,d^\dagger_{\sigma'},nm}(\varepsilon) =$$

$$\sum_{n,m}\int_{-\omega/2}^{\omega/2} d\varepsilon e^{-i(\varepsilon+n\omega)t+i(\varepsilon+m\omega)t'}\delta_{nm}. \tag{A.75}$$

Rewriting the equation in the form

$$(i\partial_t \pm i0^+) \sum_{n,m} \int_{-\omega/2}^{\omega/2} d\varepsilon e^{-i(\varepsilon+n\omega)t+i(\varepsilon+m\omega)t'} g^{r,a}_{d_\sigma,d^\dagger_{\sigma'},nm}(\varepsilon) -$$
$$\sum_{n,m,k} \int_{-\omega/2}^{\omega/2} d\varepsilon e^{-i(\varepsilon+n\omega)t+i(\varepsilon+m\omega)t'} e^{-i\omega kt} \varepsilon^k_{d\sigma} g^{r,a}_{d_\sigma,d^\dagger_{\sigma'},nm}(\varepsilon) =$$
$$\sum_{n,m} \int_{-\omega/2}^{\omega/2} d\varepsilon e^{-i(\varepsilon+n\omega)t+i(\varepsilon+m\omega)t'} \delta_{nm}, \tag{A.76}$$

and substituting the following calculated derivative $i\partial_t e^{-i(\varepsilon+n\omega)t} = (\varepsilon+n\omega)e^{-i(\varepsilon+n\omega)t}$ we obtain:

$$\sum_{n,m} \int_{-\omega/2}^{\omega/2} d\varepsilon \left(\varepsilon \pm i0^+ + n\omega\right) e^{-i(\varepsilon+n\omega)t+i(\varepsilon+m\omega)t'} g^{r,a}_{d_\sigma,d^\dagger_{\sigma'},nm}(\varepsilon) -$$
$$\sum_{n,m,k} \int_{-\omega/2}^{\omega/2} d\varepsilon e^{-i[\varepsilon+(n+k)\omega]t+i(\varepsilon+m\omega)t'} \varepsilon^k_{d\sigma} g^{r,a}_{d_\sigma,d^\dagger_{\sigma'},nm}(\varepsilon) =$$
$$\sum_{n,m} \int_{-\omega/2}^{\omega/2} d\varepsilon e^{-i(\varepsilon+n\omega)t+i(\varepsilon+m\omega)t'} \delta_{nm}. \tag{A.77}$$

We introduce the extra summation over the additional index k

$$\sum_{n,m,k} \int_{-\omega/2}^{\omega/2} d\varepsilon \left(\varepsilon \pm i0^+ + k\omega\right) e^{-i(\varepsilon+k\omega)t+i(\varepsilon+m\omega)t'} \delta_{n,k} g^{r,a}_{d_\sigma,d^\dagger_{\sigma'},km}(\varepsilon) - \tag{A.78}$$
$$\sum_{n,m,k,k} \int_{-\omega/2}^{\omega/2} d\varepsilon e^{-i[\varepsilon+(k+k)\omega]t+i(\varepsilon+m\omega)t'} \delta_{n,k} \varepsilon^k_{d\sigma} g^{r,a}_{d_\sigma,d^\dagger_{\sigma'},km}(\varepsilon) =$$
$$\sum_{n,m} \int_{-\omega/2}^{\omega/2} d\varepsilon e^{-i(\varepsilon+n\omega)t+i(\varepsilon+m\omega)t'} \delta_{nm}, \tag{A.79}$$

and replace the index k by $k = n - k$ to finally get

$$\sum_{n,m,k} \int_{-\omega/2}^{\omega/2} d\varepsilon \left(\varepsilon \pm i0^+ + k\omega\right) e^{-i(\varepsilon+k\omega)t+i(\varepsilon+m\omega)t'} \delta_{n,k} g^{r,a}_{d_\sigma,d^\dagger_{\sigma'},km}(\varepsilon) -$$
$$\sum_{n,m,k} \int_{-\omega/2}^{\omega/2} d\varepsilon e^{-i(\varepsilon+k\omega)t+i(\varepsilon+m\omega)t'} \varepsilon^{n-k}_{d\sigma} g^{r,a}_{d_\sigma,d^\dagger_{\sigma'},km}(\varepsilon) =$$
$$\sum_{n,m} \int_{-\omega/2}^{\omega/2} d\varepsilon e^{-i(\varepsilon+n\omega)t+i(\varepsilon+m\omega)t'} \delta_{nm}. \tag{A.80}$$

In the next step we can skip the Fourier integration on both sides and write the result in the form of time-independent equation

$$\sum_k \left[(\varepsilon \pm i0^+ + n\omega)\delta_{nk} - \varepsilon_{d\sigma}^{n-k}\right] g^{r,a}_{d_\sigma, d^\dagger_{\sigma'}, km}(\varepsilon) = 1$$

$$\Rightarrow$$

$$g^{r,a-1}_{d_\sigma, d^\dagger_{\sigma'}, nm}(\varepsilon) = (\varepsilon \pm i0^+ + n\omega)\delta_{nm} - \varepsilon_{d\sigma}^{n-m}, \tag{A.81}$$

which is the bare Green's function in the Fourier space.

A.7 Diagonalization of bare Green's function

In the preceding part, we obtained the energy-dependent Green's function in Fourier space (A.81). Here we introduce Λ function [129], defined as follows

$$\Lambda_{\sigma,nm} = \langle\langle \sigma n | u_{\sigma,m}\rangle\rangle = \langle\sigma|\frac{1}{T}\int_0^T dt e^{i(n-m)\omega t}|u_\sigma(t)\rangle = \langle\sigma|\frac{1}{T}\int_0^T dt e^{i(n-m)\omega t} e^{i\varepsilon_d^0 t}|\sigma(t)\rangle =$$
$$\frac{1}{T}\int_0^T dt e^{i(n-m)\omega t} e^{i\varepsilon_d^0 t}\langle\sigma|U(t,0)|\sigma\rangle = \frac{1}{T}\int_0^T dt e^{i(n-m)\omega t} e^{i\varepsilon_d^0 t} e^{-i\int_0^t d\tau \varepsilon_{d\sigma}(\tau)} =$$
$$\frac{1}{T}\int_0^T dt e^{i(n-m)\omega t} e^{-i\int_0^t d\tau (\varepsilon_{d\sigma}(\tau) - \varepsilon_d^0)}, \tag{A.82}$$

where $\langle\langle \sigma n|$ acts on a state in the Floquet space $|u_{\sigma,m}\rangle\rangle$. The operator Λ fulfils the following property

$$\sum_k \Lambda_{\sigma,nk}\Lambda^\dagger_{\sigma,km} = \sum_k \frac{1}{T}\int_0^T dt e^{i(n-k)\omega t} e^{-i\int_0^t d\tau(\varepsilon_{d\sigma}(\tau)-\varepsilon_d^0)} \frac{1}{T}\int_0^T dt e^{-i(k-m)\omega t} e^{i\int_0^t d\tau(\varepsilon_{d\sigma}(\tau)-\varepsilon_d^0)} =$$
$$\sum_k \int_{-\pi}^{\pi}\frac{dx}{2\pi} e^{i(n-k)x} e^{-\frac{i}{\omega}\int_0^x dz(\varepsilon_{d\sigma}(z/\omega)-\varepsilon_d^0)} \int_{-\pi}^{\pi}\frac{dy}{2\pi} e^{-i(m-k)y} e^{-\frac{i}{\omega}\int_y^0 dz(\varepsilon_{d\sigma}(z/\omega)-\varepsilon_d^0)} =$$
$$\int_{-\pi}^{\pi}\frac{dx}{2\pi}\int_{-\pi}^{\pi}\frac{dy}{2\pi}\sum_k e^{i(nx-my)-ik(x-y)} e^{-\frac{i}{\omega}\int_0^x dz(\varepsilon_{d\sigma}(z/\omega)-\varepsilon_d^0)} e^{-\frac{i}{\omega}\int_y^0 dz(\varepsilon_{d\sigma}(z/\omega)-\varepsilon_d^0)} =$$
$$\int_{-\pi}^{\pi}\frac{dx}{2\pi}\int_{-\pi}^{\pi}\frac{dy}{2\pi}\sum_k e^{i(nx-my)-ik(x-y)} e^{-\frac{i}{\omega}\int_y^x dz(\varepsilon_{d\sigma}(z/\omega)-\varepsilon_d^0)} =$$
$$\int_{-\pi}^{\pi}\frac{dx}{2\pi}\int_{-\pi}^{\pi}\frac{dy}{2\pi}\delta(x-y) e^{i(nx-my)} e^{-\frac{i}{\omega}\int_y^x dz(\varepsilon_{d\sigma}(z/\omega)-\varepsilon_d^0)} =$$
$$\int_{-\pi}^{\pi}\frac{dx}{2\pi} e^{i(n-m)x} = \delta_{nm}. \tag{A.83}$$

Here, we used the mathematical property of the Dirac delta $f(x) = \int \delta(x-y)f(y)dy$. The product of two Λ operators gives the Kronecker delta $\sum_k \Lambda_{\sigma,nk}\Lambda^\dagger_{\sigma,km} = \delta_{nm}$. To

obtain the diagonal kind of the bare Green's function $D^{r,a-1}_{d_\sigma,d^\dagger_\sigma,nn}(\varepsilon)$ we act on both sides of the inverse Green's function $g^{r,a-1}_{d_\sigma,d^\dagger_\sigma,kl}(\varepsilon)$ by Λ operator

$$
\begin{aligned}
&D^{r,a-1}_{d_\sigma,d^\dagger_\sigma,nn}(\varepsilon) = \sum_{kl} \Lambda^\dagger_{\sigma,nk} g^{r,a-1}_{d_\sigma,d^\dagger_\sigma,kl}(\varepsilon)\Lambda_{\sigma,ln} = \\
&\sum_{kl} \Lambda^\dagger_{\sigma,nk}[(\varepsilon \pm i0^+ + k\omega)\delta_{kl} - \varepsilon_{d\sigma,k-l}]\Lambda_{\sigma,ln} = \\
&\sum_{kl} \Lambda^\dagger_{\sigma,nk}(\varepsilon \pm i0^+)\delta_{kl}\Lambda_{\sigma,ln} + \sum_{kl} \Lambda^\dagger_{\sigma,nk} k\omega\delta_{kl}\Lambda_{\sigma,ln} - \sum_{kl} \Lambda^\dagger_{\sigma,nk}\varepsilon_{d\sigma,k-l}\Lambda_{\sigma,ln} = \\
&\sum_{k} \Lambda^\dagger_{\sigma,nk}(\varepsilon \pm i0^+)\Lambda_{\sigma,kn} + \sum_{k} \Lambda^\dagger_{\sigma,nk} k\omega\Lambda_{\sigma,kn} - \sum_{kl} \Lambda^\dagger_{\sigma,nk}\varepsilon_{d\sigma,k-l}\Lambda_{\sigma,ln} = \\
&\varepsilon \pm i0^+ + (n\omega + \varepsilon_{d\sigma})\delta_{nn} - \varepsilon_{d\sigma,n-n} - \varepsilon_{d\sigma,k-l}\delta_{kl}\delta_{ln} = \\
&\varepsilon \pm i0^+ + n\omega - \varepsilon_{d\sigma,k-l}\delta_{kl} = \varepsilon \pm i0^+ + n\omega - \varepsilon_{d\sigma,0},
\end{aligned}
\tag{A.84}
$$

where we used the following relation

$$
\sum_{k} \Lambda_{\sigma,nk} k\omega \Lambda^\dagger_{\sigma,km} = (n\omega + \varepsilon^0_d) - \varepsilon_{d\sigma,m-n}. \tag{A.85}
$$

To prove (A.85), we need to rewrite the limits of integration in (A.85) in the following manner

$$
\begin{aligned}
&\sum_{k} \Lambda_{\sigma,nk} k\omega \Lambda^\dagger_{\sigma,km} = \int_{-\pi}^{\pi} \frac{dx}{2\pi} \int_{-\pi}^{\pi} \frac{dy}{2\pi} \sum_{k} e^{i(nx-my)-ik(x-y)} k\omega e^{-\frac{i}{\omega}\int_y^x dz(\varepsilon_{d\sigma}(z/\omega)-\varepsilon^0_d)} = \\
&\int_{-\pi}^{\pi} \frac{dx}{2\pi} \int_{-\pi}^{\pi} dy e^{i(nx-my)} k\omega e^{-\frac{i}{\omega}\int_y^x dz(\varepsilon_{d\sigma}(z/\omega)-\varepsilon^0_d)}.
\end{aligned}
\tag{A.86}
$$

Using the definition of the Dirac delta and its differential

$$
\begin{aligned}
&\delta(x-y) = \frac{1}{2\pi}\sum_{k} e^{-ik(x-y)} \\
&i\partial_x\delta(x-y) = i(-i)k\delta(x-y) = k\delta(x-y),
\end{aligned}
\tag{A.87}
$$

we perform some analytical calculations, to obtain

$$
\begin{aligned}
&\sum_{k} \Lambda_{\sigma,nk} k\omega \Lambda^\dagger_{\sigma,km} = \int_{-\pi}^{\pi} \frac{dx}{2\pi} \int_{-\pi}^{\pi} dy e^{i(nx-my)} i\omega[\partial_x\delta(x-y)] e^{-\frac{i}{\omega}\int_y^x dz(\varepsilon_{d\sigma}(z/\omega)-\varepsilon^0_d)} = \\
&e^{i(nx-my)} i\omega\delta(x-y) e^{-\frac{i}{\omega}\int_y^x dz(\varepsilon_{d\sigma}(z/\omega)-\varepsilon^0_d)}|^{\pi}_{-\pi} + \\
&\int_{-\pi}^{\pi} \frac{dx}{2\pi} \int_{-\pi}^{\pi} dy e^{i(nx-my)} \delta(x-y)[n\omega - \varepsilon_{d\sigma}(z/\omega) + \varepsilon^0_d] e^{-\frac{i}{\omega}\int_y^x dz(\varepsilon_{d\sigma}(z/\omega)-\varepsilon^0_d)} = \\
&\int_{-\pi}^{\pi} \frac{dx}{2\pi} e^{i(n-m)x}[n\omega - \varepsilon_{d\sigma}(z/\omega) + \varepsilon^0_d] = \int_{-\pi}^{\pi} \frac{dx}{2\pi} e^{i(n-m)x}[n\omega + \varepsilon^0_d] - \\
&\int_{-\pi}^{\pi} \frac{dx}{2\pi} e^{i(n-m)x} \varepsilon_{d\sigma}(z/\omega) = (n\omega + \varepsilon^0_d) - \varepsilon_{d\sigma,m-n}.
\end{aligned}
\tag{A.88}
$$

In result, the inverse diagonal bare Green's function is given by

$$D^{r,a-1}_{d_\sigma,d^\dagger_\sigma,nn}(\varepsilon) = \varepsilon \pm i0^+ + n\omega - \varepsilon_{d\sigma,0}, \tag{A.89}$$

where $n\omega - \varepsilon_{d\sigma,0}$ is the eigenvalue of Hamiltonian $\hat{H}_F$ in state $|u_{\sigma,n}\rangle\rangle$. Then the inverse diagonal Green's function can be written as

$$D^{r,a-1}_{d_\sigma,d^\dagger_\sigma,nn}(\varepsilon) = \varepsilon \pm i0^+ - \langle\langle u_{\sigma,n}|\hat{H}_F|u_{\sigma,n}\rangle\rangle. \tag{A.90}$$

In a similar way, we can obtain the bare Green's function expressed by Λ operators and determine the diagonal part of the Green's function in the Floquet space

$$g^{r,a}_{d_\sigma,d^\dagger_\sigma,nm}(\varepsilon) = \sum_k \Lambda^\dagger_{\sigma,nk} D^{r,a}_{d_\sigma,d^\dagger_\sigma,kk}(\varepsilon)\Lambda_{\sigma,km}. \tag{A.91}$$

For the oscillating energy level $\varepsilon_d(t) = \varepsilon^0_d + A\cos(\omega t)$ the operator $\Lambda_{\sigma,nm}$ takes the form

$$\begin{aligned}
&\Lambda_{\sigma,nm} = \frac{1}{T}\int_0^T dt e^{i(n-m)\omega t} e^{-i\int_0^t d\tau(\varepsilon^0_d + A\cos(\omega\tau) - \varepsilon^0_d)} = \\
&\frac{1}{T}\int_0^T dt e^{i(n-m)\omega t} e^{-i\int_0^t d\tau(\varepsilon^0_d + A\cos(\omega\tau) - \varepsilon^0_d)} = \frac{1}{T}\int_0^T dt e^{i(n-m)\omega t} e^{-i\int_0^t d\tau A\cos(\omega\tau)} = \\
&\frac{1}{T}\int_0^T dt e^{i(n-m)\omega t} e^{-i\frac{A}{\omega}\sin(\omega t)},
\end{aligned} \tag{A.92}$$

where we used the Bessel function property [161]

$$e^{-ia\sin(\omega t)} = \sum_{k=-\infty}^{\infty} e^{-ik\omega t} J_k(a) \tag{A.93}$$

$$\begin{aligned}
&\Lambda_{\sigma,nm} = \frac{1}{T}\int_0^T dt e^{i(n-m)\omega t} \sum_{k=-\infty}^{\infty} e^{-ik\omega t} J_k\left(\frac{A}{\omega}\right) = \\
&\frac{1}{T}\int_0^T dt \sum_{k=-\infty}^{\infty} e^{i(n-m-k)\omega t} J_k\left(\frac{A}{\omega}\right) = \frac{1}{T}\int_0^T dt \sum_{k=-\infty}^{\infty} \delta_{k,n-m} e^{i(k-k)\omega t} J_k\left(\frac{A}{\omega}\right) = \\
&\frac{1}{T}\int_0^T dt \sum_{k=-\infty}^{\infty} \delta_{k,n-m} J_k\left(\frac{A}{\omega}\right) = J_{n-m}\left(\frac{A}{\omega}\right).
\end{aligned} \tag{A.94}$$

to express the operator Λ by the Bessel function dependent on the Fourier coefficients, the driving amplitude, and the frequency of the perturbation

$$\Lambda_{\sigma,nm} = J_{n-m}\left(\frac{A}{\omega}\right). \tag{A.95}$$

Now we are able to transform the bare Green's function as follows

$$g^{r,a}_{d_\sigma,d^\dagger_\sigma,nm}(\varepsilon) = \sum_k \Lambda^\dagger_{\sigma,nk} D^{r,a}_{d_\sigma,d^\dagger_\sigma,kk}(\varepsilon)\Lambda_{\sigma,km} =$$
$$\sum_k J_{n-k}\left(\frac{A}{\omega}\right) D^{r,a}_{d_\sigma,d^\dagger_\sigma,kk}(\varepsilon) J_{k-m}\left(\frac{A}{\omega}\right) =$$
$$\sum_k \frac{J_{n-k}\left(\frac{A}{\omega}\right) J_{k-m}\left(\frac{A}{\omega}\right)}{\varepsilon \pm i0^+ + k\omega - \varepsilon_d^0}, \tag{A.96}$$

and get the final formula

$$g^{r,a}_{d_\sigma,d^\dagger_\sigma,nm}(\varepsilon) = \sum_k \frac{J_{n-k}\left(\frac{A}{\omega}\right) J_{k-m}\left(\frac{A}{\omega}\right)}{\varepsilon \pm i0^+ + k\omega - \varepsilon_d^0}. \tag{A.97}$$

A.8 Mixed Green's functions

Quantum dot - metal interface

The contour-ordered Green's functions which describe the quantum dot coupled to the metallic lead are defined by

$$G^c_{c_{k\sigma},d^\dagger_{\sigma'}}(t,t') = -i\langle \hat{T}_C\{c_{k\sigma}(t), d^\dagger_{\sigma'}(t')\}\rangle, \tag{A.98}$$

$$G^c_{c^\dagger_{k\sigma},d^\dagger_{\sigma'}}(t,t') = -i\langle \hat{T}_C\{c^\dagger_{k\sigma}(t), d^\dagger_{\sigma'}(t')\}\rangle. \tag{A.99}$$

To determine these Green's functions we must solve the following differential equations

$$i\partial_t G^c_{c_{Nk\sigma},d^\dagger_{\sigma'}}(t,t') = -i\langle \hat{T}_C\{\partial_t c_{Nk\sigma}(t), d^\dagger_{\sigma'}(t')\}\rangle, \tag{A.100}$$

$$i\partial_t G^c_{c^\dagger_{Nk\sigma},d^\dagger_{\sigma'}}(t,t') = -i\langle \hat{T}_C\{\partial_t c^\dagger_{Nk\sigma}(t), d^\dagger_{\sigma'}(t')\}\rangle. \tag{A.101}$$

To obtain the solution of such functions we need to calculate the equation of motions for the operators $c_{Nk\sigma}(t)$ and $c^\dagger_{Nk\sigma}(t)$ with the corresponding Hamiltonian $H(t)$ defined in (3.1)

$$i\partial_t c_{Nk\sigma}(t) = i[H(t), c_{Nk\sigma}(t)] = \varepsilon_{Nk\sigma}(t)c_{Nk\sigma}(t) + V_k d_\sigma(t), \tag{A.102}$$

$$i\partial_t c^\dagger_{Nk\sigma}(t) = i[H(t), c^\dagger_{Nk\sigma}(t)] = -\varepsilon_{Nk\sigma}(t)c^\dagger_{Nk\sigma}(t) - V_k d^\dagger_\sigma(t), \tag{A.103}$$

which give us

$$(i\partial_t - \varepsilon_{Nk\sigma}(t))\, G^c_{c_{k\sigma},d^\dagger_{\sigma'}}(t,t') = V_k G^c_{d_\sigma,d^\dagger_{\sigma'}}(t,t'), \tag{A.104}$$

$$(i\partial_t + \varepsilon_{Nk\sigma}(t))\, G^c_{c^\dagger_{k\sigma},d^\dagger_{\sigma'}}(t,t') = -V_k G^c_{d^\dagger_\sigma,d^\dagger_{\sigma'}}(t,t'). \tag{A.105}$$

On the left side of (A.104) and (A.105) there appear the bare Green's functions of the normal lead electrons defined by

$$g^c_{c_{Nk\sigma},c^\dagger_{Nk\sigma'}}(t,t') = -i\langle \hat{T}_C\{c_{Nk\sigma}(t), c^\dagger_{Nk\sigma'}(t')\}\rangle, \tag{A.106}$$

$$g^c_{c^\dagger_{Nk\sigma},c_{Nk\sigma'}}(t,t') = -i\langle \hat{T}_C\{c^\dagger_{Nk\sigma}(t), c_{Nk\sigma'}(t')\}\rangle. \tag{A.107}$$

For the normal metallic lead Hamiltonian $\hat{H}_N = \sum_{k\sigma} \varepsilon_{Nk\sigma} c^\dagger_{Nk\sigma} c_{Nk\sigma}$ the bare Green's function obeys

$$(i\partial_t - \varepsilon_{Nk\sigma}(t)) g^c_{c_{Nk\sigma},c^\dagger_{Nk\sigma'}}(t,t') = \delta_c(t-t')\delta_{\sigma\sigma'}, \tag{A.108}$$

$$(i\partial_t + \varepsilon_{Nk\sigma}(t)) g^c_{c^\dagger_{Nk\sigma},c_{Nk\sigma'}}(t,t') = \delta_c(t-t')\delta_{\sigma\sigma'}. \tag{A.109}$$

Substituting (A.108) and (A.109) to Eqs.(A.104),(A.105), respectively, we obtain

$$G^c_{c_{Nk\sigma},d^\dagger_{\sigma'}}(t,t') = V_k \int_C d\tau\, g^c_{c_{Nk\sigma},c^\dagger_{Nk\sigma}}(t,\tau) G^c_{d_\sigma,d^\dagger_\sigma}(\tau,t'), \tag{A.110}$$

$$G^c_{c^\dagger_{Nk\sigma},d^\dagger_{\sigma'}}(t,t') = -V_k \int_C d\tau\, g^c_{c^\dagger_{Nk\sigma},c_{Nk\sigma}}(t,\tau) G^c_{d^\dagger_{\sigma'},d^\dagger_\sigma}(\tau,t'). \tag{A.111}$$

Quantum dot - superconductor interface

Below, we present the equation of motion for the contour-ordered Green's functions for the quantum dot coupled to the superconducting lead, described by Hamiltonian $\hat{H}_S = \sum_{q\sigma} \varepsilon_{Sq\sigma} c^\dagger_{Sq\sigma} c_{Sq\sigma} - \sum_q \Delta_{sc}\left(c^\dagger_{S-q\uparrow} c^\dagger_{Sq\downarrow} + h.c.\right)$

$$(i\partial_t - \varepsilon_{Sq})\, G^c_{c_{Sq\uparrow},d^\dagger_\uparrow}(t,t') = -\Delta_{sc} G^c_{c^\dagger_{S-q\downarrow},d^\dagger_\uparrow}(t,t') + V_q G^c_{d_\uparrow,d^\dagger_\uparrow}(t,t'), \tag{A.112}$$

$$(i\partial_t + \varepsilon_{Sq})\, G^c_{c^\dagger_{S-q\downarrow}, d^\dagger_\uparrow}(t,t') = -\Delta_{sc} G^c_{c_{Sq\uparrow}, d^\dagger_\uparrow}(t,t') - V_q G^c_{d^\dagger_\downarrow, d^\dagger_\uparrow}(t,t'). \tag{A.113}$$

This set of entangled functions comes from the solution of the equation of motion for operators

$$i\partial_t c_{Sq\sigma}(t) = \varepsilon_{Sq} c_{Sq\sigma}(t) + \delta_{\downarrow\sigma}\Delta_{sc} c^\dagger_{S-q\uparrow}(t) - \delta_{\uparrow\sigma}\Delta_{sc} c^\dagger_{S-q\downarrow}(t) + V_q d_\sigma(t), \tag{A.114}$$

$$i\partial_t c^\dagger_{S-q\sigma}(t) = -\varepsilon_{Sq} c^\dagger_{S-q\sigma}(t) - \delta_{\downarrow\sigma}\Delta_{sc} c_{Sq\uparrow}(t) + \delta_{\uparrow\sigma}\Delta_{sc} c_{Sq\downarrow}(t) - V_q d^\dagger_\sigma(t). \tag{A.115}$$

To solve functions presented in (A.112) and (A.113) we need a solution of the following bare Green's functions

$$i\partial_t g^c_{c_{Sq\uparrow}, c^\dagger_{Sq\uparrow}}(t,t') = \delta_c(t-t') - i\langle \hat{T}_C\{i\partial c_{Sq\sigma}(t), c^\dagger_{Sq\sigma'}(t')\}\rangle \tag{A.116}$$

$$i\partial_t g^c_{c_{Sq\uparrow}, c^\dagger_{Sq\uparrow}}(t,t') = \delta_c(t-t') - i\langle \hat{T}_C\{i\partial c_{Sq\sigma}(t), c^\dagger_{Sq\sigma'}(t')\}\rangle, \tag{A.117}$$

which give

$$(i\partial_t - \varepsilon_{Sq}) g^c_{c_{Sq\uparrow}, c^\dagger_{Sq\uparrow}}(t,t') = \delta_c(t-t') - \Delta_{sc} g^c_{c^\dagger_{S-q\downarrow}, c^\dagger_{Sq\uparrow}}(t,t'), \tag{A.118}$$

$$(i\partial_t + \varepsilon_{Sq}) g^c_{c^\dagger_{S-q\downarrow}, c^\dagger_{Sq\uparrow}}(t,t') = -\Delta_{sc} g^c_{c_{Sq\uparrow}, c^\dagger_{Sq\uparrow}}(t,t'). \tag{A.119}$$

Similarly, we can obtain a set of two equation for $g^c_{c_{Sq\downarrow}, c^\dagger_{Sq\downarrow}}(t,t')$. In such way, we can obtain other required bare Green's functions

$$\left((i\partial_t)^2 - E^2_{Sq}\right) g^c_{c^\dagger_{S-q\uparrow}, c^\dagger_{Sq\downarrow}}(t,t') = \Delta_{sc}\delta_c(t-t'), \tag{A.120}$$

$$\left((i\partial_t)^2 - E^2_{Sq}\right) g^c_{c^\dagger_{S-q\downarrow}, c^\dagger_{Sq\uparrow}}(t,t') = -\Delta_{sc}\delta_c(t-t'), \tag{A.121}$$

where $E^2_{Sq} = \varepsilon^2_{Sq} + \Delta^2_{sc}$.

Expressions for the bare Green's functions, (A.112) and (A.113) can be transformed as follow

$$\begin{aligned} G^c_{c_{Sq\uparrow}, d^\dagger_\uparrow}(t,t') = -V_q \int_C d\tau\, g^c_{c^\dagger_{S-q\uparrow}, c^\dagger_{Sq\downarrow}}(t,\tau) G^c_{d^\dagger_\downarrow, d^\dagger_\uparrow}(\tau,t') \\ + \int_C d\tau\, g^c_{c_{Sq\uparrow}, c^\dagger_{Sq\downarrow}}(t,\tau) V_q G^c_{d_\uparrow, d^\dagger_\uparrow}(\tau,t'), \end{aligned} \tag{A.122}$$

$$G^c_{c^\dagger_{Sq\downarrow},d^\dagger_\uparrow}(t,t') = -V_q \int_C d\tau g^c_{c^\dagger_{S-q\uparrow},c^\dagger_{Sq\downarrow}}(t,\tau) G^c_{d_\uparrow,d^\dagger_\uparrow}(\tau,t') \\ -V_q \int_C d\tau g^c_{c^\dagger_{Sq\downarrow},c_{Sq\uparrow}}(t,\tau) G^c_{d^\dagger_\downarrow,d^\dagger_\uparrow}(\tau,t'). \quad \text{(A.123)}$$

A.9 Contour ordered self energies

This appendix presents calculations of the self energies for electrodes. To solve the Green's function presented in (4.39) we need the self-energy functions in the Fourier representation.

We start from the self-energy of the normal metallic electrode

$$\Sigma^c_{c_{N\sigma},c^\dagger_{N\sigma}}(\tau,\tau') = \sum_k V_k^2 g^c_{c_{Nk\sigma},c^\dagger_{Nk\sigma}}(\tau,\tau'), \quad \text{(A.124)}$$

which can be Fourier transformed in (4.32) into the following form

$$\Sigma^{r,a}_{c_{N\sigma},c^\dagger_{N\sigma},nm}(\varepsilon) = \sum_k V_k^2 g^{r,a}_{c_{Nk\sigma},c^\dagger_{Nk\sigma},nm}(\varepsilon) = \sum_k V_k^2 \frac{\delta_{nm}}{\varepsilon \pm i0^+ + n\omega - \xi_k}, \quad \text{(A.125)}$$

where $\xi_k = \varepsilon_{Nk\sigma} - \varepsilon_F$ and ε_F is the Fermi level of the lead. By changing the summation over the momentum vector into integration we obtain

$$\Sigma^{r,a}_{c_{N\sigma},c^\dagger_{N\sigma},nm}(\varepsilon) = \int_{-\infty}^{\infty} d\xi_k \frac{V_k^2 \rho_k \delta_{nm}}{\varepsilon \pm i0^+ + n\omega - \xi_k \pm i\eta}, \quad \text{(A.126)}$$

where ρ_k is density of states of the electron in the metallic lead. Using the relationship for $\eta \to 0$

$$\lim_{\eta\to 0} \frac{1}{\varepsilon \pm i0^+ + n\omega - \xi_k \pm i\eta} = p.v. \mp i\pi\delta(\varepsilon \pm i0^+ + n\omega - \xi_k), \quad \text{(A.127)}$$

where $p.v.$ is the principal value, we get in the large bandwidth limit

$$\Sigma^{r,a}_{c_{N\sigma},c^\dagger_{N\sigma},nm}(\varepsilon) = \mp i\pi\delta_{nm} \int_{-\infty}^{\infty} d\xi_k V_k^2 \rho_k \delta(\varepsilon \pm i0^+ + n\omega - \xi_k). \quad \text{(A.128)}$$

Assuming constant coupling for every momentum vector k: $V_k = V_N$ and $\rho_k = \rho$, we obtain

$$\Sigma^{r,a}_{c_{N\sigma},c^\dagger_{N\sigma},nm}(\varepsilon) = \mp i\pi V_N^2 \rho \delta_{nm}. \quad \text{(A.129)}$$

In the wide-band limit approximation, we obtain the constant coupling defined by $\Gamma = 2\pi\rho V^2$, which finally gives us

$$\Sigma^{r,a}_{c_{N\sigma},c^\dagger_{N\sigma},nm}(\varepsilon) = \mp \frac{i\Gamma_N}{2}\delta_{nm}. \quad \text{(A.130)}$$

To find the self energies of the superconducting electrode, we start from

$$\Sigma^{c}_{c^{\dagger}_{S\uparrow},c^{\dagger}_{S\downarrow}}(\tau,\tau') = \sum_{q} V_q^2 g^{c}_{c^{\dagger}_{S-q\uparrow},c^{\dagger}_{Sq\downarrow}}(\tau,\tau'), \tag{A.131}$$

where the bare Green's function has the form

$$\left((i\partial_t)^2 - E_{Sq}^2\right) g^{c}_{c^{\dagger}_{S-q\uparrow},c^{\dagger}_{Sq\downarrow}}(t,t') = \Delta_{sc}\delta_c(t-t'). \tag{A.132}$$

From the double Fourier transform of (A.131) we obtain

$$\Sigma^{r,a}_{c^{\dagger}_{S\uparrow},c^{\dagger}_{S\downarrow},nm}(\varepsilon) = \sum_{q} V_q^2 g^{r,a}_{c^{\dagger}_{S-q\uparrow},c^{\dagger}_{Sq\downarrow},nm}(\varepsilon), \tag{A.133}$$

with

$$g^{r,a}_{c^{\dagger}_{S-q\uparrow},c^{\dagger}_{Sq\downarrow},nm}(\varepsilon) = \frac{\Delta_{sc}\delta_{nm}}{(\varepsilon \pm i0^{+} + n\omega)^2 - \xi_q^2 - \Delta_{sc}^2}. \tag{A.134}$$

By changing the summation over the momentum vector into integration, we obtain

$$\begin{aligned}
\Sigma^{r,a}_{c^{\dagger}_{S\uparrow},c^{\dagger}_{S\downarrow},nm}(\varepsilon) &= \int_{-\infty}^{\infty} d\xi_q V_q^2 \frac{\rho_q \Delta_{sc}\delta_{nm}}{(\varepsilon \pm i0^{+} + n\omega)^2 - \xi_q^2 - \Delta_{sc}^2} = \\
&= 2\Delta_{sc}\rho V_S^2 \int_{0}^{\infty} d\xi_q \frac{\delta_{nm}}{(\varepsilon \pm i0^{+} + n\omega)^2 - \xi_q^2 - \Delta_{sc}^2} \\
&= V_S^2 \pi \rho \Delta \frac{\delta_{nm}\left[\Theta(\Delta_{sc} - |\varepsilon + n\omega|) \mp i\,\mathrm{sign}(\varepsilon + n\omega)\Theta(|\varepsilon + n\omega| - \Delta_{sc})\right]}{\sqrt{|(\varepsilon \pm i0^{+} + n\omega)^2 - \Delta_{sc}^2|}}.
\end{aligned} \tag{A.135}$$

In the wide-band limit approximation we obtain the off-diagonal self-energy

$$\Sigma^{r,a}_{c^{\dagger}_{S\uparrow},c^{\dagger}_{S\downarrow},nm}(\varepsilon) = \frac{\Gamma_S \Delta_{sc}}{2} \frac{\delta_{nm}\left[\Theta(\Delta_{sc} - |\varepsilon + n\omega|) \mp i\,\mathrm{sign}(\varepsilon + n\omega)\Theta(|\varepsilon + n\omega| - \Delta_{sc})\right]}{\sqrt{|(\varepsilon \pm i0^{+} + n\omega)^2 - \Delta_{sc}^2|}}. \tag{A.136}$$

In similar way, we can obtain the diagonal self-energy of (4.41). We use the Fourier transformation of $g^{c}_{c_{Sq\downarrow},c^{\dagger}_{Sq\downarrow}}(t,t')$

$$\Sigma^{r,a}_{c_{S\downarrow},c^{\dagger}_{S\downarrow},nm}(\varepsilon) = \sum_{q} V_q^2 g^{r,a}_{c_{Sq\downarrow},c^{\dagger}_{Sq\downarrow},nm}(\varepsilon), \tag{A.137}$$

with

$$g^{r,a}_{c_{Sq\downarrow},c^{\dagger}_{Sq\downarrow},nm}(\varepsilon) = \frac{(\varepsilon + n\omega)\delta_{nm}}{(\varepsilon \pm i0^{+} + n\omega)^2 - \xi_q^2 - \Delta_{sc}^2}. \tag{A.138}$$

Again changing the summation over the momentum vector into integration, we get

$$\begin{aligned}\Sigma^{r,a}_{c_{S\downarrow},c^{\dagger}_{S\downarrow},nm}(\varepsilon) &= \int_{-\infty}^{\infty} d\xi_q V_q^2 \frac{\rho_q(\varepsilon+n\omega)\delta_{nm}}{(\varepsilon \pm i0^{+} + n\omega)^2 - \xi_q^2 - \Delta_{sc}^2} = \\ &= 2\rho V_S^2 \int_0^{\infty} d\xi_q \frac{(\varepsilon+n\omega)\delta_{nm}}{(\varepsilon \pm i0^{+} + n\omega)^2 - \xi_q^2 - \Delta_{sc}^2} \\ &= -V_S^2 \pi \rho(\varepsilon+n\omega) \frac{\delta_{nm}\left[\Theta(\Delta_{sc} - |\varepsilon+n\omega|) \mp i\,\mathrm{sign}(\varepsilon+n\omega)\Theta(|\varepsilon+n\omega| - \Delta_{sc})\right]}{\sqrt{|(\varepsilon \pm i0^{+} + n\omega)^2 - \Delta_{sc}^2|}}.\end{aligned} \tag{A.139}$$

In the wide-band limit approximation the diagonal part of self-energy takes the following form

$$\Sigma^{r,a}_{c_{S\downarrow},c^{\dagger}_{S\downarrow},nm}(\varepsilon) = \frac{-\Gamma_S(\varepsilon+n\omega)}{2} \frac{\delta_{nm}\left[\Theta(\Delta_{sc} - |\varepsilon+n\omega|) \mp i\,\mathrm{sign}(\varepsilon+n\omega)\Theta(|\varepsilon+n\omega| - \Delta_{sc})\right]}{\sqrt{|(\varepsilon \pm i0^{+} + n\omega)^2 - \Delta_{sc}^2|}}. \tag{A.140}$$

Appendix B

List of published articles

1. *Subgap dynamics of double quantum dot coupled between superconducting and normal leads,* **B. Baran** , R. Taranko, T. Domański, Scientific Reports 11, 11148, 2021

2. *Transient effects in a double quantum dot sandwiched laterally between superconducting and metallic leads,* R. Taranko, K. Wrześniewski, **B. Baran** , I. Weymann, T. Domański, Phys. Rev. B 103, 165430, 2021

3. *Quench dynamics of a correlated quantum dot sandwiched between normal-metal and superconducting leads,* K. Wrześniewski, **B. Baran** , R. Taranko, T. Domański, I. Weymann, Phys. Rev. B 103, 155420, 2021

4. *Post-quench Dynamics of Quantum Dot Proximitized to Superconducting Lead,* **B. Baran** , R. Taranko, T. Domański, Acta Phys. Polon. A 138,691, 2020

5. *Quasiparticles of a driven quantum dot coupled between superconducting and normal leads,* **B. Baran** and T. Domański, Phys. Rev. B 100, 085414, 2019

Bibliography

[1] P.W. Anderson. Theory of dirty superconductors. *Journal of Physics and Chemistry of Solids*, 11(1):26–30, 1959.

[2] A. V. Balatsky, I. Vekhter, and Jian-Xin Zhu. Impurity-induced states in conventional and unconventional superconductors. *Rev. Mod. Phys.*, 78:373–433, May 2006.

[3] A A Abrikosov. Magnetic Impurities In Nonmagnetic Me. *Soviet Physics Uspekhi*, 12(2):168–181, feb 1969.

[4] H. Shiba. Classical spins in superconductors. *Prog. Theor. Phys.*, 40:435, 1968.

[5] H. Shiba and T. Soda. Superconducting tunneling through the barrier with paramagnetic impurities. *Prog. Theor. Phys.*, 41:25, 1969.

[6] A. I. Rusinov. Superconductivity on the border of itinerant-electron ferromagnetism in UGe2. *Sov. Phys.—JETP*, 56:2047, 1969.

[7] A. F. Andreev. The thermal conductivity of the intermediate state in superconductors. *Sov. Phys. JETP*, 19:1228 – 1231, Nov 1964.

[8] Ekimov A.I. and Onushchenko A.A. Quantum size effect in three-dimensional microscopic semiconductor crystals. *Soviet Journal of Experimental and Theoretical Physics Letters*, 34:345, September 1981.

[9] Brus L. E. A simple model for the ionization potential, electron affinity, and aqueous redox potentials of small semiconductor crystallites. *The Journal of Chemical Physics*, 79(11):5566–5571, 1983.

[10] Brus L.E. Electron-electron and electron-hole interactions in small semiconductor crystallites: The size dependence of the lowest excited electronic state. *Journal of Chemical Physics*, 80(9):4403–4409, May 1984.

[11] M. A. Reed, R. T. Bate, K. Bradshaw, W. M. Duncan, W. R. Frensley, J. W. Lee, and H. D. Shih. Spatial quantization in GaAs–AlGaAs multiple quantum dots. *Journal of Vacuum Science & Technology B: Microelectronics Processing and Phenomena*, 4(1):358–360, 1986.

[12] M. A. Reed, J. N. Randall, R. J. Aggarwal, R. J. Matyi, T. M. Moore, and A. E. Wetsel. Observation of discrete electronic states in a zero-dimensional semiconductor nanostructure. *Phys. Rev. Lett.*, 60:535–537, Feb 1988.

[13] K. Kash, A. Scherer, J. M. Worlock, H. G. Craighead, and M. C. Tamargo. Optical spectroscopy of ultrasmall structures etched from quantum wells. *Applied Physics Letters*, 49(16):1043–1045, 1986.

[14] H. Temkin, G. J. Dolan, M. B. Panish, and S. N. G. Chu. Low-temperature photoluminescence from InGaAs/InP quantum wires and boxes. *Applied Physics Letters*, 50(7):413–415, February 1987.

[15] I. Stranski and L. Krastanow. Zur theorie der orientierten Ausscheidung von Ionenkristallen aufeinander. *Monatshefte für Chemie und verwandte Teile anderer Wissenschaften*, 71:351–364, 1937.

[16] J. M. Gerard, J. B. Genin, J. Lefebvre, J. Y. Marzin, D. Barrier, and J. M. Moison. *Nucleation and Growth of InAs Islands on GaAs: An Optical Study*, pages 35–48. Springer Netherlands, Dordrecht, 1995.

[17] Marc Bockrath, David H. Cobden, Paul L. McEuen, Nasreen G. Chopra, A. Zettl, Andreas Thess, and R. E. Smalley. Single-electron transport in ropes of carbon nanotubes. *Science*, 275(5308):1922–1925, 1997.

[18] N. Mason, M. J. Biercuk, and C. M. Marcus. Local gate control of a carbon nanotube double quantum dot. *Science*, 303(5658):655–658, 2004.

[19] Jeffrey M. Pietryga, Young-Shin Park, Jaehoon Lim, Andrew F. Fidler, Wan Ki Bae, Sergio Brovelli, and Victor I. Klimov. Spectroscopic and device aspects of nanocrystal quantum dots. *Chemical Reviews*, 116(18):10513–10622, 2016. PMID: 27677521.

[20] Dong Pan, Elias Towe, and Steve Kennerly. Normal-incidence intersubband (In, Ga)As/GaAs quantum dot infrared photodetectors. *Applied Physics Letters*, 73(14):1937–1939, 1998.

[21] L. Bakueva, S. Musikhin, M. A. Hines, T.-W. F. Chang, M. Tzolov, G. D. Scholes, and E. H. Sargent. Size-tunable infrared (1000–1600 nm) electroluminescence from PbS quantum-dot nanocrystals in a semiconducting polymer. *Applied Physics Letters*, 82(17):2895–2897, 2003.

[22] N. H. Bonadeo, J. Erland, D. Gammon, D. Park, D. S. Katzer, and D. G. Steel. Coherent optical control of the quantum state of a single quantum dot. *Science*, 282(5393):1473–1476, 1998.

[23] David P. DiVincenzo. Quantum computation. *Science*, 270(5234):255–261, 1995.

[24] Mete Atatüre, Jan Dreiser, Antonio Badolato, Alexander Högele, Khaled Karrai, and Atac Imamoglu. Quantum-dot spin-state preparation with near-unity fidelity. *Science*, 312(5773):551–553, 2006.

[25] S. Stufler et al. A. Zrenner, E. Beham. Coherent properties of a two-level system based on a quantum-dot photodiode. *Nature*, 418:612–614, 2002.

[26] L. Willems van Beveren et al. J. Elzerman, R. Hanson. Single-shot read-out of an individual electron spin in a quantum dot. *Nature*, 430:431–435, 2004.

[27] H. Kamada, H. Gotoh, J. Temmyo, T. Takagahara, and H. Ando. Exciton Rabi oscillation in a single quantum dot. *Phys. Rev. Lett.*, 87:246401, Nov 2001.

[28] Xiaoqin Li, Yanwen Wu, Duncan Steel, D. Gammon, T. H. Stievater, D. S. Katzer, D. Park, C. Piermarocchi, and L. J. Sham. An all-optical quantum gate in a semiconductor quantum dot. *Science*, 301(5634):809–811, 2003.

[29] A. Zazunov, V. S. Shumeiko, E. N. Bratus', J. Lantz, and G. Wendin. Andreev level qubit. *Phys. Rev. Lett.*, 90:087003, Feb 2003.

[30] Nikolai M. Chtchelkatchev and Yu. V. Nazarov. Andreev quantum dots for spin manipulation. *Phys. Rev. Lett.*, 90:226806, Jun 2003.

[31] C. Padurariu and Yu. V. Nazarov. Theoretical proposal for superconducting spin qubits. *Phys. Rev. B*, 81:144519, Apr 2010.

[32] R. Aguado. A perspective on semiconductor-based superconducting qubits. *Appl. Phys. Lett.*, 117(24):240501, 2020.

[33] T. Hyart, B. van Heck, I. C. Fulga, M. Burrello, A. R. Akhmerov, and C. W. J. Beenakker. Flux-controlled quantum computation with Majorana fermions. *Phys. Rev. B*, 88:035121, Jul 2013.

[34] E. Prada, P. San-Jose, M.W.A. de Moor, A. Geresdi, E.J.H. Lee, J. Klinovaja, D. Loss, J. Nygå rd, R. Aguado, and L.P. Kouwenhoven. From Andreev to Majorana bound states in hybrid superconductor-semiconductor nanowires. *Nat. Rev. Phys.*, 2:575, Oct 2020.

[35] I. Chiorescu, Y. Nakamura, C. J. P. M. Harmans, and J. E. Mooij. Coherent quantum dynamics of a superconducting flux qubit. *Science*, 299(5614):1869–1871, 2003.

[36] T. W. Larsen, K. D. Petersson, F. Kuemmeth, T. S. Jespersen, P. Krogstrup, J. Nygård, and C. M. Marcus. Semiconductor-nanowire-based superconducting qubit. *Phys. Rev. Lett.*, 115:127001, Sep 2015.

[37] G. de Lange, B. van Heck, A. Bruno, D. J. van Woerkom, A. Geresdi, S. R. Plissard, E. P. A. M. Bakkers, A. R. Akhmerov, and L. DiCarlo. Realization of microwave quantum circuits using hybrid superconducting-semiconducting nanowire josephson elements. *Phys. Rev. Lett.*, 115:127002, Sep 2015.

[38] Martin Leijnse and Karsten Flensberg. Introduction to topological superconductivity and Majorana fermions. *Semiconductor Science and Technology*, 27(12):124003, Nov 2012.

[39] Jason Alicea. New directions in the pursuit of Majorana fermions in solid state systems. *Reports on Progress in Physics*, 75(7):076501, Jun 2012.

[40] C.W.J. Beenakker. Search for Majorana fermions in superconductors. *Annual Review of Condensed Matter Physics*, 4(1):113–136, 2013.

[41] Li Dai, Watson Kuo, and Ming-Chiang Chung. Extracting entangled qubits from Majorana fermions in quantum dot chains through the measurement of parity. *Scientific Reports*, 5(1):11188, Jun 2015.

[42] Maciej M. Maśka and Tadeusz Domański. Polarization of the Majorana quasiparticles in the rashba chain. *Scientific Reports*, 7(1):16193, Nov 2017.

[43] D. Sherman, J.S. Yodh, S.M. Albrecht, J. Nygård, P. Krogstrup, and C.M. Marcus. Normal, superconducting and topological regimes of hybrid double quantum dots. *Nature Nanotechnol.*, 12:212, 2017.

[44] Daniël Bouman, Ruben J. J. van Gulik, Gorm Steffensen, Dávid Pataki, Péter Boross, Peter Krogstrup, Jesper Nygård, Jens Paaske, András Pályi, and Attila Geresdi. Triplet-blockaded Josephson supercurrent in double quantum dots. *Phys. Rev. B*, 102:220505, Dec 2020.

[45] J. C. Estrada Saldaña, A. Vekris, G. Steffensen, R. Žitko, P. Krogstrup, J. Paaske, K. Grove-Rasmussen, and J. Nygård. Supercurrent in a double quantum dot. *Phys. Rev. Lett.*, 121:257701, Dec 2018.

[46] J. C. Estrada Saldaña, A. Vekris, R. Žitko, G. Steffensen, P. Krogstrup, J. Paaske, K. Grove-Rasmussen, and J. Nygård. Two-impurity Yu-Shiba-Rusinov states in coupled quantum dots. *Phys. Rev. B*, 102:195143, Nov 2020.

[47] Z. Su, A.B. Tacla, M. Hocevar, D. Car, S.R. Plissard, E.P.A.M. Bakkers, A.J. Daley, D. Pekker, and S.M. Frolov. Andreev molecules in semiconductor nanowire double quantum dots. *Nature Commun.*, 8:585, 2017.

[48] A. Zarassi, Z. Su, J. Danon, J. Schwenderling, M. Hocevar, B. M. Nguyen, J. Yoo, S. A. Dayeh, and S. M. Frolov. Magnetic field evolution of spin

blockade in Ge/Si nanowire double quantum dots. *Phys. Rev. B*, 95:155416, Apr 2017.

[49] J.-P. Cleuziou, W. Wernsdorfer, V. Bouchiat, T. Ondarcuhu, and M. Monthioux. Carbon nanotube superconducting quantum interference device. *Nature Nanotechnol.*, 1:53, 2006.

[50] J.-D. Pillet, P. Joyez, Rok Žitko, and M. F. Goffman. Tunneling spectroscopy of a single quantum dot coupled to a superconductor: From Kondo ridge to Andreev bound states. *Phys. Rev. B*, 88:045101, Jul 2013.

[51] Johannes Bauer, Jose I. Pascual, and Katharina J. Franke. Microscopic resolution of the interplay of Kondo screening and superconducting pairing: Mn-phthalocyanine molecules adsorbed on superconducting Pb(111). *Phys. Rev. B*, 87:075125, Feb 2013.

[52] M. Ruby, B.W. Heinrich, Y. Peng, F. von Oppen, and K.J. Franke. Wavefunction hybridization in Yu-Shiba-Rusinov dimers. *Phys. Rev. Lett.*, 120:156803, Apr 2018.

[53] B.W. Heinrich, J.I. Pascual, and K.J. Franke. Single magnetic adsorbates on s-wave superconductors. *Prog. Surf. Science*, 93(1):1, 2018.

[54] D.-J. Choi, C.G. Fernández, E. Herrera, C. Rubio-Verdú, M.M. Ugeda, I. Guillamón, H. Suderow, J.I. Pascual, and N. Lorente. Influence of magnetic ordering between Cr adatoms on the Yu-Shiba-Rusinov states of the β–Bi_2Pd superconductor. *Phys. Rev. Lett.*, 120:167001, Apr 2018.

[55] S. Kezilebieke, R. Žitko, M. Dvorak, and P. Liljeroth. Observation of coexistence of Yu-Shiba-Rusinov states and spin-flip excitations. *Nano Lett.*, 19:4614, 2019.

[56] Emir G. Emiroglu, David G. Hasko, and David A. Williams. Isolated double quantum dot capacitively coupled to a single quantum dot single-electron transistor in silicon. *Applied Physics Letters*, 83(19):3942–3944, 2003.

[57] J. Gorman, D. G. Hasko, and D. A. Williams. Charge-qubit operation of an isolated double quantum dot. *Phys. Rev. Lett.*, 95:090502, Aug 2005.

[58] R. Hanson, L. P. Kouwenhoven, J. R. Petta, S. Tarucha, and L. M. K. Vandersypen. Spins in few-electron quantum dots. *Rev. Mod. Phys.*, 79:1217–1265, Oct 2007.

[59] David P. DiVincenzo. Double quantum dot as a quantum bit. *Science*, 309(5744):2173–2174, 2005.

[60] Y. Tanaka, N. Kawakami, and A. Oguri. Correlated electron transport through double quantum dots coupled to normal and superconducting leads. *Phys. Rev. B*, 81:075404, Feb 2010.

[61] A. Martín-Rodero and A. Levy Yeyati. Josephson and Andreev transport through quantum dots. *Advances in Physics*, 60(6):899–958, 2011.

[62] R. Žitko. Numerical subgap spectroscopy of double quantum dots coupled to superconductors. *Phys. Rev. B*, 91:165116, Apr 2015.

[63] K. Grove-Rasmussen, G. Steffensen, A. Jellinggaard, M.H. Madsen, R. Žitko, J. Paaske, and J. Nygård. Yu-Shiba-Rusinov screening of spins in double quantum dots. *Nature Commun.*, 9:2376, 2018.

[64] Po Zhang, Hao Wu, Jun Chen, Sabbir A. Khan, Peter Krogstrup, David Pekker, and Sergey M. Frolov. Evidence of Andreev blockade in a double quantum dot coupled to a superconductor, 2021.

[65] Qing-feng Sun, Jian Wang, and Tsung-han Lin. Resonant Andreev reflection in a normal-metal–quantum-dot–superconductor system. *Phys. Rev. B*, 59:3831–3840, Feb 1999.

[66] Q.-F. Sun, J. Wang, and T.-H. Lin. Photon-assisted Andreev tunneling through a mesoscopic hybrid system. *Phys. Rev. B*, 59:13126, May 1999.

[67] Y. Xing, Q.-F. Sun, and J. Wang. Response time of a normal-metal/superconductor hybrid system under a step-like pulse bias. *Phys. Rev. B*, 75:125308, Mar 2007.

[68] N. W. Hendrickx, M. L. V. Tagliaferri, M. Kouwenhoven, R. Li, D. P. Franke, A. Sammak, A. Brinkman, G. Scappucci, and M. Veldhorst. Ballistic supercurrent discretization and micrometer-long Josephson coupling in germanium. *Phys. Rev. B*, 99:075435, Feb 2019.

[69] P. Kot, R. Drost, M. Uhl, J. Ankerhold, J.C. Cuevas, and C.R. Ast. Microwave-assisted tunneling and interference effects in superconducting junctions under fast driving signals. *Phys. Rev. B*, 101:134507, Apr 2020.

[70] S.A. González, L. Melischek, O. Peters, K. Flensberg, K.J. Franke, and F. von Oppen. Photon-assisted resonant Andreev reflections: Yu-Shiba-Rusinov and Majorana states. *Phys. Rev. B*, 102:045413, Jul 2020.

[71] H. Kamerlingh Onnes. Further experiments with liquid helium on the electrical resistance of pure metals on the sudden change in the rate at which the resistance of mercury disappears. *Comm. Phys. Lab. Univ. Leiden*, No. 124c, 1911.

[72] W. Meissner and R. Ochsenfeld. Ein neuer Effekt bei Eintritt der Supraleitfähigkeit. *Naturwissenschaften*, 21:787–788, 1933.

[73] J. B. Ketterson and S. N. Song. *Superconductivity.* Cambridge University Press, 1999.

[74] M. Tinkham. *Introduction to Superconductivity.* Dover Publications, 2 edition, June 2004.

[75] C. Timm. *Theory of Superconductivity.* TU Dresden, 2020.

[76] Leon N. Cooper. Bound electron pairs in a degenerate Fermi gas. *Phys. Rev.*, 104:1189–1190, Nov 1956.

[77] J. Bardeen, L. N. Cooper, and J. R. Schrieffer. Microscopic theory of superconductivity. *Phys. Rev.*, 106:162–164, Apr 1957.

[78] K. Ahilan et al. S. Saxena, P. Agarwal. Superconductivity on the border of itinerant-electron ferromagnetism in UGe2. *Nature*, 406:587–592, 2000.

[79] N. I. Karchev, K. B. Blagoev, K. S. Bedell, and P. B. Littlewood. Coexistence of superconductivity and ferromagnetism in ferromagnetic metals. *Phys. Rev. Lett.*, 86:846–849, Jan 2001.

[80] Richard A. Fulde, Peter; Ferrell. Superconductivity in a strong spin-exchange field. *Phys. Rev. 135*, A550, 1964.

[81] Richard A. Fulde, Peter; Ferrell. Inhomogeneous state of superconductors. *Sov. Phys. JETP*, 20, 1965.

[82] Yuji Matsuda and Hiroshi Shimahara. Fulde–Ferrell–Larkin–Ovchinnikov state in heavy fermion superconductors. *Journal of the Physical Society of Japan*, 76(5):051005, 2007.

[83] Elliot Snider, Nathan Dasenbrock-Gammon, Raymond McBride, Mathew Debessai, Hiranya Vindana, Kevin Vencatasamy, Keith V. Lawler, Ashkan Salamat, and Ranga P. Dias. Room-temperature superconductivity in a carbonaceous sulfur hydride. *Nature*, 586 7829:373–377, 2020.

[84] H. Ding, M. R. Norman, J. C. Campuzano, M. Randeria, A. F. Bellman, T. Yokoya, T. Takahashi, T. Mochiku, and K. Kadowaki. Angle-resolved photoemission spectroscopy study of the superconducting gap anisotropy in $\mathrm{bi_2sr_2Cacu_2o_{8+x}}$. *Phys. Rev. B*, 54:R9678–R9681, Oct 1996.

[85] S. Guéron, H. Pothier, Norman O. Birge, D. Esteve, and M. H. Devoret. Superconducting proximity effect probed on a mesoscopic length scale. *Phys. Rev. Lett.*, 77:3025–3028, Sep 1996.

[86] W. Belzig, C. Bruder, and Gerd Schön. Local density of states in a dirty normal metal connected to a superconductor. *Phys. Rev. B*, 54:9443–9448, Oct 1996.

[87] P. Charlat, H. Courtois, Ph. Gandit, D. Mailly, A. F. Volkov, and B. Pannetier. Reentrance of the metallic conductance in a mesoscopic proximity superconductor. *Phys. Rev. Lett.*, 77:4950–4953, Dec 1996.

[88] S. G. Lachenmann, I. Friedrich, A. Förster, D. Uhlisch, and A. A. Golubov. Charge transport in superconductor/semiconductor/normal-conductor step junctions. *Phys. Rev. B*, 56:14108–14115, Dec 1997.

[89] L.D. Landau V.L. Ginzburg. On the theory of superconductivity. *Zh. Eksp.Teor. Fiz.*, 20:1064–1082, 1950.

[90] P. A. M. Benistant, H. van Kempen, and P. Wyder. Direct observation of Andreev reflection. *Phys. Rev. Lett.*, 51:817–820, Aug 1983.

[91] B.D. Josephson. Possible new effects in superconductive tunnelling. *Physics Letters*, 1(7):251–253, 1962.

[92] P. G. De Gennes. Boundary effects in superconductors. *Rev. Mod. Phys.*, 36:225–237, Jan 1964.

[93] Teun M. Klapwijk. Proximity effect from an Andreev perspective. *Journal of Superconductivity*, 17:593–611, 2004.

[94] G. E. Blonder, M. Tinkham, and T. M. Klapwijk. Transition from metallic to tunneling regimes in superconducting microconstrictions: Excess current, charge imbalance, and supercurrent conversion. *Phys. Rev. B*, 25:4515–4532, Apr 1982.

[95] Elsa Prada, Pablo San-Jose, Michiel W. A. de Moor, Attila Geresdi, Eduardo J H Lee, Jelena Klinovaja, Daniel Loss, Jesper Nygård, Ramón Aguado, and L. P. Kouwenhoven. From Andreev to Majorana bound states in hybrid superconductor–semiconductor nanowires. *Nature Reviews Physics*, pages 1–20, 2019.

[96] C. W. J. Beenakker. Three "universal" mesoscopic Josephson effects. In Hidetoshi Fukuyama and Tsuneya Ando, editors, *Transport Phenomena in Mesoscopic Systems*, pages 235–253, Berlin, Heidelberg, 1992. Springer Berlin Heidelberg.

[97] C. W. J. Beenakker. Quantum transport in semiconductor-superconductor microjunctions. *Phys. Rev. B*, 46:12841–12844, Nov 1992.

[98] Rolf Landauer. Can a length of perfect conductor have a resistance? *Physics Letters A*, 85(2):91–93, 1981.

[99] H. (Hidetoshi) Fukuyama and Tsuneya Andō. *Transport phenomena in mesoscopic systems : proceedings of the 14th Taniguchi symposium, Shima, Japan, November 10-14, 1991 / H. Fukuyama, T. Ando.* Springer series in solid-state sciences ; 109. Springer-Verlag, Berlin ; New York, 1992.

[100] Liang Fu and C. L. Kane. Superconducting proximity effect and Majorana fermions at the surface of a topological insulator. *Phys. Rev. Lett.*, 100:096407, Mar 2008.

[101] Tobias Meng, Serge Florens, and Pascal Simon. Self-consistent description of Andreev bound states in Josephson quantum dot devices. *Phys. Rev. B*, 79:224521, Jun 2009.

[102] A. I. Buzdin. Proximity effects in superconductor-ferromagnet heterostructures. *Rev. Mod. Phys.*, 77:935–976, Sep 2005.

[103] Piotr Magierski, Bu ğra Tüzemen, and Gabriel Wlazłowski. Spin-polarized droplets in the unitary Fermi gas. *Phys. Rev. A*, 100:033613, Sep 2019.

[104] G. A. Bobkov, I. V. Bobkova, and A. M. Bobkov. Long-range interaction of magnetic moments in a coupled system of superconductor-ferromagnet-superconductor josephson junctions with anomalous ground-state phase shift. *Phys. Rev. B*, 105:024513, Jan 2022.

[105] L. Hofstetter, S. Csonka, J. Nygård, and C. Schönenberger. Cooper pair splitter realized in a two-quantum-dot Y-junction. *Nature*, 461:1476, Oct 2009.

[106] Piotr Trocha and Kacper Wrześniewski. Cross-correlations in a quantum dot cooper pair splitter with ferromagnetic leads. *Journal of Physics: Condensed Matter*, 30(30):305303, jul 2018.

[107] Bogdan R. Bułka. Coherent current correlations in a double-dot cooper pair splitter. *Phys. Rev. B*, 104:155410, Oct 2021.

[108] Fredrik Brange, Kacper Prech, and Christian Flindt. Dynamic Cooper Pair Splitter. *Phys. Rev. Lett.*, 127:237701, Dec 2021.

[109] T. Dirks, Taylor L. Hughes, Siddhartha Lal, Bruno Uchoa, Yung fu Chen, Cesar E Chialvo, Paul M. Goldbart, and Nadya Mason. Transport through Andreev bound states in a graphene quantum dot. *Nature Physics*, 7:386–390, 2011.

[110] K. Wrześniewski, B. Baran, R. Taranko, T. Domański, and I. Weymann. Quench dynamics of a correlated quantum dot sandwiched between normal-metal and superconducting leads. *Phys. Rev. B*, 103:155420, Apr 2021.

[111] J Bauer, A Oguri, and A C Hewson. Spectral properties of locally correlated electrons in a Bardeen-Cooper-Schrieffer superconductor. *Journal of Physics: Condensed Matter*, 19(48):486211, nov 2007.

[112] G. Michałek, B. R. Bułka, T. Domański, and K. I. Wysokiński. Statistical correlations of currents flowing through a proximized quantum dot. *Phys. Rev. B*, 101:235402, Jun 2020.

[113] Benjamin W. Heinrich, Jose I. Pascual, and Katharina J. Franke. Single magnetic adsorbates on s-wave superconductors. *Progress in Surface Science*, 93(1):1–19, 2018.

[114] J. Gramich, A. Baumgartner, and C. Schönenberger. Andreev bound states probed in three-terminal quantum dots. *Phys. Rev. B*, 96:195418, Nov 2017.

[115] Eduardo J H Lee, Xiaocheng Jiang, Manuel Houzet, Ramón Aguado, Charles M. Lieber, and Silvano de Franceschi. Spin-resolved Andreev levels and parity crossings in hybrid superconductor-semiconductor nanostructures. *Nature nanotechnology*, 9 1:79–84, 2014.

[116] Antti-Pekka Jauho, Ned S. Wingreen, and Yigal Meir. Time-dependent transport in interacting and noninteracting resonant-tunneling systems. *Phys. Rev. B*, 50:5528–5544, Aug 1994.

[117] R. Taranko and T. Domański. Buildup and transient oscillations of Andreev quasiparticles. *Phys. Rev. B*, 98:075420, Aug 2018.

[118] R. Taranko, T. Kwapiński, and T. Domański. Transient dynamics of a quantum dot embedded between two superconducting leads and a metallic reservoir. *Phys. Rev. B*, 99:165419, Apr 2019.

[119] T. Domański B. Baran, R. Taranko. Postquench dynamics of quantum dot proximitized to superconducting lead. *Acta Phys. Polon. A*, 138, 2020.

[120] Fabrício M. Souza. Spin-dependent ringing and beats in a quantum dot system. *Phys. Rev. B*, 76:205315, Nov 2007.

[121] E. Perfetto, G. Stefanucci, and M. Cini. Spin-flip scattering in time-dependent transport through a quantum dot: Enhanced spin-current and inverse tunneling magnetoresistance. *Phys. Rev. B*, 78:155301, Oct 2008.

[122] E. Taranko, M. Wiertel, and R. Taranko. Transient electron transport properties of multiple quantum dots systems. *J. Appl. Phys.*, 111(2):023711, 2012.

[123] A. Kadlecová, M. Žonda, V. Pokorný, and T. Novotný. Practical guide to quantum phase transitions in quantum-dot-based tunable Josephson junctions. *Phys. Rev. Applied*, 11:044094, Apr 2019.

[124] V. Meden. The Anderson–Josephson quantum dot—a theory perspective. *J. Phys.: Condens. Matter*, 31(16):163001, feb 2019.

[125] J. Bauer, A. Oguri, and A. C. Hewson. Spectral properties of locally correlated electrons in a Bardeen-Cooper-Schrieffer superconductor. *J. Phys.: Condens. Matter*, 19(48):486211, 2007.

[126] Jon H. Shirley. Solution of the Schrödinger equation with a Hamiltonian periodic in time. *Phys. Rev.*, 138:B979–B987, May 1965.

[127] André Eckardt and Egidijus Anisimovas. High-frequency approximation for periodically driven quantum systems from a Floquet-space perspective. *New Journal of Physics*, 17(9):093039, sep 2015.

[128] Tobias Brandes. Truncation method for Green's functions in time-dependent fields. *Phys. Rev. B*, 56:1213–1224, Jul 1997.

[129] Naoto Tsuji, Takashi Oka, and Hideo Aoki. Correlated electron systems periodically driven out of equilibrium: Floquet + DMFT formalism. *Phys. Rev. B*, 78:235124, Dec 2008.

[130] Götz S. Uhrig, Mona H. Kalthoff, and James K. Freericks. Positivity of the spectral densities of retarded Floquet green functions. *Phys. Rev. Lett.*, 122:130604, Apr 2019.

[131] A.-P. Jauho, N. S. Wingreen, and Y. Meir. Time-dependent transport in interacting and noninteracting resonant-tunneling systems. *Phys. Rev. B*, 50:5528, Aug 1994.

[132] Jian Wang, Baigeng Wang, Wei Ren, and Hong Guo. Conservation of spin current: Model including self-consistent spin-spin interaction. *Phys. Rev. B*, 74:155307, Oct 2006.

[133] Marin Bukov, Luca D'Alessio, and Anatoli Polkovnikov. Universal high-frequency behavior of periodically driven systems: from dynamical stabilization to Floquet engineering. *Advances in Physics*, 64(2):139–226, 2015.

[134] T. Domański B. Baran, R. Taranko. Subgap dynamics of double quantum dot coupled between superconducting and normal leads. *Scientific Reports*, 11, 05 2021.

[135] Z. Scherübl, A. Pályi, and S. Csonka. Transport signatures of an Andreev molecule in a quantum dot-superconductor-quantum dot setup. *Beilstein J. Nanotechnol.*, 10:363, Feb 2019.

[136] Wilfred G. van der Wiel, Toshimasa Fujisawa, Seigo Tarucha, and Leo P. Kouwenhoven. A double quantum dot as an artificial two-level system. *Japanese Journal of Applied Physics*, 40(Part 1, No. 3B):2100–2104, Mar 2001.

[137] Oleg N. Jouravlev and Yuli V. Nazarov. Electron transport in a double quantum dot governed by a nuclear magnetic field. *Phys. Rev. Lett.*, 96:176804, May 2006.

[138] Hao Zheng, Junyi Zhang, and Richard Berndt. A minimal double quantum dot. *Scientific Reports*, 7(1):10764, Sep 2017.

[139] Zhaoen Su, Alexandre B. Tacla, Moïra Hocevar, Diana Car, Sébastien R. Plissard, Erik P. A. M. Bakkers, Andrew J. Daley, David Pekker, and Sergey M. Frolov. Andreev molecules in semiconductor nanowire double quantum dots. *Nature Communications*, 8(1):585, Sep 2017.

[140] Patrik Recher, Eugene V. Sukhorukov, and Daniel Loss. Andreev tunneling, coulomb blockade, and resonant transport of nonlocal spin-entangled electrons. *Phys. Rev. B*, 63:165314, Apr 2001.

[141] David Pekker, Po Zhang, and Sergey M. Frolov. Theory of Andreev Blockade in a Double Quantum Dot with a Superconducting Lead. *SciPost Phys.*, 11:81, 2021.

[142] R. Taranko, K. Wrześniewski, B. Baran, I. Weymann, and T. Domański. Transient effects in a double quantum dot sandwiched laterally between superconducting and metallic leads. *Phys. Rev. B*, 103:165430, Apr 2021.

[143] E. Taranko, M. Wiertel, and R. Taranko. Transient electron transport properties of multiple quantum dots systems. *J. App. Phys.*, 111(2):023711, 2012.

[144] Antti-Pekka Jauho, Ned S. Wingreen, and Yigal Meir. Time-dependent transport in interacting and noninteracting resonant-tunneling systems. *Phys. Rev. B*, 50:5528–5544, Aug 1994.

[145] T. Kwapiński, R. Taranko, and E. Taranko. Photon-assisted electron transport through a three-terminal quantum dot system with nonresonant tunneling channels. *Phys. Rev. B*, 72:125312, Sep 2005.

[146] Gloria Platero and Ramón Aguado. Photon-assisted transport in semiconductor nanostructures. *Physics Reports*, 395(1):1 – 157, 2004.

[147] O. Peters, N. Bogdanoff, S. Acero Gonzalez, L. Melischek, J.R. Simon, G. Reecht, C.B. Winkelmann, F. von Oppen, and K.J. Franke. Resonant

Andreev reflections probed by photon-assisted tunnelling at the atomic scale. *Nature Physics*, 16(12):1222–1226, Jul 2020.

[148] R. Mélin and B. Douçot. Inversion in a four-terminal superconducting device on the quartet line. ii. quantum dot and Floquet theory. *Phys. Rev. B*, 102:245436, Dec 2020.

[149] A. L. Samuel. Some studies in machine learning using the game of checkers. *IBM Journal of Research and Development*, 3(3):210–229, 1959.

[150] Tom M Mitchell. *Machine Learning.* New York : McGraw-Hill, 1997.

[151] Martín Abadi, Paul Barham, Jianmin Chen, Zhifeng Chen, Andy Davis, Jeffrey Dean, Matthieu Devin, Sanjay Ghemawat, Geoffrey Irving, Michael Isard, Manjunath Kudlur, Josh Levenberg, Rajat Monga, Sherry Moore, Derek G. Murray, Benoit Steiner, Paul Tucker, Vijay Vasudevan, Pete Warden, Martin Wicke, Yuan Yu, and Xiaoqiang Zheng. Tensorflow: A system for large-scale machine learning, 2016.

[152] Maciej M. Maśka, Anna Gorczyca-Goraj, Jakub Tworzydło, and Tadeusz Domański. Majorana quasiparticles of an inhomogeneous Rashba chain. *Phys. Rev. B*, 95:045429, Jan 2017.

[153] J. Barański, M. Barańska, T. Zienkiewicz, R. Taranko, and T. Domański. Dynamical leakage of majorana mode into side-attached quantum dot. *Phys. Rev. B*, 103:235416, Jun 2021.

[154] L. V. Keldysh. Diagram technique for nonequilibrium processes. *Jetp, 20(5):1080*, 1964.

[155] AP Jauho. Introduction to the Keldysh nonequilibrium green function technique. *Lecture notes, (5):17, 2006*, 2006.

[156] A. Kamenev. Introduction to the Keldysh formalism. *Capri's school lecture notes*, 2009.

[157] A. A. Abrikosov, L. P. Gorkov, I. E. Dzyaloshinski, Richard A. Silverman, and George H. Weiss. Methods of quantum field theory in statistical physics. *Physics Today*, 17(4):78–80, 1964.

[158] Julian Schwinger. Brownian motion of a quantum oscillator. *Journal of Mathematical Physics*, 2(3):407–432, 1961.

[159] Gianluca Stefanucci and Robert van Leeuwen. *Nonequilibrium Many-Body Theory of Quantum Systems: A Modern Introduction.* Cambridge University Press, 2013.

[160] Alec F. White and Garnet Kin-Lic Chan. Time-dependent coupled cluster theory on the Keldysh contour for nonequilibrium systems. *Journal of Chemical Theory and Computation*, 15(11):6137–6153, 2019. PMID: 31600075.

[161] B. Verdonk H. Waadeland A. Cuyt, V. Petersen and W. Jones. *Handbook of Continued Fractions for Special Functions.* Springer, 2008.